



저작자표시-비영리-변경금지 2.0 대한민국

이용자는 아래의 조건을 따르는 경우에 한하여 자유롭게

- 이 저작물을 복제, 배포, 전송, 전시, 공연 및 방송할 수 있습니다.

다음과 같은 조건을 따라야 합니다:



저작자표시. 귀하는 원저작자를 표시하여야 합니다.



비영리. 귀하는 이 저작물을 영리 목적으로 이용할 수 없습니다.



변경금지. 귀하는 이 저작물을 개작, 변형 또는 가공할 수 없습니다.

- 귀하는, 이 저작물의 재이용이나 배포의 경우, 이 저작물에 적용된 이용허락조건을 명확하게 나타내어야 합니다.
- 저작권자로부터 별도의 허가를 받으면 이러한 조건들은 적용되지 않습니다.

저작권법에 따른 이용자의 권리는 위의 내용에 의하여 영향을 받지 않습니다.

이것은 [이용허락규약\(Legal Code\)](#)을 이해하기 쉽게 요약한 것입니다.

[Disclaimer](#)

공학박사학위논문

**A Study on the Microstructure Resetting
Method based on the Electroplasticity
for Metallic Materials**

금속 소재의 통전 소성 거동 이해 기반

미세조직 리셋팅 방법 연구

2020년 2월

서울대학교 대학원

재료공학부

정혜진

**A Study on the Microstructure Resetting
Method based on the Electroplasticity
for Metallic Materials**

금속 소재의 통전 소성 거동 이해 기반
미세조직 리셋팅 방법 연구

지도교수 한 흥 남

이 논문을 공학박사학위논문으로 제출함
2020년 1월

서울대학교 대학원
재료공학부
정 혜 진

정혜진의 박사학위논문을 인준함
2020년 1월

위	원	장	<u>박 은 수</u>	(인)
부	위	원	<u>한 흥 남</u>	(인)
위		원	<u>최 인 석</u>	(인)
위		원	<u>홍 성 태</u>	(인)
위		원	<u>김 문 조</u>	(인)

ABSTRACT

When a high-density electric current is applied to metallic materials, reduced flow stress and increased ductility are generally observed, which is called the electroplasticity. To date, research regarding the effect of electric current (electroplasticity) has been received remarkable attention in both academia and manufacturing. In the initial stage, electroplasticity was observed for various metallic materials, with intensive studies by Troistkii, Conrad, Ross, Roth, and Cao. Subsequently, many researchers have tried to identify the mechanism of electroplasticity and various hypotheses including electron wind force, magnetic, and local Joule heating effects have been proposed. However, the exact mechanism remains unidentified. Previous studies have shown in common that electric current can accelerate microstructural changes such as annealing, aging, dissolution, and recrystallization due to the athermal effect which is distinct from the thermal effect. Recently, based on the beneficial effects of electroplasticity, various efforts for real applications have been actively underway.

The objective of this study is two-fold and is based on electroplasticity. First, the effects of electric current on AZ91 magnesium alloy and transformation-induced plasticity (TRIP)-aided steel were investigated with microstructural observation in Chapters 2 and 3, respectively. Second, based on a clear understanding of the electroplasticity (electric current-induced phenomenon), the microstructure resetting

method using sub-second electric pulsing to reset damaged microstructure for infinite reuse of metallic materials is proposed in Chapter 4.

First, the effect of the electric current on the dissolution of the $Mg_{17}Al_{12}$ phase in as-extruded AZ91 magnesium alloy was investigated by uniaxial tensile testing and microstructural analysis. When a periodic electric pulsing was applied to the specimen during plastic deformation, the flow stress substantially decreased and elongation at fracture increased 3.7 times compared to the non-pulsed tensile test at room temperature (RT, 25 °C). To distinguish between the athermal and thermal effects of electric current, induction heat treatment (IHT) was performed as it follows the temperature history measured during the pulsed tensile test using a dilatometer.

The electron backscatter diffraction (EBSD) and energy dispersive spectrometry (EDS) analyses showed that the $Mg_{17}Al_{12}$ phase significantly dissolved during the pulsed tensile test. In addition, the athermal effect of the electric current on the dissolution of the $Mg_{17}Al_{12}$ phase was examined by comparing the $Mg_{17}Al_{12}$ phase fractions after electropulsing treatment (EPT) and conventional heat treatment (CHT) under the same temperature conditions. Thus, it was demonstrated that electric current can accelerate the dissolution of the $Mg_{17}Al_{12}$ phase during deformation, significantly improving ductility.

Second, the effect of electric current on the mechanically induced martensitic transformation (MIMT) of TRIP-aided steel was investigated based on microstructural analysis and MIMT kinetic calculations. When a periodic electric pulsing was applied to the specimen during deformation (multi-pulsed tension), the

elongation at fracture decreased compared to the non-pulsed tension at RT, although the flow stress significantly reduced. From the X-ray diffraction (XRD) analysis and MIMT calculations, it was identified that the MIMT effect was negligible during the multi-pulsed tension because the stability of the retained austenite phase increased due to a temperature rise.

Thus, a pulsing pattern of the electric current was newly designed to improve the formability of TRIP-aided steel. A total of 3 electric pulsings were applied in the early stage of deformation before phase transformation of the retained austenite phase occurred. As a result, a significant increase in elongation was observed compared to the non-pulsed tension at RT. The increased elongation in the 3-pulsed tension can be explained by two main effects: the delay effect of the phase transformation due to the increased stability of the retained austenite phase during electric current application; and an annealing effect during electric current application, which was identified by comparing the full width at half maximum (FWHM) values obtained from the XRD measurements. Thus, it was confirmed that dislocation annihilation was accelerated by applying electric current.

Lastly, a microstructure resetting method is proposed based on electroplasticity. Generally, microscale defects in metallic materials damage the original microstructure during use, degrading the mechanical properties/life expectancy. Therefore, various methods for healing or repairing damage in these materials have been proposed based on the concept of self-healing. Among them, sub-second electric pulsing was used to reset the damaged microstructure of metallic materials

as a non-autonomous self-healing method.

A key point in the microstructure resetting method is the determination of the critical point where the electric pulsing should be applied to the specimen. Another key point is choosing suitable materials for the resetting core which is proposed herein. The resetting core is defined based on a reversible damage characteristic and classified into three categories: phase transformation, dislocation recovery, and recrystallization. Thus, microstructure resetting-assisted infinite reuse was successfully realized using 301L stainless steel (SUS301L, resulting from martensitic reverse transformation and recrystallization), 316L stainless steel (SUS316L, resulting from recrystallization), and super-elastic NiTi alloy (resulting from martensitic reverse transformation and dislocation recovery).

Finally, electric current-induced dissolution, delay of martensitic transformation, and annealing were thoroughly investigated. The optimal conditions for maximal deformation capacity and efficiency were determined while considering the microstructural features of each material. Furthermore, based on a clear understanding of electric current-induced phenomena, a novel microstructure reset-based self-healing method was proposed. The infinite reuse of metallic materials could be enabled by applying sub-second electric pulsing. This novel method is combined with extreme simplicity, rapidness, and infinite repetition, which cannot be achieved by conventional methods such as heat treatment.

Keywords: Metallic materials, Magnesium alloy, Transformation-induced plasticity (TRIP)-aided steel, Super-elastic NiTi alloy, Electroplasticity, Electrically assisted manufacturing (EAM), SEM, EBSD, XRD, Dissolution, Mechanically induced martensitic transformation (MIMT), Dislocation recovery, Recrystallization, Formability, Damage, Microstructure resetting, Non-autonomous self-healing.

Student number: 2014-22532

Contents

Abstract	I
Table of Contents	VII
List of Tables	XII
List of Figures	XIII

Chapter 1

Introduction

1.1 Electroplasticity	1
1.2 Electrically assisted manufacturing (EAM).....	5
1.3 Thesis motivation	7
1.4 References	10

Chapter 2

Electric current-induced phenomena in AZ91 magnesium alloy

2.1 Introduction.....	12
2.2 Experimental procedure.....	15
2.2.1 Specimen preparation	15
2.2.2 Experimental set-up.....	17
2.2.3 Microstructure observation	21
2.3 Effect of electric current on the mechanical behavior and microstructure.....	22
2.3.1 Mechanical behavior.....	22
2.3.2 Microstructure analysis.....	27
2.4 Electric current-induced dissolution	34
2.5 Electropulsing treatment (EPT) vs conventional heat treatment (CHT)	39

2.6 Conclusion	42
2.7 References	43

Chapter 3

Electric current-induced phenomena in TRIP-aided steel

3.1 Introduction	45
3.2 Experimental procedure	48
3.2.1 Specimen preparation	48
3.2.2 Experimental set-up.....	49
3.2.3 Microstructure observation	52
3.2.4 Model for mechanically induced martensitic transformation (MIMT) kinetics	53
3.3 Effect of electric current on the mechanical behavior and microstructure	58

3.3.1 Initial properties.....	58
3.3.2 Mechanical behavior.....	62
3.3.3 Mechanically induced martensitic transformation (MIMT) kinetics	65
3.4 New pulsing pattern: 3 pulsings in the early stage of deformation	69
3.4.1 Electric current-induced delay of MIMT.....	70
3.4.2 Electric current-induced annealing.....	75
3.5 Conclusion	80
3.6 References	81

Chapter 4

Microstructure resetting method using sub-second electric pulsing

4.1 Introduction	84
4.2 Experimental procedure	88
4.2.1 Specimen preparation and experimental set-up.....	88
4.2.2 Strategy of microstructure resetting method.....	91
4.2.3 Microstructure observation	95
4.3 Case 1: 301L Stainless steel (SUS301L)	97
4.4 Case 2: 316L Stainless steel (SUS316L)	107
4.5 Case 3: super-elastic NiTi alloy	116
4.6 Conclusion	126
4.7 References	129

Chapter 5

Total conclusion	132
-------------------------------	-----

LIST OF TABLES

Table 3.1 Material's parameters in Eq. (3.5) for the investigated TRIP-aided steel.

Table 4.1 Parameters of electric pulsing condition for the (a) SUS301L, (b) SUS316L, and (c) super-elastic NiTi alloy.

LIST OF FIGURES

Figure 1.1 Number of published articles which include keywords such as “electroplasticity”, “electropulsing”, and “electrically assisted” over time.

Figure 1.2 Number of published articles which include keywords such as “self-healing” and “metal” over time.

Figure 2.1 Optical micrograph of as-extruded AZ91 magnesium alloy.

Figure 2.2 (a) Instrumental set-up for non-pulsed/pulsed tensile test (Uniaxial tensile machine is modified to insulate from applied electric current), (b) Pulsing condition ($\rho_0=80 \text{ A/mm}^2$, $t_d=0.5 \text{ s}$, $t_p=20 \text{ s}$) applied to the specimen during uniaxial tensile test.

To maintain constant electric current density, the different value of electric current was applied to the specimen considering the decrease of cross sectional area during deformation.

Figure 2.3 Schematic diagram of the electropulsing treatment (EPT) equipment.

Figure 2.4 (a) Engineering stress-strain curves of non-pulsed tensile test at room temperature (RT, black line), non-pulsed tensile test at 70 °C (green line), and pulsed tensile test (red line) at the cross head speed of 1 mm/min. (b) The temperature of specimen measured during pulsed tensile test.

Figure 2.5 The temperature of specimen measured during pulsed tensile test until the engineering strain of 13% (red line) and induction heat treatment (IHT) using induction heater in a vacuum (blue line).

Figure 2.6 EBSD orientation maps and inverse pole figures for extrusion direction (ED, loading direction) obtained from (a) as-extruded, (b) induction heat treatment (IHT) after the non-pulsed tension at 70 °C and (c) pulsed tension, at the engineering strain of 13%. (misorientation angle: 10°).

Figure 2.7 EBSD grain orientation spread (GOS) maps and inverse pole figures for recrystallized grains obtained from (a) as-extruded, (b) induction heat treatment (IHT) after the non-pulsed tension at 70 °C, and (c) pulsed tension, at the engineering strain

of 13%. (misorientation angle: 10°).

Figure 2.8 Recrystallized area fraction (in red circle, left axis) and grain size (in blue square, right axis) for each three specimens measured from GOS maps. (misorientation angle: 10°).

Figure 2.9 SEM micrographs after fracture for the (a) non-pulsed tension at 70 °C and (b) pulsed tension.

Figure 2.10 EDS phase maps of specimens obtained from (a) as-extruded, (b) non-pulsed tension at 70 °C, (c) induction heat treatment (IHT) after the non-pulsed tension at 70 °C, and (d) pulsed tension, at the engineering strain of 13% (yellow area: Mg₁₇Al₁₂, green area: Matrix). The arrows indicate crack within Mg₁₇Al₁₂ phase. (e) The average fraction of Mg₁₇Al₁₂ phase for the specimens at engineering strain of 0%, 5%, and 13% obtained from non-pulsed tension at RT (rectangle symbols), non-pulsed tension at 70 °C (triangle symbols), and pulsed tension (circle symbols).

Figure 2.11 Vickers Hardness (HV) measurement of specimen obtained from the

non-pulsed tension at 70 °C (triangle symbol), IHT after the non-pulsed tension at 70 °C (inverted triangle symbol), and pulsed tension (circle symbol) at the engineering strain of 13% compared to the as-extruded specimen (rectangle symbol).

Figure 3.1 Schematics of (a) experimental set-up for non-pulsed/pulsed tensile tests and (b) two types pulsing conditions applied to the specimen during uniaxial tensile test.

Figure 3.2 (a) EBSD inverse pole figure map for normal direction (ND), (b) EBSD phase map (red area: retained austenite phase, green area: ferrite matrix), and (c) X-ray diffraction pattern in the range of 18-36° for the investigated TRIP-aided steel.

Figure 3.3 Elements distribution in the initial specimen: (a) backscattered electron image, (b) C distribution, (c) Al distribution, (d) Si distribution, and (e) Mn distribution.

Figure 3.4 (a) True stress-strain curves of non-pulsed tension at RT (in black), non-pulsed tension at 100 °C (in green), and multi-pulsed tension (in blue) under the cross

head speed of 1.5 mm/min. (b) The temperature of specimen measured during multi-pulsed tension.

Figure 3.5 (a) The calculated strain hardening exponent and (b) the fraction of retained austenite phase as a function of true strain for non-pulsed tension at RT (in black), non-pulsed tension at 100 °C (in green), and multi-pulsed tension (in blue). The experimental data (symbols) and calculated data (lines) were based on the XRD measurement and MIMT kinetics model, respectively.

Figure 3.6 (a) True stress-strain curves of non-pulsed tension at RT (in black) and 3-pulsed tension (in red) under the cross head speed of 1.5 mm/min. (b) The temperature of specimen measured during 3-pulsed tensile test.

Figure 3.7 (a) The calculated strain hardening exponent and (b) the fraction of retained austenite phase as a function of true strain for the non-pulsed tension at RT (in black) and 3-pulsed tension (in red). The experimental data (symbols) and calculated data (lines) was based on the XRD measurement and MIMT kinetics

model, respectively.

Figure 3.8 (a) Temperature histories during 3-pulsed tension (in red), non-pulsed tension at RT (in black), 100 °C (in green) and 200 °C (in purple) until the true strain of 0.076. EBSD phase maps (red area: retained austenite phase, green area: ferrite matrix) for the four specimens obtained from: (b) the non-pulsed tension at RT, (c) the non-pulsed tension at 100 °C, (d) the non-pulsed tension at 200 °C, and (e) the 3-pulsed tension.

Figure 3.9 FWHM profiles (symbols, left axis) of ferrite phase peaks and X-ray diffraction patterns (lines, right axis) in the range of 18-36° for the four specimens strained to the true strain of 0.076 in the 3-pulsed tension (in red), non-pulsed tension at RT (in black), 100 °C (in green) and 200 °C (in purple).

Figure 4.1 (a) Scheme for the process design showing the mechanical behavior of tensile deformation after each pulsing treatment and change in damage for the specimen and (b) Resetting cores (phase transformation, dislocation recovery, and

recrystallization) reflecting reversible damage characteristics at microscale.

Figure 4.2 (a) Geometry of tensile specimen for the SUS301L and SUS316L. The gage length is 12 mm. For the super-elastic NiTi alloy, the tensile specimen was fabricated by halving the SUS301L/SUS316L specimen size. (b) Actual image of custom-made fixture for stress relief.

Figure 4.3 Schematics of experimental procedure of pulsing treatment and loading/unloading in the microstructure resetting method for (a) SUS301L/SUS316L and (b) super-elastic NiTi alloy.

Figure 4.4 (a) Tensile curve (line) and work-hardening rate (symbol). The work hardening rate of SUS301L is obtained from the slope of the true stress–strain curve, which is related to the volume fraction of the mechanically induced martensite phase. (b) EBSD phase maps showing the MIMT as the plastic deformation increases.

Figure 4.5 (a) Tensile curve data during reloading after single pulsing treatment at the pre-strain of 27%, 52%, and 72%. (b) Recrystallization fraction (left axis) and

average grain size (right axis) after each pulsing. (c), (d), and (e) EBSD inverse pole figure (IPF), phase, and grain orientation spread (GOS) maps for specimen after single pulsing treatment at the pre-strain of 27%, 52%, and 72% with initial specimen. The orange and dark green areas in the GOS map indicate the recrystallized and unrecrystallized grain, respectively.

Figure 4.6 Maximum temperatures of specimen measured during pulsing treatment for SUS301L. The time between the previous pulsing and the next pulsing is independent of the actual time of the experiment. To aid in understanding, the temperature histories of each pulsing are arranged in order at a certain interval.

Figure 4.7 (a) Tensile behavior after each pulsing treatment based on the critical point (engineering strain of 52%) is described in red line. The order of pulsing is indicated with arrows. (b) Photograph of specimen after fracture through the microstructure resetting process. To compare the ductility, photograph of initial specimen is also shown.

Figure 4.8 (a) Engineering yield strength and average grain size after each pulsing treatment. Error bars represent standard deviation from the average value. (b) EBSD inverse pole figure (IPF) maps for normal direction (ND) before and after 2nd, 5th, 8th, and 10th pulsing compared to the initial specimen. The different colors in the IPF map indicate the orientation of each grain with respect to ND.

Figure 4.9 (a) X-ray diffraction (XRD) patterns before and after 2nd and 8th pulsing. For the comparison, the XRD pattern for the initial specimen is shown. Theta is the Bragg angle. The symbols of face-centered cubic (f.c.c.) and body-centered cubic (b.c.c.) are presented as star and circle, respectively. (b) EBSD phase maps before and after 2nd, 5th, 8th, and 10th pulsing compared to the initial specimen. The blue and red area in phase map indicate the f.c.c. and b.c.c. phase, respectively. The fraction of f.c.c. and b.c.c. phase is shown within the phase map.

Figure 4.10 (a) Tensile curve (line) and work-hardening rate (symbol). The work hardening rate of SUS316L decreases continuously as the true strain increases. (b) EBSD phase maps showing no change in the phase fraction as the plastic

deformation increases.

Figure 4.11 Maximum temperatures of specimen measured during pulsing treatment for SUS316L. The time between the previous pulsing and the next pulsing is independent of the actual time of the experiment. To aid in understanding, the temperature histories of each pulsing are arranged in order at a certain interval.

Figure 4.12 (a) Tensile behavior after each pulsing treatment based on the critical point (engineering strain of 40%). The order of pulsing is indicated with arrows. (b)

Photograph of specimen after fracture compared to the initial specimen.

Figure 4.13 (a) Engineering yield strength and average grain size after each pulsing treatment. Error bars represent standard deviation from the average value (b) EBSD grain orientation spread (GOS) maps after 1st, 2nd, and 3rd pulsing with initial specimen. The orange and dark green area in the GOS map indicate the recrystallized and unrecrystallized grain, respectively.

Figure 4.14 EBSD IPF maps for ND, RD, and TD after 1st, 2nd, and 3rd pulsing with

initial specimen for the SUS316L. The different colors in the IPF ND, RD, and TD maps indicate the orientation of each grain with respect to ND, RD, and TD, respectively.

Figure 4.15 (a) X-ray diffraction (XRD) patterns before and after 1st and 3rd pulsing. For the comparison, the XRD pattern for the initial specimen is shown. (b) Full width at half maximum (FWHM) profiles of austenite phase peaks before and after each pulsing in addition to the initial specimen. The (111), (200), (220), and (311) peaks of austenite phase are used to obtain the FWHM values based on the XRD pattern.

Figure 4.16 (a) The average kernel average misorientation (KAM) values before (unfilled symbol) and after (filled symbol) each pulsing in addition to the initial specimen (black filled symbol). (b) EBSD KAM maps at each condition. The range of degree of misorientation is 0 to 5, and is indicated in red to blue. Note that the brighter the colored areas, the more deformed the part with a higher dislocation density.

Figure 4.17 (a) Schematic stress-strain curves representing the super-elasticity (SE) characteristics for 1st and Nth cycles during the mechanical training. (b) Maximum temperatures of specimen measured during pulsing treatment for the super-elastic NiTi alloy. The time between the previous pulsing and the next pulsing is independent of the actual time of the experiment. To aid in understanding, the temperature histories of each pulsing are arranged in order at a certain interval.

Figure 4.18 Stress-strain curves for 1st, 2nd, 3rd, 5th, 10th, 50th, and 100th cycle during the mechanical training of 100 cycles at RT for the (a) initial specimen, (b) specimen after 1st pulsing treatment, and (c) specimen after 2nd pulsing treatment, respectively. The stress-strain curve of first and final cycle is represented in colored solid line.

Figure 4.19 Effect of the mechanical training of 100 cycles on (a) residual strain and (b) recovered strain after each pulsing treatment. These data were obtained from the Fig. 4.18.

Figure 4.20 (a) XRD patterns for the specimens before and after 1st pulsing. For the

comparison, the XRD pattern for the initial specimen is also shown. To clearly show the formation of stabilized martensite phase (B19'), the part where the peaks of the martensite phase appears is enlarged. (b) EBSD image quality (IQ) maps for the specimens before and after 1st pulsing. The stabilized martensite phase is marked by red arrows.

Figure 4.21 (a) FWHM profiles of B2 austenite phase peaks before and after each pulsing in addition to the initial specimen. The (110), (111), (211), and (220) peaks of B2 austenite phase are used to obtain the FWHM values based on the XRD pattern. (b) The KAM values before (unfilled symbol) and after (filled symbol) each pulsing. (c) EBSD KAM maps at each condition.

Figure 4.22 EBSD inverse pole figure (IPF) maps for normal direction (ND) before and after 1st, 2nd, and 3rd pulsing treatment with initial specimen. The different colors in the IPF map indicate the orientation of each grain with respect to ND.

Figure 4.23 Summary for the principle of microstructure resetting in the selected

three materials based on the resetting core classified into three categories (phase transformation, dislocation recovery, and recrystallization) for the (a) SUS301L, (b) SUS316L, and (c) super-elastic NiTi alloy.

Chapter 1

Introduction

1.1 Electroplasticity

When an electric current is applied to metals during deformation, flow stress decreases and ductility significantly increases. This phenomenon often referred to electroplasticity. The electroplasticity was first reported by Troistkii in 1969 [1]. A series of extensive studies regarding the electroplasticity of various metals were conducted by Conrad, indicating that high electric current can clearly enhance ductility of metals in addition to the side effect of Joule heating [2, 3]. The number of research articles on the effect of electric current (electroplasticity) are drastically increasing in both academia and industry, as shown in Fig. 1.1.

Entering the 2000s, observations of the electroplasticity were intensively reported for various metallic materials, including aluminum, copper, and brass alloys [4–9]. When a pulsed electric current was applied to 5754 aluminum alloy during tensile test, the elongation increased up to 400% of the gauge length [6]. In addition, the effects of pulse duration and current density were examined to obtain optimal specimen elongation [7]. Previous study has also indicated that the elongation can be approximately doubled and the flow stress decreased by applying pulsed electric current during tensile test for the AZ31B-O magnesium alloy [8].

The effects of electric current on mechanical behavior have also been examined based on microstructural observations. For example, the relationships between grain size and flow stress reduction under an electric current have been reported [10, 11]. Recently, the annihilation of dislocation was shown to be accelerated by applying pulsed electric current during tensile test of the 5052 aluminum alloy [12]. The authors observed that early stage of precipitation or atomic clustering from a supersaturated state, i.e. aging process, can be enhanced by applying electric current [13]. In addition, it was reported that recrystallization kinetics are accelerated by electropulsing treatment compared to furnace heat treatments for interstitial free (IF) steel and AZ31 magnesium alloy [14]. They showed in common an obvious athermal effect caused by electric current, which is distinct from thermal effect due to Joule heating.

Although some researchers tried to identify the fundamental mechanism of electroplasticity, the exact mechanism has not been yet elucidated. One of the various hypotheses which have been proposed is that the mechanical behavior of metals under an electric current is not properly described in terms of thermal effects due to Joule heating. For example, it was suggested that the thermal effect may play a significant role in electroplasticity by introducing a new material parameter such as current density sensitivity to thermal mechanical constitutive models [15]. In contrast, it has been also reported that electroplasticity cannot be clearly understood without consideration of athermal effects, including electric current-induced annealing [12], aging [13], and recrystallization [14]. However, the proposals share

a common idea that the electric current can enhance the mobility of metal atoms, resulting in accelerating diffusion kinetics.

Increased research interests in **Electroplasticity** (Keyword: electroplasticity, electropulsing, electrically assisted)

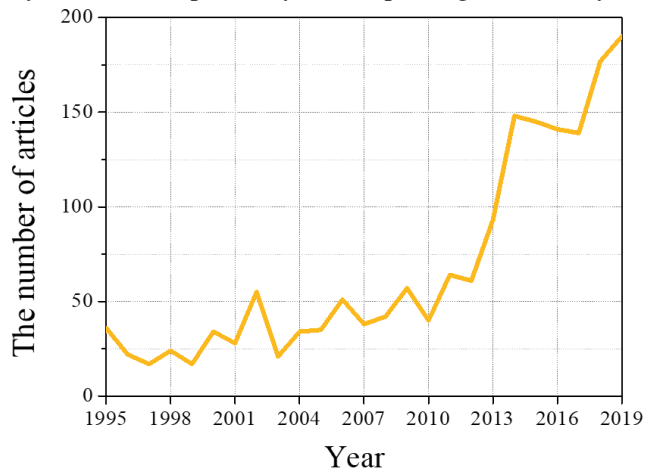


Figure 1.1 Number of published articles which include keywords such as “electroplasticity”, “electropulsing”, and “electrically assisted” over time.

1.2 Electrically assisted manufacturing (EAM)

The properties of metallic materials can be drastically improved by applying an electric current to metals during deformation. As reports regarding electroplasticity have become more abundant, various attempts have recently been made to directly apply it to conventional manufacturing processes. Manufacturing technology utilizing the electroplasticity is called electrically assisted manufacturing (EAM), which is a relatively new hybrid manufacturing technology that can be used to improve productivity, efficiency, and material quality [16, 17].

Conventional processes require large areas for heating furnaces and time to heat up the furnace with excess energy to maintain the furnace and mold temperature. However, EAM requires only a small space for a power supply and can heat materials rapidly. Therefore, it is possible to save space and energy by using EAM compared to conventional processes. Moreover, since EAM is expected to be performed at relatively low temperatures, the common problems of conventional processes such as thermal stress, warping, and low tolerance controllability can be minimized.

Recently, various studies have been conducted for practical processes in industries to harness the beneficial effects of EAM. For example, it has been reported that the energy efficiency and formability for forging can be improved by applying electric current during compression deformation [18]. The efficiency of manufacturing can be enhanced by reducing the forming load and/or increasing formability during bending [19], rolling [20], blanking [21], and drawing [22]. It has also been reported that springback during sheet metal forming can be effectively

reduced by applying electric current during processing [23].

Therefore, the EAM is a cost-effective and energy-saving manufacturing strategy that can enhance product quality. Furthermore, if an electrode can be properly designed for each process, EAM can be applied to various processes with potential applications in the manufacture of numerous products.

1.3 Thesis motivation

The objective of the present study is two-fold. First, electric current-induced phenomena are clearly understood by applying electric current during tensile deformation of AZ91 magnesium alloy and transformation-induced plasticity (TRIP)-aided steel in Chapters 2 and 3, respectively. To improve both mechanical properties of materials and process efficiency, the electric current should be properly applied to suit the microstructural characteristics of the target material. Thus, it is essential to understand the initial material properties, followed by an evaluation of the effect of electric current on the mechanical behavior and microstructural changes. Subsequently, the optimal pulsing condition that enhance both formability of the material and process efficiency will be obtained by careful design of the pulsing pattern.

Second, based on the understood electroplasticity, a microstructure resetting method that can instantly reset a damaged microstructure to its original state using sub-second electric pulsing is proposed in Chapter 4. This novel method, which is based on the concept of non-autonomous self-healing, renders metallic materials infinitely reusable in theory. Moreover, although research regarding self-healing is rapidly increasing in popularity and impact, the application of self-healing in bulk metallic materials is still challenging due to low atomic mobility or diffusivity, high melting points, and difficulty in detecting damage, as shown in Fig. 1.2. Therefore, to overcome these problems, the microstructure reset-based self-healing method is newly proposed as an innovative strategy for the self-healing of metallic materials

in this chapter. Finally, it is expected that this novel method will provide real industrial applications and academic interests regarding the electroplasticity.

Increased research interests in **Self-healing** (Keyword: self-healing, metal)

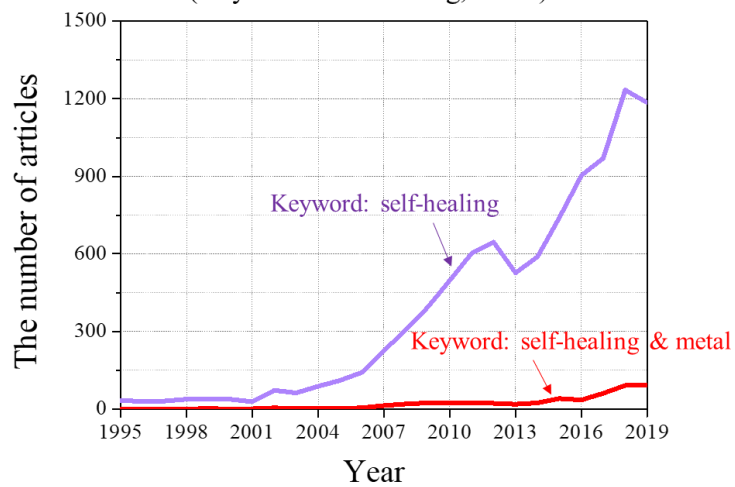


Figure 1.2 Number of published articles which include keywords such as “self-healing” and “metal” over time.

1.4 References

- [1] O. A. Troitskii, *Pis'ma Zhurn. Experm. Teoret. Fiz.*, 10 (1969) 18.
- [2] K. Okazaki, M. Kagawa, H. Conrad, *Scr. Metall.*, 12 (1978) 1063.
- [3] H. Conrad, *Mater. Sci. Eng. A*, 287 (2000) 276.
- [4] C. Ross, J. T. Roth, ASME 2005 International Mechanical Engineering Congress and Exposition, (2005) 363.
- [5] C. D. Ross, D. B. Irvin, J. T. Roth, *J. Eng. Mater. Technol.*, 129 (2007) 342.
- [6] J. T. Roth, I. Loker, D. Mauck, M. Warner, S. F. Golovashchenko, A. Krause, *Trans. NAMRI/SME.*, 36 (2008) 405.
- [7] W. A. Salandro, J. J. Jones, T. A. McNeal, J. T. Roth, S.-T. Hong, M. T. Smith, *J. Manuf. Technol.*, 132 (2010) 051016.
- [8] W. A. Salandro, A. Khalifa, J. T. Roth, *Trans. NAMRI/SME.*, 37 (2009) 387.
- [9] J. Magaree, F. Morestin, J. Cao, *J. Eng. Mater. Technol.* 135 (2013) 041003.
- [10] M. S. Siopis, B. L. Kinesy, *ASME J. Manuf. Sci. Eng.*, 132 (2010) 021004.
- [11] R. Fan, J. Magaree, P. Hu, J. Cao, *Mater. Sci. Eng. A*, 574 (2013) 218.
- [12] M.-J. Kim, K. Lee, K. H. Oh, I. S. Choi, H. H. Yu, S.-T. Hong, H. N. Han, *Scr. Mater.*, 75 (2014) 58.
- [13] M.-J. Kim, M.-G. Lee, K. Hariharan, S.-T. Hong, I.-S. Choi, D. Y. Kim, K. H. Oh, H. N. Han, *Int. J. Plast.*, 94 (2017) 148.
- [14] J.-W. Park, H.-J. Jeong, S.-W. Jin, M.-J. Kim, K. Lee, J. J. Kim, S.-T. Hong, H. N. Han, *Mater. Character.*, 133 (2017) 70.
- [15] J. Magaree, R. Fan, J. Cao, *J. Manuf. Sci. Eng.*, 135 (2013) 061022.

- [16] W.-S. Chu, C.-S. Kim, H.-T. Lee, J.-O. Choi, J.-I. Park, *Int. J. Precis. Eng. Manuf.-Green Tech.*, 1 (2014) 75.
- [17] C. Park, B.-S. Shin, M.-S. Kang, Y.-W. Ma, J.-Y. Oh, *Int. J. Precis. Eng. Manuf.*, 16 (2015) 1385.
- [18] S. T. Hong, Y.-H. Jeong, M. N. Chowdhury, D.-M. Chun, M.-J. Kim, H. N. Han, *CIRP Ann. Manuf. Technol.*, 64 (2015) 277.
- [19] A. J. S. Egea, H. A. G. Rojas, D. J. Clentanob, J. A. T.-Rodríguez, J. L. i Fuentes, *J. Mater. Process. Technol.*, 214 (2014) 2261.
- [20] Z. Xu, G. Tang, S. Tian, F. Ding, H. Tian, *J. Mater. Process. Technol.* 182 (2007) 128.
- [21] W. Kim, K.-H Yeom, N. T. Thien, S.-T. Hong, B.-K. Min, S. I. Oh, M.-J. Kim, H. N. Han, H.-W. Lee, *CIRP Ann. Manuf.*, 63 (2014) 273.
- [22] H. Xie, X. Dong, Z. Ai, Q. Wang, F. Peng, K. Liu, F. Chen, J. Wang, *Int. J. Adv. Manuf. Technol.*, 86 (2016) 1063.
- [23] M. S. Kim, N. T. Vinh, H. -H. Yu, S. -T. Hong, H.-W. Lee, M. -J. Kim, H. N. Han, J. T. Roth, *Int. J. Precis. Eng. Manuf.*, 15 (2014) 1207.

Chapter 2

Electric current-induced phenomena in AZ91 magnesium alloy

2.1 Introduction

Recently, as governments tighten legislative regulations for CO₂ emission, reduction of vehicle weight and improving the fuel efficiency of vehicle are becoming important issues in the automotive industry [1, 2]. Thus, demands for magnesium alloys are globally increasing because of their low density, high specific strength, and extending application such as electronic component and car body [3–5]. Among various magnesium alloys, AZ91 (Mg-9.0Al-1.0Zn in wt.%) is one of the most popular magnesium alloys due to superior corrosion resistance, specific strength, and castability than other magnesium alloys [2, 6, 7]. However, AZ91 alloy usually contains significant amounts of the intermetallic Mg₁₇Al₁₂ phase distributing along the grain boundary [6]. Microcracks easily initiate at the interface between Mg₁₇Al₁₂ phase and magnesium matrix or inside the Mg₁₇Al₁₂ phase, resulting in poor strength and formability [7, 8]. Thus, before forming and deformation, these phases should be artificially dissolved into matrix through an ordinary solution heat treatment (HT). However, it inevitably induces local deformation, grain growth, surface oxidation, and low production efficiency of AZ91 alloys. Therefore, a new

technique in practical process should be developed for improving their low formability without requiring additional process.

Recently, to overcome this problem, electropulsing treatment (EPT), which is an instantaneous high-energy input method and can be applied to controlling the microstructure and property of materials without deformation, has been introduced. Many researchers have studied the effect of EPT on mechanical property [9–11], phase transformation [12–15], recrystallization [16, 17], and aging process [18]. Jiang *et al.* reported that EPT accelerated the dissolution of $Mg_{17}Al_{12}$ phase in aged AZ61 magnesium alloy [12]. It was also reported that EPT accelerated recrystallization in cold-rolled AZ91 magnesium alloy due to the enhancement of nucleation rate and atomic diffusion resulting from the coupling of the thermal and athermal effects [14]. Du *et al.* observed the increased elongation and grain size through EPT for ECAPed AZ31 magnesium alloy due to the enhancement of the recrystallization nucleation rate and the annihilation of the dislocations [17]. Wang *et al.* reported that EPT accelerated the aging process of Cu-Cr-Zr alloy due to the enhancement of diffusion of solute atoms and the mobility of vacancies [18]. These studies about EPT suggested in common that microstructural change through atomic diffusion could be accelerated by applying electric current, resulting in enhancement of materials property.

Based on the effect of EPT, Zhu *et al.* studied the effect of dynamic electropulsing on microstructural evolution and elongation of Zn-Al-Cu alloy during tensile test. The authors reported that under electropulsing, the elongation was

increased by 437% due to acceleration of dislocation movement by electropulsing during tensile test [19]. However, even though a few studies have been reported on effect of EPT or dynamic electropulsing for various alloys, the electroplasticity effect on as-extruded AZ91 alloy has not been investigated until now.

In this chapter, the effect of electric current on dissolution of $Mg_{17}Al_{12}$ phase in as-extruded AZ91 alloy during plastic deformation was investigated. The tensile tests with or without pulsed electric current (hereafter “pulsed tensile test” and “non-pulsed tensile test”, respectively) were carried out. Microstructure change in specimens subjected to non-pulsed and pulsed tensile test was observed using scanning electron microscopy (SEM), energy dispersive x-ray spectroscopy (EDS), and electron backscatter diffraction (EBSD). The mechanical behavior associated with electroplasticity was discussed based on the microstructure analysis.

2.2 Experimental procedure

2.2.1 Specimen preparation

A commercial AZ91 (Mg-9.0Al-1.0Zn in wt.%) magnesium alloy billet was used in this study. It was indirectly extruded at 300 °C, ram speed of 1.0 mm/s, and an extrusion ratio of 25; from initial diameter of 80 mm to final diameter of 16 mm. The die and container were pre-heated to the initial billet temperature of 300 °C to avoid temperature variation in the remaining billet during extrusion. After processing, the extruded billet was cooled in air. Fig. 2.1 shows the optical micrographs of the extruded billet.

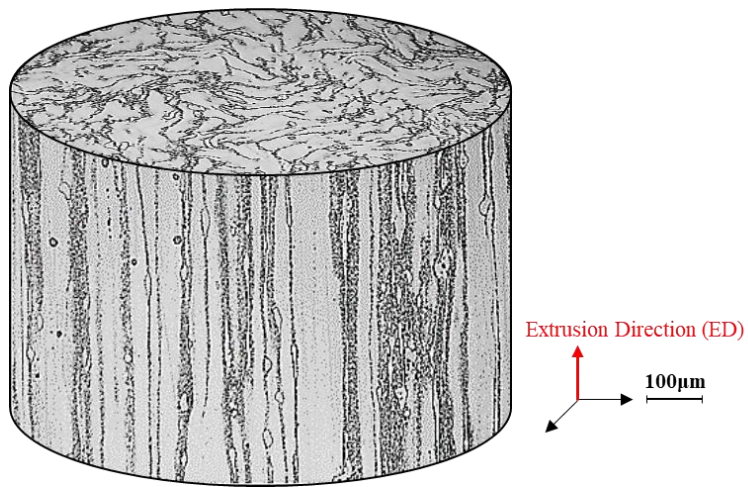


Figure 2.1 Optical micrograph of as-extruded AZ91 magnesium alloy.

2.2.2 Experimental set-up

The uniaxial tensile test was conducted at the constant crosshead speed of 1.0 mm/min (corresponding to the nominal strain rate of 0.00067/s). Fig. 2.2a describes the experimental set-up for non-pulsed/pulsed tensile test. The tensile test machine (INSTRON 5584, USA) was modified to make electric current pass only through the specimen by inserting bakelite between the specimen and each grip, which was described previously by Kim *et al.* [20, 21]. The specimens used for the tensile test were prepared with a gauge width of 6.25 mm and a gauge length of 25 mm along the extrusion direction according to the ASTM E8 subsize. The displacement of the specimen was measured by ARAMIS Digital Image Correlation (DIC) system (GOM, Germany), which can measure relative displacements of characteristic points on the digital images. For preparing of the tensile specimen used for DIC system, a black speckle pattern was formed using spray paint to create a high contrast with the white surface coating and displacement measurement was taken from this surface pattern.

For the uniaxial tensile test with a pulsed electric current, the electric current was generated by a Vadal SP-1000U DC power supply (Hyosung, South Korea) and periodically applied to the specimen with a duration (t_d) of 0.5 s and a period (t_p) of 20 s during deformation, as schematically shown in Fig. 2.2b. The first pulse of electric current was applied right before yielding. In order to maintain constant electric current density (ρ) of 80 A/mm² based on the initial cross-sectional area of the specimen, a different amplitude of electric current every pulse was applied to the

specimen considering the decrease of cross-sectional area of the specimen during deformation. Specimen temperature during pulsed tensile test was measured by a FLIR-E40 infra-red (IR) thermal imaging camera (FLIR, Sweden). For this measurement, high temperature black paint was sprayed to the other side of the tensile specimen facing the FLIR camera to stabilize the emissivity of the specimen. Note that the temperature measured by using FLIR camera system was calibrated comparing with that by using a K-type thermocouple.

EPT was conducted to identify acceleration of dissolution of $Mg_{17}Al_{12}$ phase by electric current. Fig. 2.3 shows a schematic diagram of the treatment machine used for EPT, which was used previously by Lee *et al.* [22]. The specimen was prepared with the diameter of 20 mm and thickness of 2 mm, which was positioned between two graphite electrodes to apply pressure and make electric current pass through the specimen. The target temperatures were set to 350 and 400 °C which are below dissolution temperature of $Mg_{17}Al_{12}$ phase. Note that nominal dissolution treatment for AZ91 alloy has been specified to be at temperature ranging from 400 to 420 °C [23]. The specimen was heated at rate of 100 °C/min and maintained at the setting temperature during 10 min. After EPT, the specimen was taken out of the vacuum chamber, and then it was water quenched. To investigate the athermal effect of electric current, the conventional heat treatment (CHT) using a furnace (Lindberg, Thermo Electron Corporation, USA) was conducted at the identical temperature history with EPT. Note that a K-type thermocouple was attached to the center position of specimen and the temperature of specimen was monitored in real time.

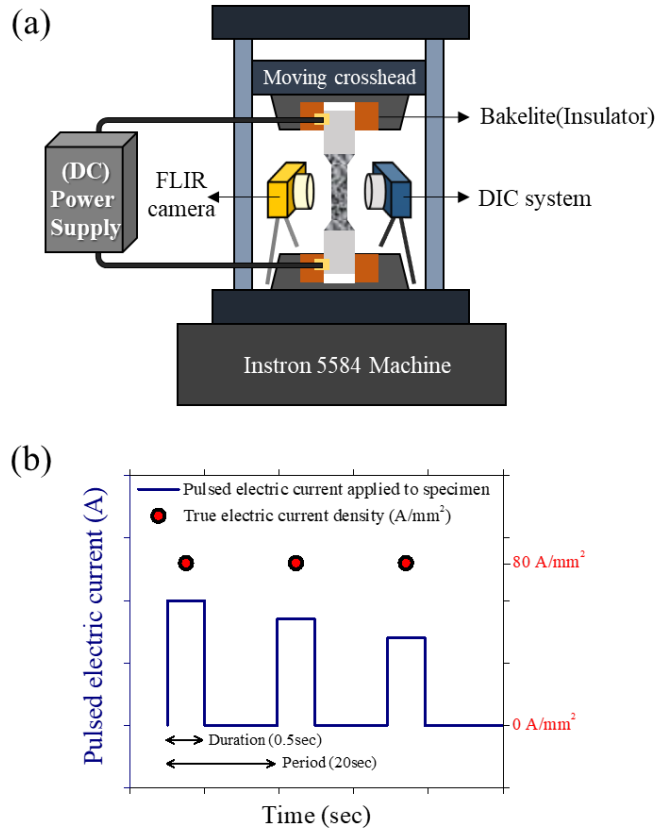


Figure 2.2 (a) Instrumental set-up for non-pulsed/pulsed tensile test (Uniaxial tensile machine is modified to insulate from applied electric current), (b) Pulsing condition ($\rho_o=80 \text{ A/mm}^2$, $t_d=0.5 \text{ s}$, $t_p=20 \text{ s}$) applied to the specimen during uniaxial tensile test. To maintain constant electric current density, the different value of electric current was applied to the specimen considering the decrease of cross sectional area during deformation.

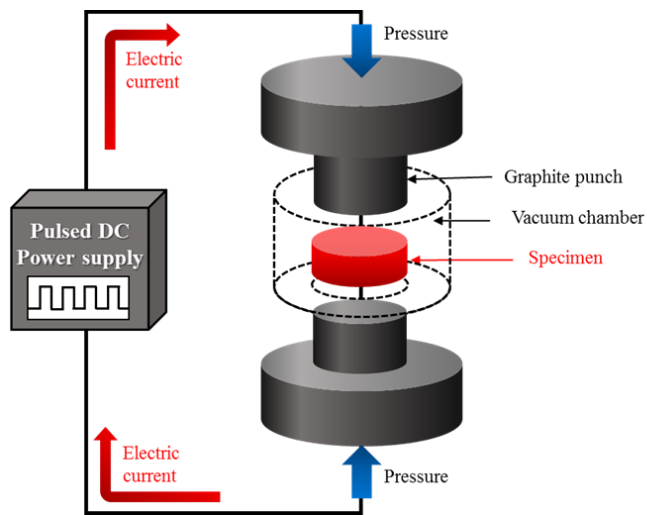


Figure 2.3 Schematic diagram of the electropulsing treatment (EPT) equipment.

2.2.3 Microstructure observation

The macrostructure of the as-extruded billet was observed using optical microscopy (OM) and the microstructures were characterized by using a field emission gun scanning electron microscope (FE-SEM, MERLIN COMPACT, Carl Zeiss, Germany) equipped with energy dispersive x-ray spectroscopy (EDS). The fraction of $Mg_{17}Al_{12}$ phase was determined using phase mapping analysis in the EDS software. The AutoPhaseMap module in the EDS software automatically finds areas of different characteristic composition and determines the area fraction of these phases. For EDS phase mapping analysis, the specimens were prepared by mechanical grinding followed by etching with a 5 ml nitric acid and 95 ml methanol solution. More than 10 images of each specimen were observed for the validity on the average fraction of $Mg_{17}Al_{12}$ phase. Vickers hardness measurement was conducted with a 0.03 kg load and the hardness was measured at least 10 times for each specimen. The crystallographic orientation maps were obtained by FE-SEM (SU70, Hitachi, Japan) equipped with EBSD system (EDAX/TSL, Hikari, USA). The specimen preparation included conventional mechanical grinding, grinding using colloidal silica suspension (0.1 μm) and ion milling. Ion milling (IM4000, Hitachi, Japan) was carried out for 40 min at 6 kV and 420 μA . For EBSD analysis, the accelerating voltage and scan step size were 15 kV and 0.8 μm , respectively. The critical misorientation angle was set to 10° for grain identification.

2.3 Effect of electric current on the mechanical behavior and microstructure

2.3.1 Mechanical behavior

Figure 2.4a shows engineering stress-strain curves of non-pulsed and pulsed tensile test at room temperature (RT, 25 °C). In the non-pulsed tensile test, the specimen yields at ~300 MPa undergoes strain hardening and fails after 7.7% elongation. In the pulsed tensile test, after each pulse the flow stress decreased rapidly and then increased due to strain hardening until the next pulse. The decrease in flow stress on application of electric current is known to be caused by the combined effect of three phenomena. The phenomena are: 1. Electric current induced annealing; 2. Softening by temperature rise due to Joule heating; and 3. Thermal expansion due to Joule heating. When compared to the non-pulsed specimen, the pulsed specimen showed remarkable ductility. The elongation increased ~3.7 time viz. from 7.7% to 28.8%.

Figure 2.4b shows the measured specimen temperature during the pulsed tensile test. In each electric pulse, the specimen temperature increased instantly because of Joule heating. After applying the electric pulse, the specimen temperature decreased because of air cooling until the next pulse. The peak value of measured temperature was almost same as about 300 °C. This was because the amplitude of electric current was varied, according to the decrease in cross sectional area of the specimen during deformation, to keep the electric current density constant.

To evaluate the effect of temperature due to Joule heating on mechanical behavior, the non-pulsed tensile test at 70 °C, which is the lowest value of the measured temperature in Fig. 2.4b, was carried out as shown in Fig. 2.4a. In the non-pulsed tensile test at 70 °C, the flow stress decreased and the elongation increased from 7.7% to 13.8% when compared with the non-pulsed tensile test at RT. However, the elongation of the pulsed tensile test was 2 times higher than that of the non-pulsed tensile test at 70 °C. Also, the flow stress of the pulsed tensile test was clearly lower than that of the non-pulsed tensile test at 70 °C.

The increase in elongation in pulsed tensile test was attributed to various effects. Among them, the most dominant effect is a dissolution effect of $Mg_{17}Al_{12}$ phase in extruded AZ91 alloy. As noted earlier, the dissolution effect acts as important role to improving ductility of AZ91 alloy. As shown in Figs. 2.4a and b, even though the peak value of specimen temperature (~300 °C) is quite below the nominal dissolution treatment temperature (~420 °C), the noticeably improved ductility was obtained in pulsed tensile test. From this fact, it may seem that there is athermal effect of electric current on dissolution of $Mg_{17}Al_{12}$ phase during plastic deformation. However, it should be noted that both thermal effect due to Joule heating and athermal effect of electric current work at the same time during pulsed tensile test.

In order to distinguish athermal effect of electric current from Joule heating effect during deformation, induction heat treatment (IHT) was conducted using a dilatometer equipment, which can precisely control the temperature of the specimen by an induction heater in a vacuum state. A specimen strained to 13% in the non-

pulsed tensile test was subjected to IHT. The engineering strain of 13% was selected based on the fracture elongation in non-pulsed tensile test at 70 °C. The temperature cycle of IHT was similar to that of pulsed tensile test, as shown in Fig. 2.5. Here, the time difference in pulsed period observed in Fig. 2.5 was caused because induction heater could not keep up with the momentary heating rate of temperature when a pulsed electric current applied to the specimen. However, note that the induction heat treated specimen was undergone under stronger temperature condition in perspective of thermal energy than temperature condition of specimen due to Joule heating during pulsed tensile test.

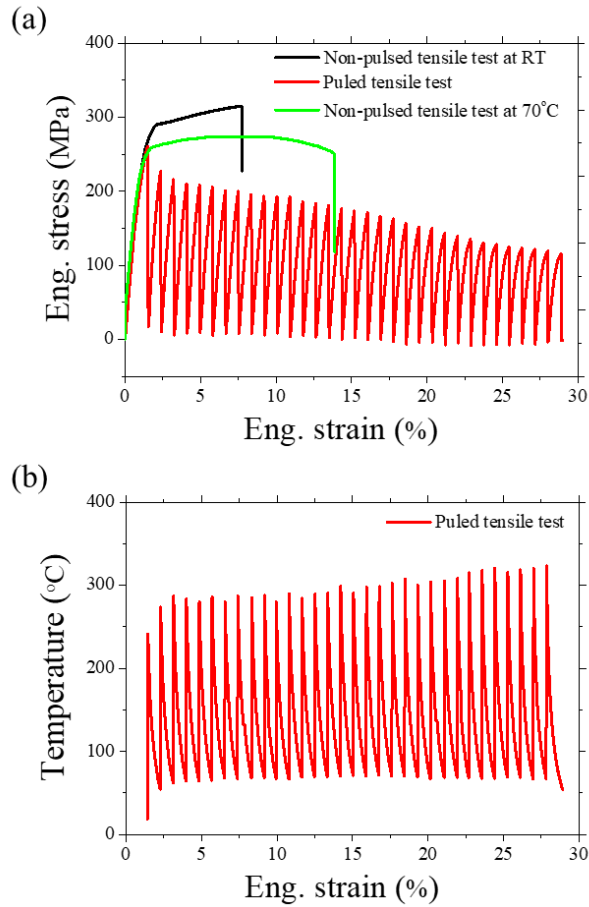


Figure 2.4 (a) Engineering stress-strain curves of non-pulsed tensile test at room temperature (RT, black line), non-pulsed tensile test at 70 °C (green line), and pulsed tensile test (red line) at the cross head speed of 1 mm/min. (b) The temperature of specimen measured during pulsed tensile test.

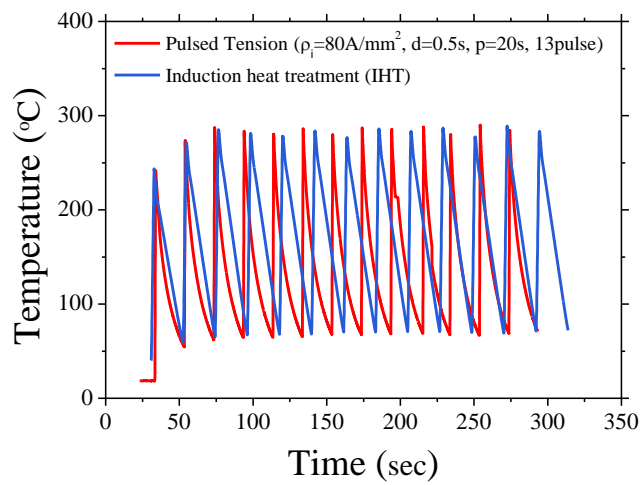


Figure 2.5 The temperature of specimen measured during pulsed tensile test until the engineering strain of 13% (red line) and induction heat treatment (IHT) using induction heater in a vacuum (blue line).

2.3.2 Microstructure analysis

Figures 2.6a, b, and c show the EBSD orientation maps and inverse pole figures (IPFs) obtained from as-extruded, IHT after non-pulsed tension at 70 °C, and pulsed tension, respectively. All specimens except for as-extruded specimen were strained to the engineering strain of 13%. The different colors in the orientation map indicate the orientation of each grain with respect to extrusion direction (ED). For the as-extruded specimen, a partially recrystallized microstructure consisting of fine dynamically recrystallized grains and elongated coarse un-recrystallized grains was observed. The un-recrystallized grain has a strong $\langle 10\text{-}10 \rangle$ texture parallel to the ED, as shown in Fig. 2.6a. For both the induction heat treated and pulsed tension specimens, it was observed that recrystallization and grain growth occurred. The maximum intensity values of IPFs for both the induction heat treated and pulsed tension specimens were 2.0 and 2.2, respectively, which were lower than that for the as-extruded specimen (7.5). It means that $\langle 10\text{-}10 \rangle$ texture becomes weak in both induction heat treated and pulsed tension specimens due to the decrease in the fraction of the un-recrystallized grains with a strong $\langle 10\text{-}10 \rangle$ texture. This result was consistent with previous works [24, 25]. However, the difference in texture between the induction heat treated specimen and pulsed tension specimen is not significant.

Figure 2.7 shows the grain orientation spread (GOS) maps and IPFs for recrystallized grains for the three specimens. The recrystallized area was identified based on the GOS values obtained from EBSD measurement [24]. The criterion of GOS value for identifying recrystallized grain was set to below 2°, which was

determined as average value of GOS in the specimens. When we consider only texture for the recrystallized grains, the maximum intensity values were almost similar among three specimens, as shown in Fig. 2.7. It means that there is no significant change in texture for three specimens under the given condition. Therefore, the effect of texture on strength and ductility of the alloy is not expected to be significant in this study.

Figure 2.8 shows the recrystallized grain size and area fraction obtained from GOS maps for three specimens. For both the induction heat treated and pulsed tension specimens, the recrystallized area fraction was clearly increased compared with the as-extruded specimen. It was also observed that the recrystallized area fraction and the grain size (91.6% and $11.6 \pm 4.0 \mu\text{m}$) of the induction heat treated specimen were larger than those (81.4% and $5.8 \pm 1.9 \mu\text{m}$) of the pulsed tension specimen. The influence of recrystallized area fraction and grain size on the mechanical property will be discussed later.

The black regions in all the specimens indicate the $\text{Mg}_{17}\text{Al}_{12}$ phases, as shown in Figs. 2.6 and 2.7. When compared with the as-extruded and induction heat treated specimen, a decrease in black region was identified in the pulsed tension specimen, as shown Fig. 2.6c. This implies that under the same temperature conditions, the pulsed tensile test results in a larger dissolution of $\text{Mg}_{17}\text{Al}_{12}$ phase and a finer grain size than the induction heat treated specimen.

In addition, the tensile behavior for as-extruded AZ91 alloy was affected by crack formation in the brittle $\text{Mg}_{17}\text{Al}_{12}$ phase. Fig. 2.9 shows SEM micrographs of

specimens after fracture during the non-pulsed tension at 70 °C and pulsed tension. Many cracks within the large elongated Mg₁₇Al₁₂ phase were observed in the non-pulsed tension at 70 °C. On the contrary, any cracks could not be found in the pulsed tension specimen. So, the tensile behavior in extruded AZ91 is dominantly affected by the crack initiation in the Mg₁₇Al₁₂ phase. The very high ductility of the AZ91 alloy during pulsed tensile test is mainly caused by the dissolution of Mg₁₇Al₁₂ phase.

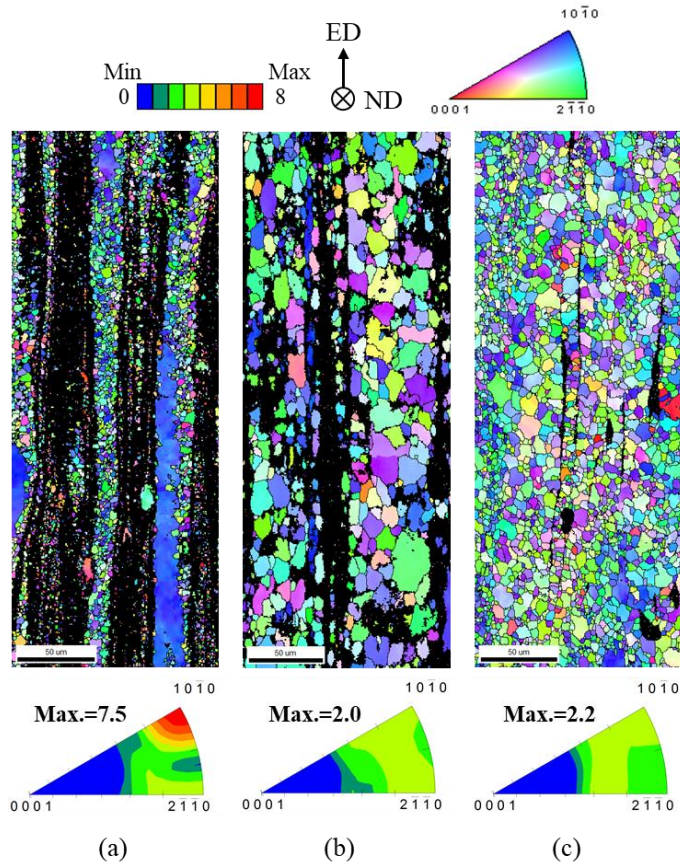


Figure 2.6 EBSD orientation maps and inverse pole figures (IPFs) for extrusion direction (ED // loading direction) obtained from (a) as-extruded, (b) induction heat treatment (IHT) after the non-pulsed tension at 70 °C, and (c) pulsed tension, at the engineering strain of 13%. (misorientation angle: 10°).

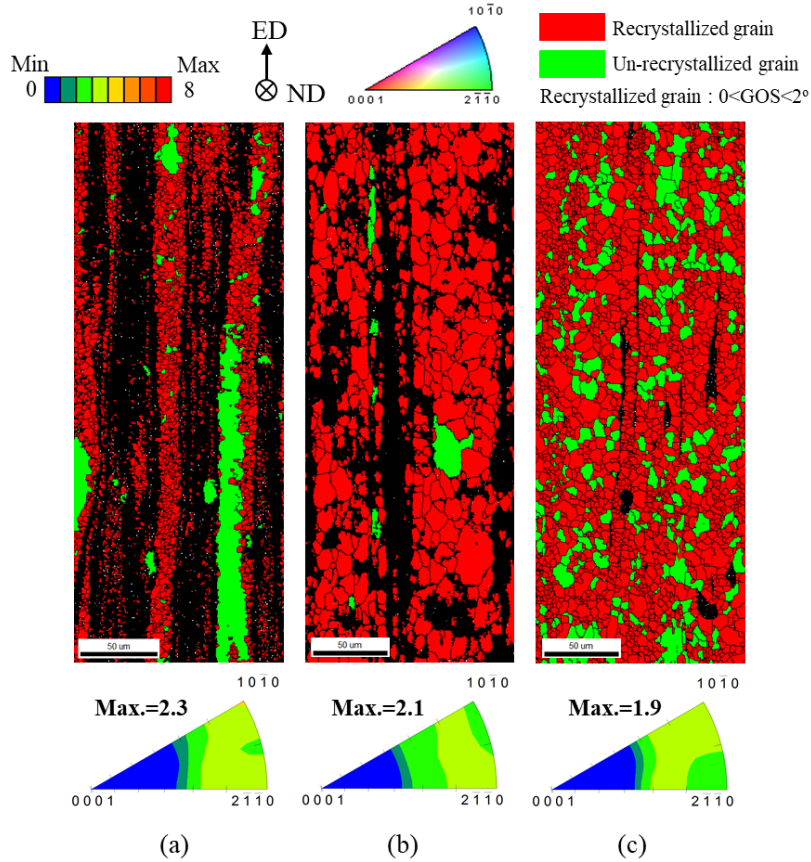


Figure 2.7 EBSD grain orientation spread (GOS) maps and IPFs for recrystallized grains obtained from (a) as-extruded, (b) induction heat treatment (IHT) after the non-pulsed tension at 70 °C, and (c) pulsed tension, at the engineering strain of 13%. (misorientation angle: 10°).

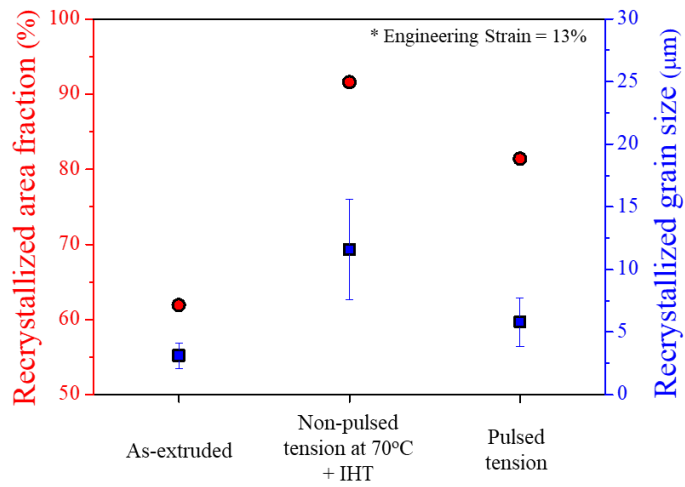


Figure 2.8 Recrystallized area fraction (in red circle, left axis) and grain size (in blue square, right axis) for each three specimens measured from GOS maps. (misorientation angle: 10°).

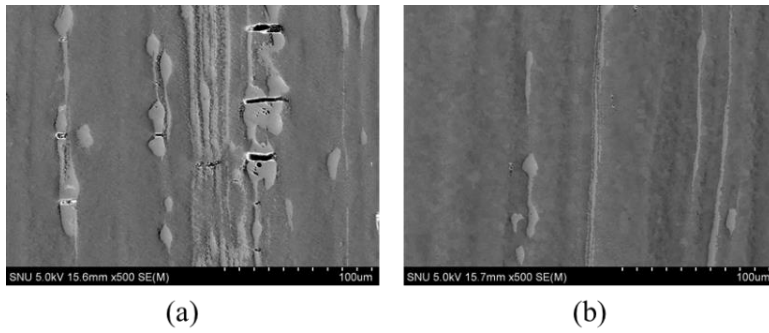


Figure 2.9 SEM micrographs after fracture for the (a) non-pulsed tension at 70 °C and (b) pulsed tension.

2.4 Electric current-induced dissolution

To investigate quantitatively dissolution effect of the $Mg_{17}Al_{12}$ phase during pulsed tensile test, the average fraction of $Mg_{17}Al_{12}$ phase was measured using SEM and EDS phase mapping analysis. A vertical direction of the observed surface, which is center position of the extruded specimen, is an ED. The yellow and green area in EDS phase map indicates $Mg_{17}Al_{12}$ phase and matrix, respectively. Fig. 2.10a shows the EDS phase map of as-extruded specimen. Large elongated $Mg_{17}Al_{12}$ phases along the ED were observed which shows a typical microstructure of as-extruded AZ91 alloy. The separation of the small $Mg_{17}Al_{12}$ particles from the elongated phase has been also observed. These small particles are directly formed by separation from the large $Mg_{17}Al_{12}$ eutectics during extrusion, as demonstrated by Li *et al.* [26]. These small particles and large elongated phases, which make the shape irregularity and interior defects, contribute to the lower ductility of specimen as shown in Fig. 2.4a. The average fraction of $Mg_{17}Al_{12}$ phase was measured to be $21.1 \pm 3.4\%$. Figs. 2.10b, c and d indicate the EDS phase maps of specimen obtained from non-pulsed tension at 70 °C, IHT after non-pulsed tension at 70 °C, and pulsed tension, respectively, at the engineering strain of 13%. When compared with the as-extruded specimen, large amount of $Mg_{17}Al_{12}$ phases were eliminated in the pulsed tension specimen.

Figure 2.10e shows the average $Mg_{17}Al_{12}$ phase fraction value measured from EDS phase maps at the engineering strains of 0%, 5%, and 13% for three tensile tests. In the non-pulsed tension at RT and 70 °C specimens, there is no noticeable change in the average fraction of $Mg_{17}Al_{12}$ phase. However, in the specimen subjected to the

pulsed tensile test, the average fraction of $Mg_{17}Al_{12}$ phase at the engineering strain of 5% was $13.0 \pm 2.2\%$. At engineering strain of 13%, the average fraction of $Mg_{17}Al_{12}$ phase was $9.0 \pm 1.4\%$ which is clearly lower than both non-pulsed tension at $70\text{ }^{\circ}\text{C}$ ($20.0 \pm 3.9\%$) and IHT after non-pulsed tension at $70\text{ }^{\circ}\text{C}$ ($16.8 \pm 3.0\%$). This shows that the amount of dissolved $Mg_{17}Al_{12}$ phase during pulsed tensile test was much larger than that during IHT even though the IHT was conducted identically with the temperature due to Joule heating during pulsed tensile test. Based on these results, it can be said that the dissolution of the $Mg_{17}Al_{12}$ phase can be also accelerated by applying electric current which is distinct from thermal effect due to Joule heating during plastic deformation.

Figure 2.11 shows that the dissolution of $Mg_{17}Al_{12}$ phase should affect the hardness of the specimen. The Vickers hardness of as-extruded specimen was $74.8 \pm 1.5\text{ HV}$. The hardness of the non-pulsed tension at $70\text{ }^{\circ}\text{C}$ at the engineering strain of 5% increased to $83.5 \pm 1.3\text{ HV}$. This is because the strain hardening effect is dominant at 5% strain despite the softening effect of temperature rise. The hardness of induction heat treated specimen was $68.1 \pm 2.3\text{ HV}$ which is lower than that of the non-pulsed tension at $70\text{ }^{\circ}\text{C}$ under the same engineering strain. This is because IHT decreases the $Mg_{17}Al_{12}$ phase fraction as mentioned in Fig. 2.10. The hardness of the specimen subjected to the pulsed tensile test until the engineering strain of 13%, $64.9 \pm 2.8\text{ HV}$, was much lower than that of induction heat treated specimen at the same strain. It is well known that the hardness value increases with decrease in grain size and recrystallized area fraction for metal alloys [27]. However, the hardness

value of pulsed tension specimen was clearly lower than that of induction heat treated specimen despite the lower recrystallized area fraction and the smaller grain size than induction heat treated specimen, as shown in Figs. 2.8 and 2.11 This indicates that the recrystallized grain size and area fraction effects were not dominant effects on the mechanical property. When compared to the induction heat treated specimen, the lower fraction of $Mg_{17}Al_{12}$ phase in the pulsed tension specimen was shown in Fig. 2.10e. So, the lower hardness of the pulsed tension specimen can be explained by acceleration of dissolution of $Mg_{17}Al_{12}$ phase during pulsed tension.

In addition, the tensile behavior for as-extruded AZ91 alloy is affected by crack formation in the brittle $Mg_{17}Al_{12}$ phase. As indicated by arrows in Figs. 2.10b and 2.10c, many cracks within the large elongated $Mg_{17}Al_{12}$ phase were observed in the non-pulsed tension at 70 °C. This obviously shows that the brittle $Mg_{17}Al_{12}$ phase is vulnerable to crack propagation and acts as barriers to dislocation movement, as previously indicated by Wang *et al.* [28]. On the contrary, any cracks could not be found in the pulsed tension specimen, as shown in Fig. 2.10d. So, the tensile behavior in extruded AZ91 is dominantly affected by the crack initiation in the $Mg_{17}Al_{12}$ phase. The very high ductility of the AZ91 alloy during pulsed tensile test is mainly caused by the dissolution of $Mg_{17}Al_{12}$ phase.

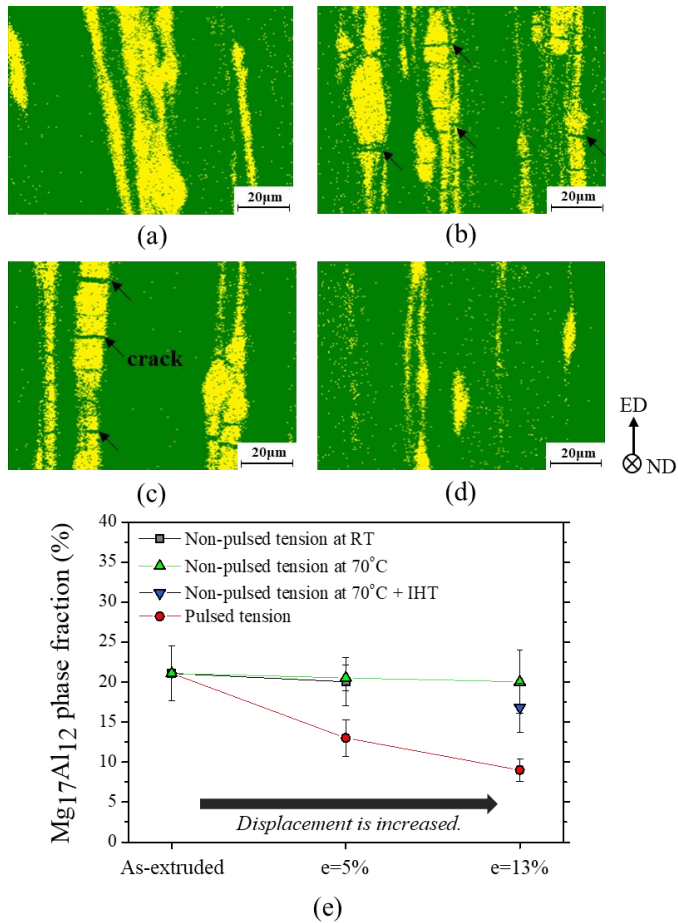


Figure 2.10 EDS phase maps of specimens obtained from (a) as-extruded, (b) non-pulsed tension at 70 °C, (c) induction heat treatment (IHT) after the non-pulsed tension at 70 °C, and (d) pulsed tension, at the engineering strain of 13% (yellow area: $Mg_{17}Al_{12}$, green area: Matrix). The arrows indicate crack within $Mg_{17}Al_{12}$ phase. (e) The average fraction of $Mg_{17}Al_{12}$ phase for the specimens at engineering strain of 0%, 5%, and 13% obtained from non-pulsed tension at RT (rectangle symbols), non-pulsed tension at 70 °C (triangle symbols), and pulsed tension (circle symbols).

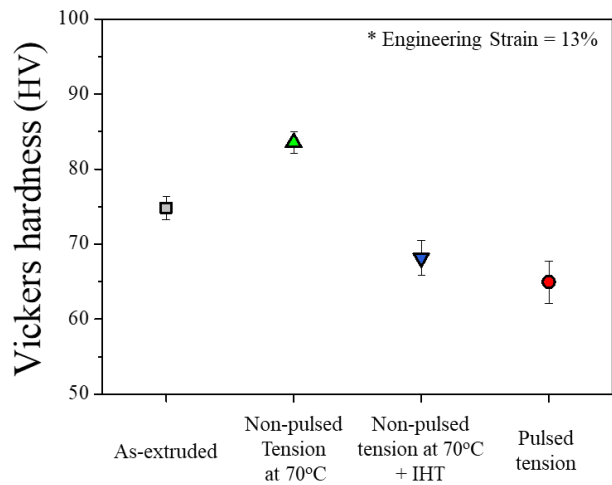


Figure 2.11 Vickers Hardness (HV) measurement of specimen obtained from the non-pulsed tension at 70 °C (triangle symbol), IHT after the non-pulsed tension at 70 °C (inverted triangle symbol), and pulsed tension (circle symbol) at the engineering strain of 13% compared to the as-extruded specimen (rectangle symbol).

2.5 Electropulsing treatment (EPT) vs conventional heat treatment (CHT)

To identify the athermal effect by applying electric current on the dissolution of the $Mg_{17}Al_{12}$ phase without deformation, heat treatment (HT) at 350 °C and 400 °C during 10 minutes was conducted by both electropulsing treatment (EPT) and conventional heat treatment (CHT). Fig. 2.12a shows the average fraction of $Mg_{17}Al_{12}$ phase measured at each condition for EPT and CHT specimens. In both EPT and CHT, the average fraction of $Mg_{17}Al_{12}$ phase commonly decreased with increasing temperature. However, when compared with CHT, the average fraction of $Mg_{17}Al_{12}$ phase in EPT was much lower at the given same temperature condition. At the condition of 350 °C, the average fraction of $Mg_{17}Al_{12}$ phase in EPT was $7.8\pm 0.3\%$ which is lower than that in CHT ($11.4\pm 0.6\%$). At the condition of 400 °C, the average fraction of $Mg_{17}Al_{12}$ phase in EPT was $3.9\pm 0.5\%$ which is about half of that in CHT ($7.0\pm 0.5\%$). From this result, it was identified that the amount of $Mg_{17}Al_{12}$ phase dissolved during EPT is significantly larger than that during CHT.

Figure 2.12b shows the Vickers hardness values of the specimens subjected to the EPT and CHT. Through the CHT, the hardness value decreased from 67.5 ± 1.4 HV to 60.0 ± 2.0 HV with increasing temperature from 350 °C to 400 °C. These hardness values were lower than that of as-extruded specimen (74.8 ± 1.5 HV). However, for the EPT, the hardness values were 63.1 ± 1.6 HV and 55.7 ± 1.6 HV at the temperature condition of 350 °C and 400 °C, respectively, which were clearly

lower than that of the CHT at the same temperatures. This hardness trend was consistent with the trend of the average fraction of $Mg_{17}Al_{12}$ phase. It means that electric current accelerates the dissolution of $Mg_{17}Al_{12}$ phase even in the absence of Joule heating.

On the basis of the experimental results in the present study, it is identified that applying electric current during deformation can accelerate microstructural change through atomic diffusion such as the dissolution of the $Mg_{17}Al_{12}$ phase with a distinct effect from Joule heating. Furthermore, our results can provide that it is possible to apply of EAM technique to forming process of AZ91 alloy without additional dissolution heat treatment process. It implies that EAM can save a lot of energy and time for forming of AZ91 alloy in process because additional dissolution heat treatment process is not required.

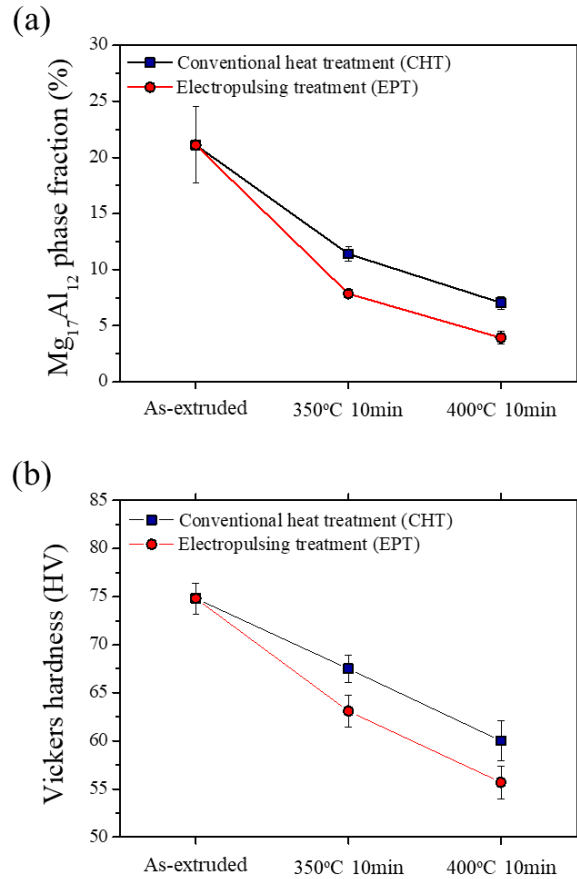


Figure 2.12 (a) The average fraction of $Mg_{17}Al_{12}$ phase and (b) Vickers Hardness (HV) measurement of as-extruded specimen, the conventional heat treated specimen, and the electropulsing treated specimen under each condition of 350 °C and 400 °C for 10 min.

2.6 Conclusion

In this chapter, the effect of electric current on dissolution of $Mg_{17}Al_{12}$ phase in as-extruded AZ91 magnesium alloy was investigated by uniaxial tensile test and heat treatment based on microstructural analysis. When a pulsed electric current was applied to the specimen during plastic deformation, the flow stress substantially decreased and the elongation at fracture increased 3.7 times compared to the non-pulsed tensile test at RT. From EBSD and EDS phase mapping analysis, it was observed that the average fraction of $Mg_{17}Al_{12}$ phase dissolved during pulsed tensile test was much larger than that during IHT. In addition, the Vickers hardness value of specimen subjected to pulsed tensile test was clearly lower than that of induction heat treated specimen. These results support sufficiently that dissolution of the $Mg_{17}Al_{12}$ phase occurs by both thermal effect due to Joule heating and athermal effect of electric current during pulsed tensile test. The athermal effect of electric current on dissolution of the $Mg_{17}Al_{12}$ phase was demonstrated by comparing $Mg_{17}Al_{12}$ phase fractions after EPT and CHT. The dissolved phase fraction after EPT was times higher than CHT. It can be understood that applying electric current can accelerate the dissolution of the $Mg_{17}Al_{12}$ phase with a distinct effect from Joule heating. The application of EAM technique to forming of as-extruded AZ91 magnesium alloy can provide a high efficiency in forming process because additional dissolution heat treatment can be omitted.

2.7 References

- [1] S. Celotto, *Acta Mater.*, 48 (2000) 1775.
- [2] S. W. Xu, N. Matsumoto, S. Kamado, T. Honma, Y. Kojima, *Mater. Sci. Eng. A*, 523 (2009) 47.
- [3] B. L. Mordike, T. Ebert, *Mater. Sci. Eng. A*, 302 (2001) 37.
- [4] H. Friedrich, S. Shumann, *Mater. Proc. Technol.*, 117 (2001) 276.
- [5] Z. Zhang, A. Courture, A. Luo, *Scr. Mater.*, 39 (1998) 45.
- [6] Y. Z. Lu, Q. D. Wang, W. J. Ding, X. Q. Zeng, Y. P. Zhu, *Mater. Lett.*, 44 (2000) 265.
- [7] I. J. Polmear, *Mater. Sci. Technol.*, 10 (1994) 1.
- [8] I. J. Polmear, *Mater. Trans.*, 37 (1996) 12.
- [9] Y. Jiang, L. Guan, G. Tang, C. Shek, Z. Zhang, *Mater. Sci. Eng. A*, 528 (2011) 5627.
- [10] E. I. Samuel, A. Bhowmik, *J. Mater. Res.*, 25 (2010) 1020.
- [11] M.-S. Kim, N. T. Vinh, H.-H. Yu, S.-T. Hong, H.-W Lee, M.-J. Kim, H. N. Han, J. T. Roth, *Int. J. Precis. Eng. Manuf.*, 15 (2014) 1207.
- [12] Y. Jiang, G. Tang, L. Guan, S. Wang, Z. Xu, C. Shek, Y. Zhu, *J. Mater. Res.*, 23 (2008) 2685.
- [13] Y. Jiang, G. Tang, C. Shek, Y. Zhu, L. Guan, S. Wang, Z. Xu, *J. Mater. Res.*, 24 (2009) 1810.
- [14] Y. Z. Zhou, *Phil. Mag. Lett.*, 84 (2004) 341.
- [15] Y. Jiang, G. Tang, C. Shek, Y. Zhu, Z. Xu, *Acta Mater.*, 57 (2009) 4797.

- [16] Y. Jiang, G. Tang, C. Shek, W. Liu, *J. Alloys Compd.*, 509 (2011) 4308,
- [17] X. N. Du, S. M. Yin, S. C. Liu, B. Q. Wang, J. D. Guo, *J. Mater. Res.*, 23 (2008) 1570.
- [18] Z. Q. Wang, Y. B. Zhong, Z. S. Lei, W. L. Ren, Z. M. Ren, K. Deng, *J. Alloys Compd.*, 471 (2009) 172.
- [19] Y. H. Zhu, S. To, W. B. Lee, X. M. Liu, Y. B. Jiang, G. Y. Tang, *Mater. Sci. Eng. A*, 501 (2009) 125.
- [20] M.-J. Kim, K. Lee, K. H. Oh, I. S. Choi, H. H. Yu, S.-T. Hong, H. N. Han, *Scr. Mater.*, 75 (2014) 58.
- [21] M.-J. Kim, M.-G. Lee, K. Hariharan, S.-T. Hong, I.-S. Choi, D. Y. Kim, K. H. Oh, H. N. Han, *Int. J. Plast.*, 94 (2017) 148.
- [22] Y. J. Lee, H.-M. Sung, Y. G. Jin, K. H. Lee, C. R. Park, G.-H. Kim, H. N. Han, *Int. J. Refract. Met. Hard Mater.*, 60 (2016) 99.
- [23] T. Zhu, Z. W. Chen, W. Gao, *J. Mater. Eng. Perform.*, 860 (2010) 860.
- [24] H. Yu, S. H. Park, B. S. You, *J. Mater. Process. Technol.*, 224 (2015) 181.
- [25] H. Ding, L. Liu, S. Kamado, W. Ding, Y. Kojima, *J. Alloys Compd.*, 456 (2008) 400.
- [26] Z. Li, J. Dong, X. Q. Zeng, C. Lu, W. J. Ding, *Mater. Sci. Eng. A*, 466 (2007) 134.
- [27] S. H. Hwan, C. Park, Y. S. Sato, H. Kokawa, *J. Mater. Sci.*, 38 (2003) 4379.
- [28] R. M. Wang, A. Eliezer, E. Gutman, *Mater. Sci. Eng. A*, 344 (2002) 279.

Chapter 3

Electric current-induced phenomena in TRIP-aided steel

3.1 Introduction

Recently, demands for weight reduction in many automotive industries have been driving the development of advanced high-strength steels (AHSSs) with high strength-to-weight ratios. This is due not only to improvements in fuel efficiency, but also to the consumer's increasing demand for safer and more comfortable vehicle [1, 2]. To satisfy these demands, steel makers are trying to increase the strength of steels without significantly deteriorating their ductility by generating multiphase microstructures [3, 4]. One of the various AHSSs containing multiphase is transformation-induced plasticity (TRIP)-aided steel, which consists of a ferrite, metastable retained austenite, bainite, and martensite phases [5, 6]. Note that TRIP refers to a phenomenon in which a permanent strain remains after the solid-solid phase transformation under external stress [7, 8]. The retained austenite phase in the TRIP-aided steel transforms into hard martensite phase, which is induced mechanically by an external stress or strain, leading to higher ductility due to a delay effect of necking (TRIP effect) [9]. This phase transformation proceeding by an external stress or strain is hereafter denoted as the mechanically induced martensitic transformation (MIMT). Thus, TRIP-aided steels containing a large volume fraction

of retained austenite phase are preferred types of AHSSs [10].

However, TRIP-aided steel with a high strength still shows large springback and forming load during forming, which make it difficult for automakers to manufacture automotive parts in desired shapes with a reasonable cost. Furthermore, for TRIP-aided steel, it is well established that the MIMT effect takes place between the M_s (martensite start temperature) and the M_d (stress-induced martensite start temperature), above which the austenite becomes completely stable [11–13]. Therefore, there is a temperature between M_s and M_d , at which the MIMT effect is suppressed moderately and the resultant strain hardenability is held in a large strain range, leading to maximum benefit of the MIMT effect. However, in terms of warm and hot forming process, the process temperature, which is generally between 550 and 850 °C, is higher than M_d (200–400 °C) [14]. Thus, the MIMT effect could not work properly in the hot forming process of the TRIP-aided steels. Additionally, the hot forming process inevitably induces increased adhesion between the material and the die, decreased die strength, surface oxidation, and low production efficiency.

To overcome these problems, the EAM technique can be suggested as a promising new forming method for TRIP-aided steels. Recently, there have been many cases of applying electric current to high-strength steels [15–19]. Tang *et al.* reported that the drawing stress of stainless steel wire was decreased by approximately 20–50% with the application of electric current pulses, showing the improvement in plasticity [15]. Kim *et al.* studied the effect of electric current density on the mechanical properties of AHSS under quasi-static tensile loads [16].

The authors reported that the electric current can be effectively used to reduce the springback of the material. Lu and Qin also investigated the effect of electric current on the tempering of martensite in dual-phase steels [17]. The authors indicated that high electric current can significantly enhance the strength of tempered dual-phase steels via the formation of ultrafine-grained ferrite with nanocementite particles.

Based on the positive effects of electric current on the plastic deformation, Liu *et al.* applied the electric current to TRIP-aided steel during tensile test [20]. However, the authors observed that the ductility was not improved by applying electric current, despite of the reduction in flow stress. This was explained by the suppression of the MIMT effect due to the increased temperature [20]. Unfortunately, the technique, which can improve the formability of TRIP-aided steel by applying electric current, has not been developed until now.

In this chapter, the effect of electric current on the MIMT during tensile deformation is investigated and a modified pulsing pattern of electric current is suggested based on the microstructural observation to improve the formability of TRIP-aided steel.

3.2 Experimental procedure

3.2.1 Specimen preparation

The chemical composition of the investigated TRIP-aided steel is Fe-0.35C-3.68Mn-0.19Si-5.27Al in wt.%. The higher Al content in this alloy than other conventional TRIP-aided steels provides a density reduction effect by means of substitution and lattice expansion. Typical tensile specimens (ASTM-E08) with a gauge width of 6.25 mm, thickness of 1 mm, and gauge length of 25 mm were fabricated along the rolling direction (RD) of the sheet.

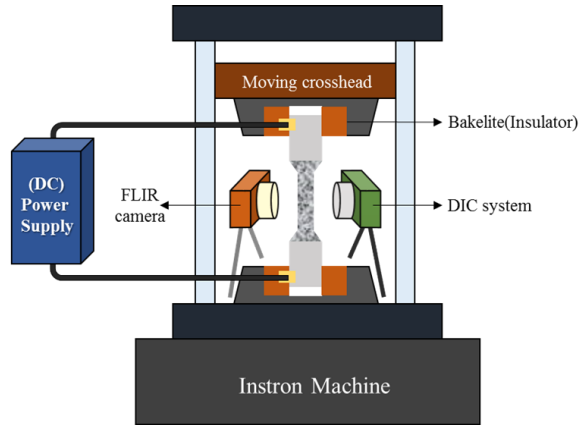
3.2.2 Experimental set-up

Quasi-static uniaxial tensile tests were conducted using the experimental set-up described in Fig. 3.1a with a constant crosshead speed of 1.5 mm/min (corresponding to the nominal strain rate of 1×10^{-3} /s) at room temperature (RT, 25 °C). The tensile test machine (INSTRON 5584, USA) was modified to apply electric current only through the specimen by inserting Bakelite (Insulator) between the specimen and each grip. The displacement of the specimen was measured by ARAMIS Digital Image Correlation (DIC) system (GOM, Germany), which provides non-contact measurement based on the principle of digital image correlation. Note that the experimental set-up described in Fig. 3.1a is identical to that described in the previous chapter.

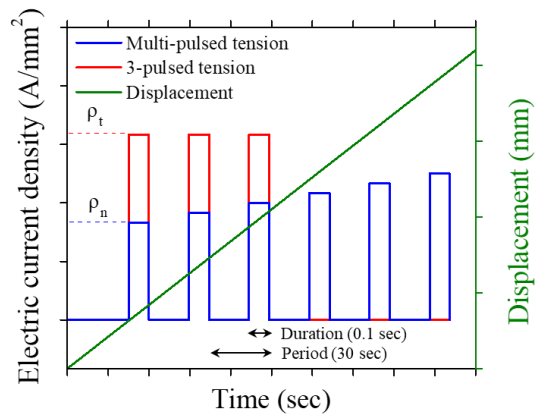
The pulsed tensile tests were carried out by using two pulsing patterns of electric current, and the electric current was generated by a Vadal SP-1000U welder (Hyosung, South Korea). First, the electric current was periodically applied to the specimen with a duration (t_d) of 0.1 s and a period (t_p) of 30 s during deformation (multi-pulsed tension), as schematically shown in Fig. 3.1b. The first pulse of electric current was applied immediately before yielding. The amplitude of the electric current was selected to induce a nominal electric current density (ρ_n) of 50 A/mm² based on the original cross-sectional area of the specimen. Note that as the specimen is continuously deformed by tension, the cross sectional area of the gage continuously decreases. Therefore, with the constant amplitude of electric current, the true electric current density (ρ_t) based on the actual cross-sectional area for each

pulse of electric current continuously increases. Second, the tensile test with 3 pulses of electric current (3-pulsed tension) was conducted under the condition of a duration (t_d) of 0.1 s and a true electric current density (ρ_t) of 95 A/mm², as schematically shown in Fig. 3.1b. The first pulse of electric current was applied immediately before yielding. 3 pulses of electric current were applied to the specimen only in the early stage of deformation, when the phase transformation of retained austenite phase begins to take place. In order to maintain a constant electric current density (ρ_t) based on the initial cross-sectional area of the specimen, a different amplitude of electric current was applied to the specimen considering the decrease in cross-sectional area of the specimen during deformation.

The non-pulsed tensions at high temperature were also performed using the same tensile machine with an environmental chamber at cross-head speed 1.5 mm/min. Target temperatures were set to 100 and 200 °C, which cover the temperature range measured during the multi-pulsed and 3-pulsed tension, to evaluate the thermal effect due to Joule heating on the mechanical behavior. Test was performed after the target temperature was reached. The temperature change of the specimen during the pulsed tensile test was measured using an FLIR-E40 infra-red (IR) thermal imaging camera (FLIR, Sweden). One side of the specimen was sprayed with black thermal paint to stabilize the emissivity and thus to improve the accuracy of temperature measurement. The emissivity was calibrated by comparing the measured temperature using a K-type thermocouple.



(a)



(b)

Figure 3.1 Schematics of (a) experimental set-up for non-pulsed/pulsed tensile tests and (b) two types pulsing conditions applied to the specimen during uniaxial tensile test.

3.2.3 Microstructure observation

The microstructure of the initial specimen was characterized by a JXA- 8530F electron probe microanalyzer (EPMA, JEOL Ltd., Japan) and a field emission gun scanning electron microscope (FE-SEM, SU70, Hitachi, Japan) equipped with an electron backscatter diffraction (EBSD) system (EDAX/TSL, Hikari, USA). To calculate the M_s temperature, the quantities of C, Al, Si, and Mn in the retained austenite phase were obtained from the EPMA analysis. The X-ray diffraction (XRD) measurement was carried out using a Lab X-ray diffractometer (Smart Lab, Rigaku, Japan) with a Mo radiation source operating at 50 kV at RT. The diffraction patterns were recorded in the angular range of 18–36° with a scan rate of 1 °/min. To check the change in dislocation density during the pulsed tensile test, the full width at half maximum (FWHM) value was obtained from the X-ray diffraction peak data. The diffraction peaks could be fitted well with the Pseudo-Voigt function. In order to measure the fraction of the retained austenite phase, a Rietveld refinement was performed for all specimens using the TOPAS (version 4.2) software package. The specimens for microstructure observation were prepared by mechanical grinding followed by electropolishing with a 100 ml perchloric acid and 900 ml ethanol solution. For the EBSD analysis, the accelerating voltage and scan step size were 15 kV and 0.4 μm , respectively. The critical misorientation angle was set to 15° for grain identification.

3.2.4 Model for mechanically induced martensitic transformation (MIMT) kinetics

In addition to the experimental measurement of the retained austenite phase fraction, a calculation of the MIMT kinetics in both non-pulsed and pulsed tensions was performed using the model, which was derived based on the concept of energetically favorable variant selection under an external stress field [21]. In this model, the chemical free energy change, ΔG , and the entropy change, ΔS , were defined in terms of the thermodynamic theory for the austenite-to-martensite transformation. The mechanical interaction energy, U^i , for the i th martensitic variant between the externally applied stress and the lattice deformation in austenite during phase transformation can be defined as the product of applied stress and the transformation strain for the i th martensitic variant. Han *et al.* derived the following expression for the increment of the extended martensite volume fraction in the retained austenite, df_{ex}^i [21]:

$$df_{ex}^i = A^i d\bar{\epsilon}_a^P + Bd(XH(-dX))H(-dX)H[(\Delta G^C - X)] \quad (3.1)$$

where X is $\Delta G + U^i$ and $d\bar{\epsilon}_a^P$ is the effective plastic strain increment accumulated in the parent austenite. In the present study, the value of $d\bar{\epsilon}_a^P$ was calculated reflecting strain partitioning effect during deformation based on the ratio of the hardness value for each phase in the TRIP-aided steel. Thus, the value of $d\bar{\epsilon}_a^P$ was calculated using the following equation:

$$d\bar{\epsilon}_{total}^P = d\bar{\epsilon}_f^P + d\bar{\epsilon}_a^P + d\bar{\epsilon}_m^P \quad (3.2)$$

where $d\bar{\epsilon}_{total}^P$, $d\bar{\epsilon}_f^P$, and $d\bar{\epsilon}_m^P$ are the total plastic strain increment, the effective

plastic strain increments accumulated in the ferrite and martensite phases, respectively. The $d\bar{\varepsilon}_{total}^P$ value was taken from the experimental data obtained from the true stress-strain curve. It was reported that the nanohardness value of the martensite phase is four times higher than that of the ferrite phase [22]. Thus, the effective plastic strain during tensile deformation was assumed to be inversely proportional to the hardness of each phase. For the simplicity of calculation, it was also assumed that the hardness of the ferrite phase is the same as that of the austenite phase. In Eq. (3.1), H is the Heaviside step function, reflecting the fact that the martensitic transformation can occur when the driving force exceeds the critical free energy. ΔG should be defined as a function of temperature. ΔG^C is known to be 2100 J/mol regardless of chemical composition according to Jaccin and Beyer [23]. Under the assumption that ΔG is a linear function of temperature, ΔG and ΔS can be derived as follows:

$$\Delta G = \Delta G^C + \Delta S(T - M_s) \quad (3.3)$$

$$\Delta S = -\Delta G^C / (T_0 - M_s) \quad (3.4)$$

where T_0 is the temperature at which the difference in the chemical free energy between austenite and martensite is zero. The T_0 temperature was obtained by a CALPHAD method [24]. The M_s temperature of the retained austenite phase in this material was -22 °C, and the details about M_s will be discussed in the Chapter 3.3.1.

For the temperature, T , the experimentally measured temperature data should be reflected as an input value. However, for a duration time of 0.1 s when the electric current was applied, it should not be calculated solely based on the measured

temperature due to Joule heating. According to previous studies [25–28], it was commonly indicated that the athermal effect of electric current can obviously accelerate the microstructural changes through atomic diffusion, which is distinct from the thermal effect due to Joule heating. However, it is difficult to separate the athermal effect of electric current on MIMT kinetics from thermal effect during application of electric current in this study. Therefore, the calculation was performed only for the region where the electric current was eliminated.

Additionally, the functions of A and B in Eq. (3.1) were derived on the basis of the observation that the strain-induced nucleation occurs predominantly at shear-band intersections [29, 30]. They are expressed by the following formulas [21]:

$$A^i = -\frac{0.011\alpha\delta\gamma(f_{sb})^{r-1}(1-f_{sb})^r}{24\Delta S}(\Delta G + U^i) \quad (3.5)$$

$$B = -\frac{0.011[1+\delta(f_{sb})^r]}{24\Delta S} \quad (3.6)$$

where α is the shear-band formation rate, and δ and γ are the geometric constants. f_{sb} is the volume fraction of shear-bands. It is known that the parameter on the rate of shear-band formation, α , decreases with increasing temperature [29, 30]. These three material's parameters were adjusted to give the best agreement between the experimental data and calculated transformation kinetics data.

Thus, based on the extension of the classical Johnson-Mehl-Avrami-Kolmogorov (JMAK) theory for the simultaneous decomposition of austenite [31], the real volume fraction of i th martensitic variant at time, $t+dt$, can be obtained as:

$$f_{t+dt}^i = f_t^i + df^i \quad (3.7)$$

$$df^i = \left(1 - \sum_{i=1}^{24} f_{t+dt}^i\right) df_{ex}^i \quad (3.8)$$

Then, the total volume fraction of martensite in the retained austenite then becomes:

$$f = \sum_{i=1}^{24} f^i \quad (3.9)$$

where f refers to the volume fraction of the martensite transformed from one parent austenite.

Finally, the total volume fraction of martensite, X_m , in the TRIP-aided steel specimen can be obtained as:

$$X_m = X_a^I f \quad (3.10)$$

where X_a^I is the initial volume fraction of retained austenite in the TRIP-aided steel.

Based on the above MIMT kinetic model, the MIMT kinetics for the given test conditions were calculated. The reliability of the experimental data for the retained austenite phase fraction was improved by comparing between the experimental data (symbols) and calculated data (lines) for the phase transformation kinetics. The material's parameters in Eq. (3.5) obtained from the result of non-puled tension at RT are listed in Table 3.1 and used in the calculation of MIMT kinetics for all test conditions.

Table 3.1 Material's parameters in Eq. (3.5) for the investigated TRIP-aided steel.

α	δ	r	T_0 (°C)	M_s (°C)
$3244 \exp[-0.0208(T + 273)]$	0.25	3.44	532	-22

3.3 Effect of electric current on the mechanical behavior and microstructure

3.3.1 Initial properties

Figures 3.2a and b show the EBSD inverse pole figure (IPF) and phase maps for the investigated TRIP-aided steel, respectively. The different colors in the IPF map indicate the orientation of each grain with respect to normal direction (ND). The initial specimen consists of a ferrite matrix (green area) with some retained austenite grains (red area). The average grain sizes of the ferrite and retained austenite phase were 7.2 and 2.0 μm , respectively. The volume fraction of these retained austenite phase is 24.5%, which was measured from EBSD analysis (Fig. 3.2a). In order to ensure the reliability and accuracy of the data, an additional XRD measurement was conducted. The X-ray diffraction pattern of the initial specimen was presented in Fig. 3.2b. The (111), (200), and (220) peaks of the austenite phase were identified under the given measurement condition. The (110), (200), and (210) peaks of the ferrite phase were also identified. Through the Rietveld method using TOPAS, the volume fraction of austenite phase was determined to be approximately 26.5%. The discrepancy of the phase fraction might originate from the limitation of the EBSD analysis, which is performed only on the surface of the specimen. Thus, the value obtained from XRD measurement (26.5%) was used as reference value in this study.

Figure 3.3 shows the backscattered electron micrograph and distributions of C, Al, Si, and Mn in the initial specimen which were obtained from the EPMA analysis.

As a result, the measured concentrations of C, Mn, Al, and Si in the retained austenite phase were 1.21, 5.76, 4.18, and 0.06 wt.%, respectively. The concentrations of C and Mn in the retained austenite phase were much higher than the nominal concentration (0.35 and 3.68 wt.%, respectively), as shown in Figs. 3.3b and c. This showed good agreement with the fact that C and Mn concentrate in the retained austenite phase accompanying the ferrite and bainite phase transformation for TRIP-aided steels [32]. On the contrary, it was observed that Al and Si were slightly concentrated on the ferrite phase compared with the retained austenite, as shown in Figs. 3.3d and e.

Based on the concentration of elements in the retained austenite phase determined quantitatively from the EPMA analysis, the M_s temperature of the retained austenite in this material was calculated to be -22 °C using the following equation [33]:

$$M_s(^{\circ}\text{C}) = 539 - 423C - 30.4Mn - 7.5Si + 30Al \quad (3.11)$$

where C, Mn, Si, and Al are the contents of these elements in wt.%. It is clear that the M_s temperature is lower than the RT (25 °C). Thus, the austenite phase in the investigated TRIP-aided steel can remain metastable at RT.

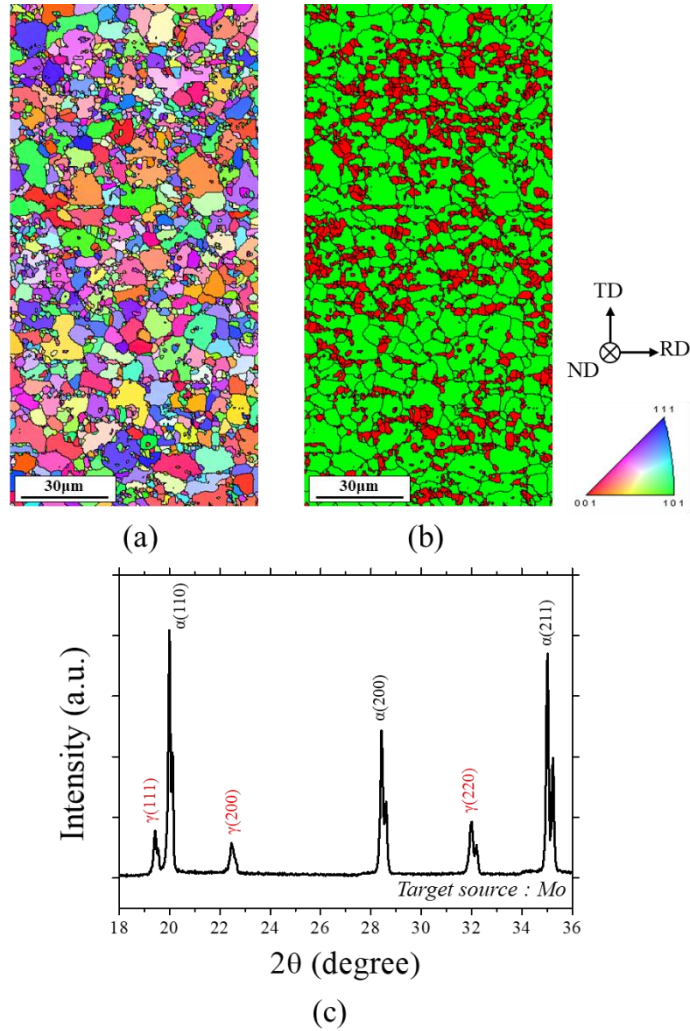


Figure 3.2 (a) EBSD inverse pole figure map for normal direction (ND), (b) EBSD phase map (red area: retained austenite phase, green area: ferrite matrix), and (c) X-ray diffraction pattern in the range of 18-36° for the investigated TRIP-aided steel.

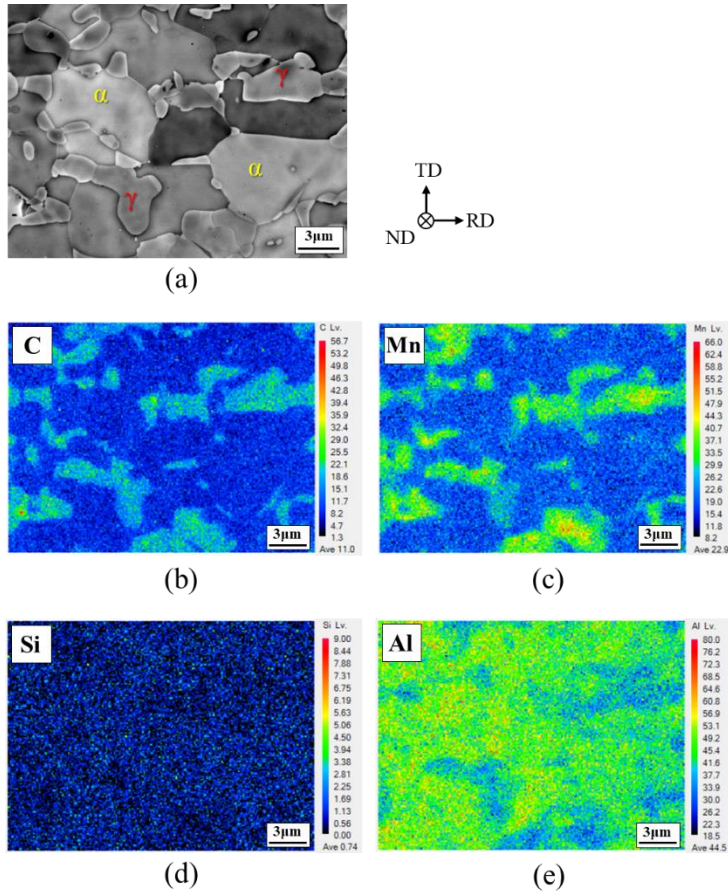


Figure 3.3 Elements distribution in the initial specimen: (a) backscattered electron image, (b) C distribution, (c) Al distribution, (d) Si distribution, and (e) Mn distribution.

3.3.2 Mechanical behavior

In the non-pulsed tension, the specimen showed strain hardening after yielding at ~500 MPa and failed by fracture at the true strain of 0.33, as shown in Fig. 3.4a. In the multi-pulsed tension, the flow stress decreased rapidly immediately after each pulse and then increased owing to strain hardening until the next pulse, as shown in Fig. 3.4a. The decrease in flow stress by applied electric current is known to be caused by thermal and athermal effects. When compared to the non-pulsed specimen, the multi-pulsed specimen showed a reduction in ductility in spite of the decrease in flow stress. The elongation decreased from 0.33 to 0.26. Under the non-pulsed tension at 100 °C, the flow stress decreased and the elongation also decreased from 0.33 to 0.25, compared with the non-pulsed tension at RT. There is no significant difference between the multi-pulsed tension and non-pulsed tension at 100 °C with respect to the flow stress and elongation at fracture.

The measured specimen temperature during the multi-pulsed tension is presented in the Fig. 3.4b. During an electric pulse application, the specimen temperature increased instantly due to the Joule heating effect. After applying the electric pulse, the specimen temperature decreased by air cooling until the next pulse. The peak value of the measured temperature showed a steady increase owing to the continuously increasing true electric current density with decreasing cross-sectional area during deformation.

For the multi-pulsed tension and non-pulsed tension at 100 °C, it was observed that the slope of true stress-strain curve noticeably changed in comparison with the

non-pulsed tension at RT. The slope of the stress-strain curve indicates the strain hardening rate, which is called the strain hardening exponent (n). The strain hardening exponent can be expressed as true stress (σ) and true strain (ϵ).

$$n = \frac{d \ln \sigma}{d \ln \epsilon}$$

The change in hardening rate of TRIP-aided steels is related to the volume fraction of mechanically induced martensite phase [10,12]. The increase in the fraction of the hard martensite phase with increasing true strain induces the increase in the hardening rate. This increase in the hardening rate due to the fraction of hard martensite phase is denoted as phase hardening, according to Han *et al.* [12].

To check the influence of electric current on the phase hardening effect, the strain hardening exponent was calculated and plotted as a function of true strain in Fig. 3.5a. In the non-pulsed tension at RT, the strain hardening exponent increased until the true strain was approximately 0.2, and the maximum value was approximately 0.4. However, in the non-pulsed tension at 100 °C, the value of strain hardening exponent gradually decreased as the deformation progressed. For the multi-pulsed tension, it is difficult to compare the strain hardening exponent properly due to the stress drop phenomenon caused by applying periodic electric current. Thus, considering only the maximum flow stress points in the strain hardening zones where the electric current was eliminated, the strain hardening exponent values were calculated and are shown as symbols in Fig. 3.5a. The line connecting the symbols is presented by the dotted line in Fig. 3.5a. It was identified that the strain hardening

exponent value under the multi-pulsed tension was significantly lower than that under the non-pulsed tension at RT, although it showed a slight increase as the deformation progressed. This suggests that the phase hardening effect did not occur, owing to the suppression of the MIMT effect caused by a temperature increase under the given condition of multi-pulsed tension.

3.3.3 Mechanically induced martensitic transformation (MIMT) kinetics

To quantitatively investigate the suppression effect of the MIMT by applying electric current, the microstructural changes were analyzed as the deformation progressed, focusing on the change in the retained austenite phase fraction. As shown in Fig. 3.5b, for the non-pulsed tension at RT, the fraction of the retained austenite phase decreased as the deformation progressed. However, in the multi-pulsed tension, the retained austenite phase fraction slightly decreased as the deformation proceeded. The fractions of the retained austenite phase at the true strains of 0.076, 0.117, and 0.207 were 23.8, 21.5, and 15.3%, respectively. For the specimen immediately after fracture, the retained austenite phase fraction of 8.5% remained. This means that the retained austenite phase obviously transformed into martensite phase during deformation at RT. The fraction of the retained austenite phase in the multi-pulsed specimen immediately after fracture was 21.5%, which was much higher than that in the non-pulsed tension at RT (8.5%). For the non-pulsed tension at 100 °C, there is no noticeable change in the fraction of the retained austenite phase during the deformation. This indicates that the MIMT effect hardly worked, because the stability of the retained austenite phase increased due to the temperature rise under the conditions of multi-pulsed and non-pulsed tension at 100 °C. Also, the calculated and experimental data were in good agreement for the given conditions. This result shows that the MIMT kinetics of this material can be successfully described by the model.

Based on these results, it can be seen that periodically applying multi pulses of

electric current to the specimens interferes with the MIMT effect and causes the ductility to decrease, as shown in Fig. 3.4a. Therefore, a new design of electric current pulsing pattern should be developed for improving the formability of TRIP-aided steel without requiring additional processing.

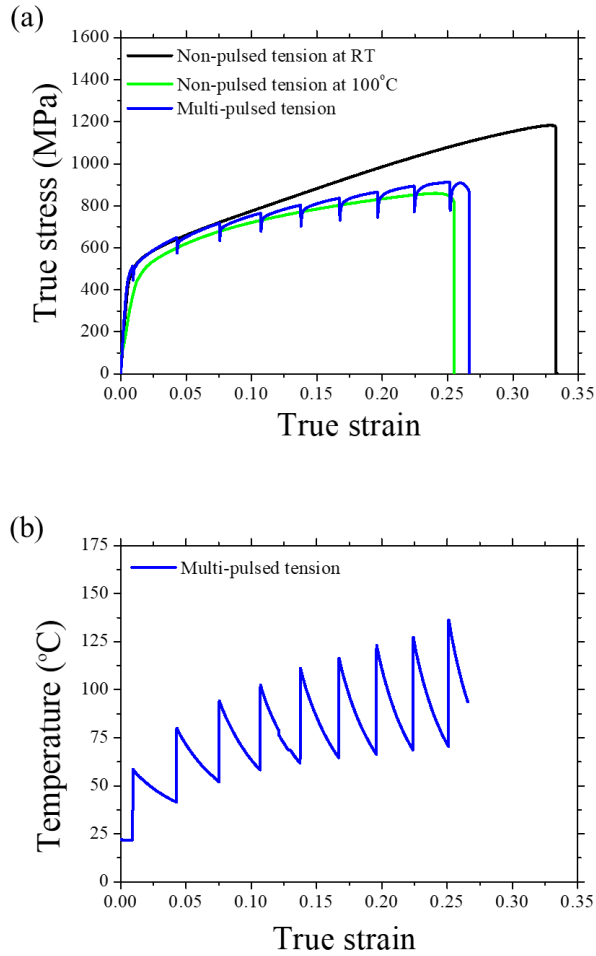


Figure 3.4 (a) True stress-strain curves of non-pulsed tension at RT (in black), non-pulsed tension at 100 °C (in green), and multi-pulsed tension (in blue) under the cross head speed of 1.5 mm/min. (b) The temperature of specimen measured during multi-pulsed tension.

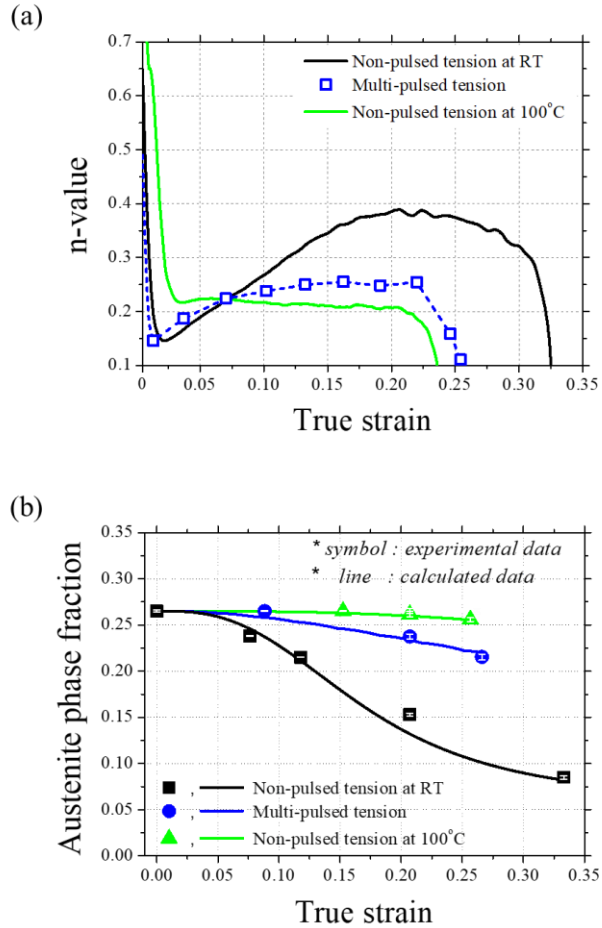


Figure 3.5 (a) The calculated strain hardening exponent and (b) the fraction of retained austenite phase as a function of true strain for non-pulsed tension at RT (in black), non-pulsed tension at 100 °C (in green), and multi-pulsed tension (in blue). The experimental data (symbols) and calculated data (lines) were based on the XRD measurement and MIMT kinetics model, respectively.

3.4 New pulsing pattern: 3 pulsings in the early stage of deformation

For improving the ductility of the TRIP-aided steel, the pulsing pattern of electric current was modified to apply 3 pulses of electric current in the early stage of deformation immediately before the phase transformation of retained austenite phase begins. The point at which to apply electric current was selected to be before an inflection point. Note that the MIMT occurred significantly at the inflection point according to the result in Fig. 3.5b. Thus, based on the inflection point occurring at a true strain of approximately 0.10, the 3 pulses of electric current were applied at the true strains of 0.01, 0.039, and 0.076, respectively. Moreover, in order to maintain the same electrical energy per unit volume, the electric currents were applied to the specimen while maintaining constant current density.

3.4.1 Electric current-induced delay of MIMT

The 3-pulsed specimen showed a significant increase in elongation, as shown in Fig. 3.6a. The elongation increased from 0.33 to 0.40 by applying only 3 pulses of electric current compared to the non-pulsed tension at RT. The flow stress in the 3-pulsed tension was much lower than that in the non-pulsed tension at RT. Fig. 3.6b shows the measured specimen temperature during the 3-pulsed tension. The peak values of the measured temperature at each electric pulse were 170, 215, and 216 °C, respectively. Because the true current density was maintained as constant, the measured specimen temperature should theoretically be the same. However, since the first pulse was applied at RT and the second pulse was then applied at the state in which the specimen had not completely cooled to RT, it is thought that a difference in the measured temperature occurred.

In the 3-pulsed tension, it was also observed that the slope of the true stress-strain curve after applying 3 pulses was noticeably changed in comparison with the non-pulsed tension at RT. To check the effect of 3 pulses on the phase hardening effect, the strain hardening exponent (n) was calculated and is plotted as a function of true strain in Fig. 3.7a. The calculation was performed from the true strain of 0.10 after applying 3 pulses due to a large fluctuation by stress drop. As a result, in the 3-pulsed tension, the curve of strain hardening exponent was significantly different from the non-pulsed tension at RT. The n value decreased to 0.13 until the true strain was 0.13, and then increased to 0.56 until the true strain was 0.26. When the 3 pulses were applied in the early stage of deformation, the maximum value of n appeared in

the latter stage of deformation and increased in comparison with the non-pulsed tension at RT. This means that because the phase transformation from the retained austenite to the martensite phase was delayed by applying electric current, the phase hardening effect was amplified in the latter stage of deformation. This delay effect of phase transformation was caused by the increase in stability of the retained austenite phase during electric current application, as mentioned in the Chapter 3.3.

To clarify the phase transformation delay effect by applying 3 pulses of electric current, the change in retained austenite phase fraction was measured based on the XRD measurement, as shown in Fig. 3.7b. In the 3-pulsed tension, it was observed that the curve of retained austenite phase fraction as a function of true strain was shifted to the right compared to the non-pulsed tension at RT. The fraction values of retained austenite phase for the 3-pulsed tension at the true strains of 0.076, 0.117, and 0.207 were 26.3, 25.8, and 19.8%, respectively. Since the fraction value of the retained austenite phase at the true strain of 0.117 was similar to the initial value (26.5%), it can be seen that the phase transformation hardly occurs up to the true strain of 0.117 under the application of electric current. From the true strain of 0.117, the fraction value of the retained austenite phase decreased in earnest, while the MIMT occurred properly. Moreover, at the true strain of 0.207, the fraction value of retained austenite phase in the 3-pulsed tension was still higher than that in the non-pulsed tension at RT. Thus, it was confirmed that applying the electric current in the early stage of deformation clearly induces the delay effect of MIMT. In addition, for the specimen immediately after fracture in the 3-pulsed tension, the retained

austenite phase fraction was 7.9%, which was similar with that in the non-pulsed tension at RT (8.5%). Moreover, there is no difference in the maximum true stress values at fracture between the non-pulsed tension at RT and 3-pulsed tension, as shown in Fig. 3.6a. This means that there is no negative effect of electric current on the implementation of the original mechanical properties for the investigated TRIP-aided steel.

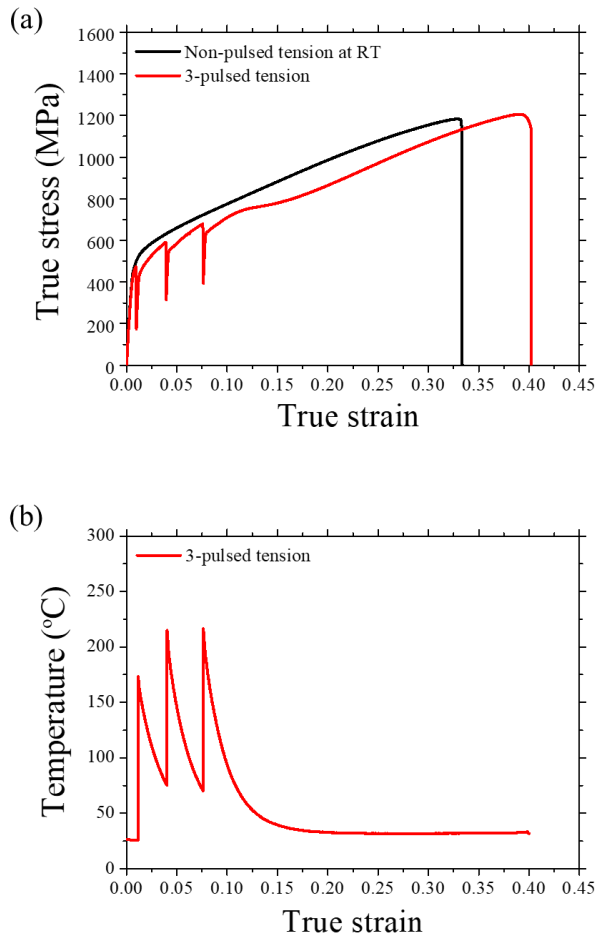


Figure 3.6 (a) True stress-strain curves of non-pulsed tension at RT (in black) and 3-pulsed tension (in red) under the cross head speed of 1.5 mm/min. (b) The temperature of specimen measured during 3-pulsed tensile test.

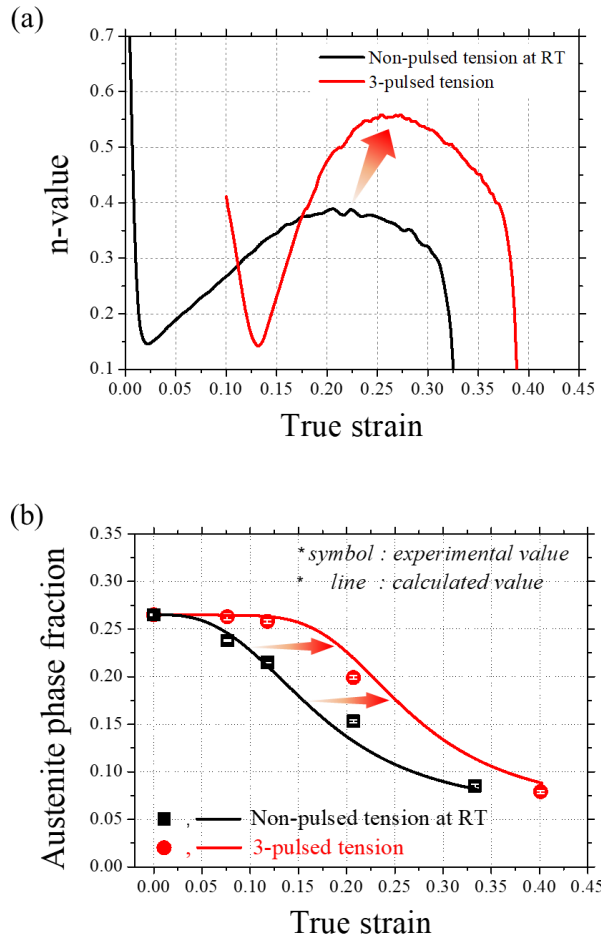


Figure 3.7 The calculated strain hardening exponent and (b) the fraction of retained austenite phase as a function of true strain for the non-pulsed tension at RT (in black) and 3-pulsed tension (in red). The experimental data (symbols) and calculated data (lines) was based on the XRD measurement and MIMT kinetics model, respectively.

3.4.2 Electric current-induced annealing

The FWHM analysis of the diffraction peak profile is a well-established technique for determining the dislocation density in crystalline materials. Generally, diffraction peak profile is broadened when subgrains are small or if the crystal lattice is distorted by lattice defects, especially by dislocations [34–36]. Here, instrumental effects on the diffraction peak broadening were assumed to be the same in all specimens, with a focus on the major effects of dislocations. Additionally, since the fraction of martensite phase and grain size can affect the FWHM value, the specimens containing the same fraction of martensite phase and grain size should be compared.

As shown in Fig. 3.8a, four specimens strained to the true strain of 0.076 in the non-pulsed tensions at RT, 100, 200 °C, and 3-pulsed tension were prepared to obtain the FWHM values of the ferrite peaks. From the XRD analysis results, it was identified that three specimens excluding the non-pulsed specimen at RT have the same fraction of retained austenite phase (26.5%), which means that there is no change in phase fraction until the true strain reached 0.076 under the three given conditions (non-pulsed tensions at 100, 200 °C, and 3-pulsed tension). Additionally, EBSD analysis was conducted for the four specimens to verify whether the grain size of the ferrite phase was same for the four specimens. Figs. 3.8b, c, d, and e show the phase map obtained from the non-pulsed tensions at RT, 100, 200 °C, and 3-pulsed tension, respectively. The ferrite and austenite phase are indicated by green and red, respectively. As a result, the average grain size of the ferrite phase for the four

specimens obtained from the non-pulsed tensions at RT, 100, 200 °C, and 3-pulsed tension were almost the same as 6.44, 6.79, 6.13, and 6.28 μm , respectively (Figs. 3.8b, c, d, and e).

Thus, the annealing effect was then qualitatively discussed by comparing of the FWHM values of the ferrite peaks for the four specimens under the same instrumental conditions, retained austenite phase fraction, and grain size. The FWHM profiles obtained from the non-pulsed tensions at RT, 100, 200 °C, and 3-pulsed tension at the same true strain of 0.076 are presented in the Fig. 3.9, as well as the X-ray diffraction patterns. The FWHM values are presented as a function of 2θ , where θ is the Bragg angle. As a result, for the non-pulsed tension, the values of FWHM decreased with increasing temperature. This was due to recovery effect of dislocation as the temperature increased. However, the values of FWHM obtained from the specimen in the 3-pulsed tension was lower than the non-pulsed tension at 100 °C and similar to the non-pulsed tension at 200 °C. Note that the strained specimen at 200 °C was deformed under stronger temperature condition, with respect to thermal energy, than the temperature condition of specimen due to Joule heating during 3-pulsed tension. This suggests that the specimen was clearly annealed due to the annihilation of dislocations by both thermal and athermal effects while 3 pulses of electric current were applied. Based on this result, it is thought that the electric current-induced annealing would also occur in the multi-pulsed tension. However, when multi pulses of electric current were applied, the suppression of the MIMT effect overwhelmed the electric current-induced annealing effect so that the ductility

was decreased.

Therefore, applying an electric current at the state in which the phase transformation of the retained austenite phase begins to take place can clearly induce both the electric current-induced annealing and an adequate delay of the MIMT effects. This enhances the ductility without deteriorating of mechanical property. Thus, it was confirmed that the formability of TRIP-aided steel can be sufficiently improved by applying an electric current. Furthermore, our results show that the EAM technique can save a lot of energy and time in the forming of TRIP-aided steel.

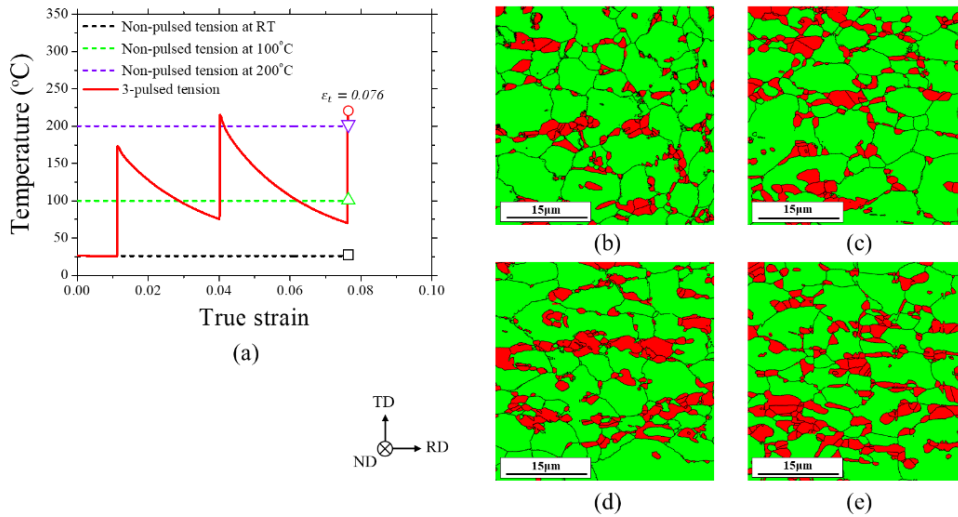


Figure 3.8 (a) Temperature histories during 3-pulsed tension (in red), non-pulsed tension at RT (in black), 100 °C (in green), and 200 °C (in purple) until the true strain of 0.076. EBSD phase maps (red area: retained austenite phase, green area: ferrite matrix) for the four specimens obtained from: (b) the non-pulsed tension at RT, (c) the non-pulsed tension at 100 °C, (d) the non-pulsed tension at 200 °C, and (e) the 3-pulsed tension.

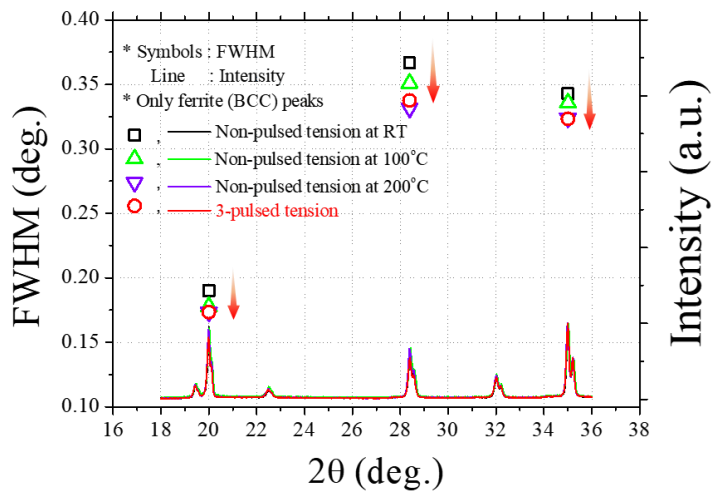


Figure 3.9 FWHM profiles (symbols, left axis) of ferrite phase peaks and X-ray diffraction patterns (lines, right axis) in the range of 18-36° for the four specimens strained to the true strain of 0.076 in the 3-pulsed tension (in red), non-pulsed tension at RT (in black), 100 °C (in green), and 200 °C (in purple).

3.5 Conclusion

In this chapter, the effect of electric current on the MIMT for TRIP-aided steel was investigated based on microstructural analysis and calculations. When a periodic pulsed electric current was applied to the specimen during plastic deformation, the elongation at fracture decreased compared to the non-pulsed tension at RT, although the flow stress substantially decreased. From the XRD measurement and calculation of MIMT kinetics, it was identified that the MIMT effect could not work properly in the multi-pulsed and non-pulsed tension at 100 °C, because the stability of the retained austenite phase increased due to a temperature rise. A new pulsing pattern of electric current was designed to improve the formability of TRIP-aided steel. 3 pulses of electric current were applied in the early stage of deformation immediately before the phase transformation of retained austenite phase begins to take place. As a result, a significant increase in elongation was observed compared to non-pulsed tension at RT. The increase in elongation in the 3-pulsed tension was due to two types of effect. One is the delay effect of the phase transformation, causing the MIMT effect to be exhibited in the latter stage of deformation. The other is an annealing effect during application of electric current, which is identified by comparing the FWHM values obtained from the XRD measurement. Therefore, the EAM technique can efficiently improve the formability by designing the pulsing pattern of electric current in accordance with the material characteristic.

3.6 References

- [1] H. E. Friedrich, P. Steinle, G. Kopp, R. Scholl, *Mater. Sci. Forum*, 3 (2010) 638.
- [2] E. Jimenez-Melero, N. H. van Dijk, L. Zhao, J. Sietsma, J. P. Wright, S. van der Zwaag, *Mater. Sci. Eng. A*, 528 (2011) 6407.
- [3] P. Jacques, J. Ladriere, F. Delannay, *Metall. Mater. Trans. A*, 32 (2011) 2759.
- [4] G. K. Tirumalasetty, M. A. van Huis, C. Kwakernaak, J. Sietsma, W. G. Sloof, H. W. Zandbergen, *Acta mater.*, 60 (2012) 1311.
- [5] E. Girault, A. Martens, P. Jacques, Y. Houbaert, B. Verlinden, J. van Humbeeck, *Scr. Mater.*, 44 (2001) 885.
- [6] P. Jacques, Q. Furnemont, A. Mertens, F. Delannay, *Philos. Mag. A*, 81 (2001) 1789.
- [7] H. N. Han, J. K. Lee, *ISIJ Int.*, 42 (2002) 200.
- [8] H. N. Han, D.-W. Suh, *Acta Mater.*, 51 (2003) 4907.
- [9] V. F. Zackay, E. R. Parker, D. Fahr, R. Bush, *Trans. ASM*, 60 (1967) 252.
- [10] H. N. Han, C.-S. Oh, G. Kim, O. Kwon, *Mater. Sci. Eng. A*, 499 (2009) 462.
- [11] G. B. Olson, M. Cohen, *Metall. Mater. Trans. A*, 13 (1982) 1907.
- [12] H. N. Han, C. G. Lee, D.-W. Suh, S.-J. Kim, *Mater. Sci. Eng. A*, 485 (2008) 224.
- [13] G.-M. Carlos, G. C. Francisca, *Mater. Trans.*, 46 (2005) 1839.
- [14] R. Schubert, *Society of Manufacture Engineers Technical papers*, (2003) 1.
- [15] G. Tang, J. Zhang, Y. Yan, H. Zhou, W. Fang, *J. Mater. Process. Technol.*, 137

(2003) 96.

- [16] M.-S. Kim, N. T. Vinh, H.-H. Yu, S.-T. Hong, H.-W. Lee, M.-J. Kim, H. N. Han, J. T. Roth, *Int. J. Precis. Eng. Manuf.*, 15 (2014) 1207.
- [17] W. J. Lu, R. S. Qin, *Mater. Sci. Eng. A*, 677 (2016) 252.
- [18] H.-D. Nguyen-Tran, H.-S. Oh, S.-T. Hong, H. N. Han, J. Cao, S.-H. Ahn, D.-M. Chun, *Int. J. Precis. Eng. Manuf.*, 2 (2015) 365.
- [19] N. T. Thien, Y.-H. Jeong, S.-T. Hong, M.-J. Kim, H. N. Han, M.-G. Lee, *Int. J. Precis. Eng. Manuf.*, 3 (2016) 325.
- [20] X. Liu, S. Lan, J. Ni, *Mater. Sci. Eng. A*, 582 (2013) 211.
- [21] H. N. Han, C. G. Lee, C.-S. Oh, T.-H. Lee, S.-J. Kim, *Acta Mater.*, 52 (2004) 5203.
- [22] Q. Furnemont, M. Kempf, P. Jacques, M. Goken, F. Delannay, *Mater. Sci. Eng. A*, 328 (2002) 26.
- [23] K. Jacchin, B. Beyer, *Z Metallkd*, 91 (2000) 106.
- [24] B. Sundman, B. Jansson, J. O. Andersson, *CALPHAD*, 9 (1985) 153.
- [25] M.-J. Kim, K. Lee, K. H. Oh, I. S. Choi, H. H. Yu, S.-T. Hong, H. N. Han, *Scr. Mater.*, 75 (2014) 58.
- [26] M.-J. Kim, M.-G. Lee, K. Hariharan, S.-T. Hong, I.-S. Choi, D. Y. Kim, K. H. Oh, H. N. Han, *Int. J. Plast.*, 94 (2017) 148.
- [27] H.-J. Jeong, M.-J. Kim, J.-W. Park, C. D. Yim, J. J. Kim, O. D. Kwon, P. P. Madakashira, H. N. Han, *Mater. Sci. Eng. A*, 684 (2017) 668.
- [28] J.-W. Park, H.-J. Jeong, S.-W. Jin, M.-J. Kim, K. Lee, J. J. Kim, S.-T. Hong,

- H. N. Han, *Mater. Charact.*, 133 (2017) 70.
- [29] G. B. Olson, M. Cohen, *Metall. Trans.*, 6A (1975) 791.
- [30] F. Lecroisey, A. Pineau, *Metall. Trans.*, 3 (1972) 387.
- [31] S. J. Jones, K. H. D. H. Bhadeshia, *Acta Metall. Mater.*, 45 (1997) 2911.
- [32] S.-J. Lee, S. Lee, B. C. De Cooman, *Scr. Mater.*, 64 (2011) 649.
- [33] J. Mahieu, J. Maki, B. C. De cooman, S. Claessens, *Metall. Mater. Trans. A*, 33 (2002) 2573.
- [34] G. K. Williamson, W. H. Hall, *Acta Metall.*, 1 (1953) 22.
- [35] T. Ungar, A. Borbely, *Appl. Phys. Letts.*, 69 (1996) 3173.
- [36] T. Ungar, I. Dragomir, A. Revesz, A. Borbely, *J. Appl. Cryst.*, 32 (1999) 992.

Chapter 4

Microstructure resetting method using sub-second electric pulsing

4.1 Introduction

Metallic materials are the most widely used in all engineered structures. They inevitably accumulate microscale damages such as second phase, dislocation, and microvoids during their use. These damage the originally designed microstructure, degrading the mechanical properties/life expectancy of the engineered structures, and even leads to failure. Therefore, various methods for repairing damage in materials have been proposed based on concept of self-healing [1–8]. In the early stage, polymer materials were intensively studied since they have the intrinsic ability to achieve autonomous healing of damage [1–4]. However, the application of self-healing to metallic materials is intrinsically difficult due to their low atomic mobility or diffusivity, their high melting point, and difficulty in detecting damage [5–8].

To apply the self-healing concept to metallic materials, researchers have adopted two methods: applying external stimuli such as heat or magnetic field/pressure to repair the damaged microstructure [5–8], or simply designing new materials with better material/mechanical properties to substitute the original materials [9, 10]. However, it is unpractical to develop new materials every time a

damage occurs. Naturally, the concept of applying external stimuli to repair the damaged microstructure is preferred for metallic materials. This is called non-autonomous self-healing. Here, a sub-second electric pulsing is utilized as a non-autonomous self-healing method to infinitely reset the damaged microstructure of metallic materials to its initial microstructure.

The electric pulsing can provide three benefits: rapid heating up to a target temperature in only 0.01–1.0 s; various applications; kinetic enhancement of microstructural change such as dislocation annihilation, aging, dissolution, and recrystallization [11–18]. Based on the positive effects of electric pulsing, we design a strategy of microstructure resetting for infinite reuse of metallic materials.

The schematic diagram of the microstructure resetting strategy considering the damage characteristics is showed in Fig. 4.1. After deformation until the critical point, the specimen is unloaded. The electric pulsing is then applied to the specimen. This process is performed repeatedly (Fig. 4.1a). One key point is to find the critical point of damage where the electric pulsing should be applied to the damaged material to reset its microstructure to the initial state. If the electric pulsing is applied to the material when the deformation is too small, the number of pulsing required to reach the same strain becomes too high, resulting in low process efficiency. On the other hand, if the electric pulsing is applied when the material is excessively deformed, it is hard for the damaged microstructure to recover completely. The other key point is the selection of materials having resetting core which is crucial role in microstructure resetting. First, for the definition of resetting core, it is essential to consider the

intrinsic damage characteristics which induce material failure. Damages such as transformed phase [8, 19], microvoid [6, 20], and dislocation [21] generated at the microscale during deformation have a reversible feature. This means that they can be reset to the initial state through applying external heat. Thus, we define the resetting core based on the phenomena that can make the initial state while eliminating these damage characteristics. Here, the resetting core is classified into three categories: phase transformation, dislocation recovery, and recrystallization (Fig. 4.1b).

In addition, it is important to obtain the optimum pulsing condition with the target temperature, electric current density, and current duration. Increasing the electric current density while reducing the duration to reach the same temperature condition is generally more effective to cause strong athermal effect than lower electric current density with long duration time. Also, it can improve the efficiency of process. However, it is impossible to unconditionally increase the electric current density due to the limited output of the power supply and rapid thermal expansion of the material. Therefore, the optimum pulsing condition to induce proper thermal and athermal effects should be found.

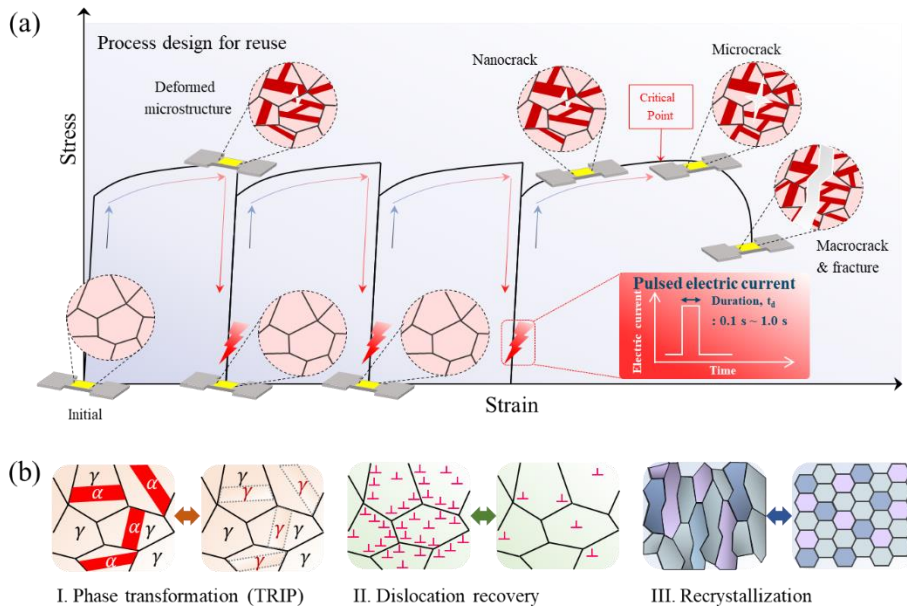


Figure 4.1 (a) Scheme for the process design showing the mechanical behavior of tensile deformation after each pulsing treatment and change in damage for the specimen and (b) Resetting cores (phase transformation, dislocation recovery, and recrystallization) reflecting reversible damage characteristics at microscale.

4.2 Experimental procedure

4.2.1 Specimen preparation and experimental set-up

Three materials having resetting cores, commercial 301L/316L stainless steels (SUS301L/SUS316L) and super-elastic NiTi alloy were selected. The chemical compositions of the SUS301L and SUS316L are 0.03C–0.74Si–17.93Cr–0.59Mn–6.41Ni–Bal. Fe and 0.08C–0.53Si–16.80Cr–1.08Mn–10.10Ni–Bal. Fe by wt.%, respectively. Tensile specimens of the SUS301L and SUS316L with a gauge width of 9 mm, thickness of 1 mm, and gauge length of 12 mm were fabricated along the rolling direction (RD) of the sheet (Fig. 4.2a). The uniaxial tensile tests were conducted using a tensile test machine (INSTRON 5584, USA) at a constant crosshead speed of 1.5 mm/min at room temperature (RT, 25 °C). For the super-elastic NiTi alloy, the chemical composition is 55.8Ni-0.05Fe-0.05C-0.025N-0.025O-Bal.Ti by wt.%. The specimen of this material was fabricated along the transverse direction (TD) of the sheet by halving the specimen dimension of the SUS301L and SUS316L. The cyclic deformation was performed using a tensile test machine (INSTRON 5582, USA) at a constant crosshead speed of 1.0 mm/min at RT. The specimen displacement was measured using the ARAMIS Digital Image Correlation (DIC) system (GOM, Germany), which enabled non-contact measurement based on the principle of digital image correlation.

To apply electric pulsing, a custom-made fixture was designed to allow the electric current to flow in the specimen. Specifically, we made it possible to relieve

the stress by making the specimen move in both directions to solve the problem of bending caused by the rapid thermal expansion when the electric pulsing was applied to the specimen (Fig. 4.2b). The electric pulsing was generated by a Vadal SP-1000U welder (Hyosung, South Korea) and a Keysite 6680A power supply (Maros, USA). We measured the temperature change of the specimen during pulsing using an FLIR-E40 infra-red (IR) thermal imaging camera (FLIR, Sweden). One side of the specimen was sprayed with a black thermal paint to stabilize the emissivity and thus improve the accuracy of temperature measurement. The emissivity was calibrated by comparing the measured temperature using a K-type thermocouple. The temperature was measured at the center of the specimen, which was the portion at maximum temperature when the electric pulsing was applied to the specimen.

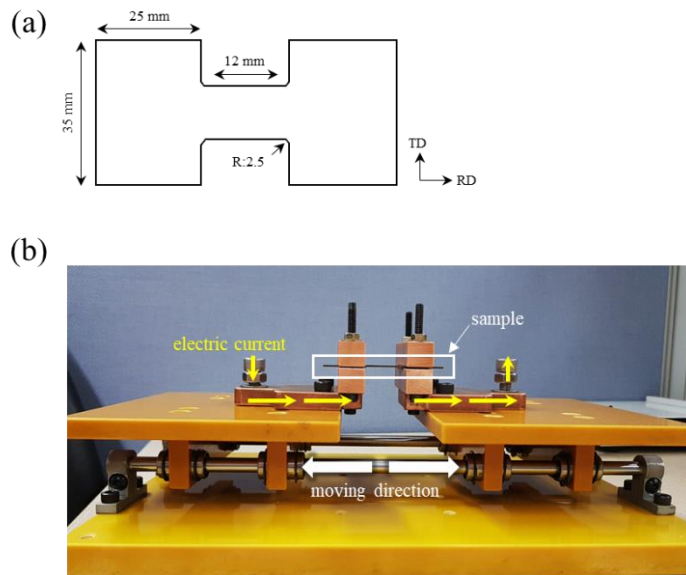


Figure 4.2 (a) Geometry of tensile specimen for the SUS301L and SUS316L. The gage length is 12 mm. For the super-elastic NiTi alloy, the tensile specimen was fabricated by halving the SUS301L/SUS316L specimen size. (b) Actual image of custom-made fixture for stress relief.

4.2.2 Strategy of microstructure resetting method

For the martensitic reverse transformation and recrystallization of the SUS301L, the target temperature was set to 1000 °C. The temperature was chosen accordingly to the phase diagram, showing full transformation to the austenite phase at 1000 °C. For the SUS316L, the target temperature was set to 1050 °C as the proper condition to match the grain size to that of the initial state after electric pulsing treatment, through the recrystallization and grain growth. For the super-elastic NiTi alloy, the target temperature was set to 900 °C considering the martensitic reverse transformation and dislocation recovery. Note that these target temperatures were optimally obtained from extensive studies on various parameters.

Based on the determined target temperature, the electric current density and the current duration were varied to obtain optimal condition. From the equipment specifications, the optimal electric current density at which the electric current could be safely applied to the SUS301L and SUS316L was 90 A/mm². The optimal electric current durations were 0.55 and 0.65 s for SUS301L and SUS316L, respectively. For the super-elastic NiTi alloy, the optimal electric current density and duration were 100 A/mm² and 0.30 s, respectively.

Based on the above results, the concept of microstructure resetting was applied to three materials. For SUS301L and SUS316L, tensile deformation after pulsing treatment is conducted up to the specified critical point of damage (Fig. 4.3a). Here, although the specimen can be further deformed, this process was repeated only 11 and 3 times for SUS301L and SUS316L, respectively. For the super-elastic NiTi

alloy, only 3 times of cyclic deformation and pulsing treatment were repeatedly performed (Fig. 4.3b). For all pulsing treatments, a different amplitude of electric current was applied to the specimen considering the decrease in the cross-sectional area of the specimen. This was done in order to maintain a constant electric current density based on the actual cross-sectional area of the specimen when electric pulsing (each step) was applied. The detailed conditions including the cross-sectional area and electric current at each pulsing for SUS301L, SUS316L, and super-elastic NiTi alloy are listed in Tables 4.1a, b and c, respectively.

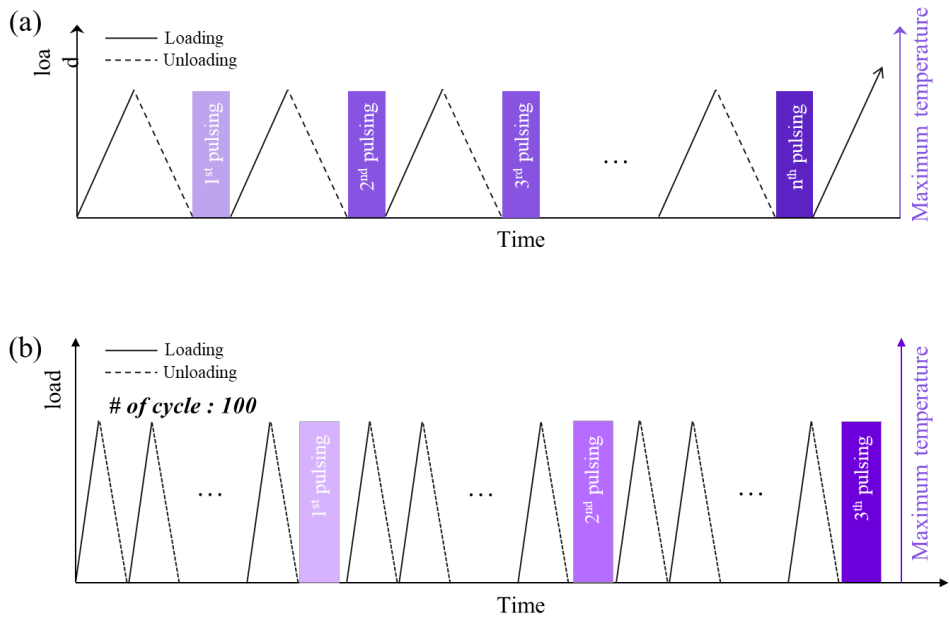


Figure 4.3 Schematics of experimental procedure of pulsing treatment and loading/unloading in the microstructure resetting method for (a) SUS301L/SUS316L and (b) super-elastic NiTi alloy.

Table 4.1 Parameters of electric pulsing condition for (a) SUS301L, (b) SUS316L, and (c) super-elastic NiTi alloy.

(a)

Alloy	# of pulsing	Cross section area (mm ²)	Current amplitude (A)	Current density (A/mm ²)	Duration (s)	Target temperature (°C)
SUS301L	1	5.3	480	90	0.55	1000
	2	4.8	440			
	3	3.6	330			
	4	2.5	230			
	5	1.7	160			
	6	1.1	100			
	7	0.6	60			
	8	0.4	40			
	9	0.2	20			
	10	0.1	10			
	11	0.05	5			

(b)

Alloy	# of pulsing	Cross section area (mm ²)	Current amplitude (A)	Current density (A/mm ²)	Duration (s)	Target temperature (°C)
SUS316L	1	6.6	600	90	0.65	1050
	2	5.0	450			
	3	3.8	340			

(c)

Alloy	# of pulsing	Cross section area (mm ²)	Current amplitude (A)	Current density (A/mm ²)	Duration (s)	Target temperature (°C)
Super-elastic NiTi alloy	1	6.9	690	100	0.30	900
	2					
	3					

4.2.3 Microstructure observation

The microstructure of the specimen was characterized using a field emission-scanning electron microscopy (FE-SEM) with an electron backscatter diffraction (EBSD) system (FE-SEM: SU70, Hitachi, Japan; EBSD: Hikari EBSD detector with TSL OIM 6.1 software, EDAX/TSL, USA). The critical misorientation angle was set to 15° for grain identification. ND, RD, and TD indicate the normal, rolling, and transverse direction, respectively. The average grain size, phase fraction, recrystallization fraction, and amount of dislocation were obtained from the inverse pole figure (IPF), phase, grain orientation spread (GOS), image quality (IQ), and kernel average misorientation (KAM) maps, respectively. Here, the recrystallized grain was defined within 2° of GOS.

For the SUS301L and SUS316L, the XRD measurement was carried out with a Cu radiation source operating at 40 kV at RT using a Lab X-ray diffractometer (XRD, D8-advance, Bruker Miller Co., Germany). The diffraction patterns were recorded in the scan range of 40–95° with a scan speed of 1 °/min. For the super-elastic NiTi alloy, the XRD measurement was carried out with a Cu radiation source operating at 9 kV at RT using a Lab X-ray diffractometer (XRD, SmartLab, Rigaku, Japan). The diffraction patterns were recorded in the scan range of 30–100° with a scan speed of 0.7 °/min. All phase identifications were performed by matching the peak positions and relative intensities with powder diffraction file (PDF-2) reference data. To check the change in dislocation density, the full width at half maximum (FWHM) value was obtained from the XRD peak data. The diffraction peaks were fitted with the

Pseudo-Voigt function. To measure the fraction of the retained austenite phase, a Rietveld refinement was performed on all specimens using the TOPAS (version 4.2) software package and PDXL software.

All specimens for microstructural analysis were prepared by a standard metallographic grinding technique. After grinding and polishing, they were electropolished with an electrolyte consisting of 80 ml perchloric acid, 100 ml butanol, 90 ml distilled water, and 730 ml ethanol solution at a temperature of approximately 15 °C and a voltage of 20 V for 35 s.

4.3 Case 1: 301L Stainless steel (SUS301L)

SUS301L, which is one of the transformation-induced plasticity (TRIP) steels, consists of a metastable austenite phase. Generally, the metastable austenite phase (face centered cubic, f.c.c. structure) transforms into a hard martensite phase (body centered cubic, b.c.c. structure) when the sum of mechanical energy due to the externally applied stress and the chemical driving force exceeds a critical value [22–24]. The transformation is classified into two types. The first type is stress-assisted martensitic transformation, which occurs at temperatures above the M_s temperature. It is induced via stress-assisted nucleation on the same nucleation sites responsible for the athermal martensitic transformation during cooling [22]. The second type is strain-induced martensitic transformation which occurs in the temperature range above M_s^σ (M_s temperature under an external stress equal to the yield stress of material) and below M_d . This martensitic transformation is dominated by strain-induced nucleation on new nucleation sites created by the plastic strain [23, 24]. These two transformations via the stress-assisted and strain-induced nucleation are hereafter denoted as mechanically induced martensitic transformation (MIMT).

In normal uniaxial tension of SUS301L, the specimen shows strain hardening after yielding at ~330 MPa and failure by fracture at the true strain of 0.62 (Fig. 4.4a). The fraction of the martensite phase increases as the deformation progresses due to the MIMT (Fig. 4.4b). If the martensite phase is heated up to austenite finish temperature, the martensite phase transforms back into the austenite phase, in which phase it remains after cooling to RT [25, 26]. This phenomenon is called martensitic

reverse transformation, which is utilized as one of resetting cores for the SUS301L.

Regarding the critical point of damage for the SUS301L, it is difficult to identify exact point where microcracks or microvoids begin to generate. Thus, we focused on the fraction of transformed phase and necking point where the work hardening rate meets the true stress-strain curve. Then, the amount of pre-strain was determined by dividing the section based on the necking point. After a single pulsing treatment to specimen pre-strained up to 27%, 52%, and 72%, we analyzed the change in the mechanical properties and microstructure for each specimen (Fig. 4.5). For all conditions, no apparent change in the mechanical behavior during reloading after the single pulsing treatment was observed compared to that at the baseline (Fig. 4.5b). All martensite phases transformed into the austenite phases through reverse transformation (Fig. 4.5e). The grains of the austenite phase have equiaxed shape and do not have an orientation gradient in each grain, as seen from the inverse pole figure (IPF) maps for normal direction (ND) (Fig. 4.5d). Thus, we identify that both the reverse transformation of the martensite phase and the recrystallization of the deformed austenite phase occur under the given conditions due to the attained temperature (1000 °C), which is higher than the general range of recrystallization (700–1000 °C) [27, 28]. The properties and microstructure of the initial specimen were kept nearly the same up to the pulsing at the pre-strain of 52%. However, for the pulsing treatment at the pre-strain of 72%, the fraction of recrystallized area and the average grain size were much smaller than those of the initial state (Figs. 4.5c and f). Thus, we set the critical point of damage for SUS301L as the engineering

strain of 52% (true strain of 0.42).

Based on the critical point of damage, we performed only 11 tensile deformations and pulsing treatments, although the specimen can be further deformed. The temperature changes of the specimen measured during pulsing treatment was represented in Fig. 4.6. In each pulsing treatment, the specimen temperature increased instantly due to Joule heating. After applying electric pulsing, the specimen temperature decreased by air cooling. The peak values of the measured temperature during each pulsing treatment were very close to the target temperature. This is because the amplitude of the electric current was changed according to the decrease in cross sectional area of the specimen by deformation in order to keep the electric current density constant.

As a result, a significant elongation improvement of 700% was obtained compared to the baseline (Fig. 4.7a). A photograph of the actual specimen after fracture with the initial specimen is also presented in Fig. 4.7b. Note that the mechanical behavior including engineering yield strength and average grain size after each pulsing are almost identical to that of the initial specimen (Fig. 4.8a). Moreover, no change in texture was observed after each pulsing from the IPF maps (Fig. 4.8b). The XRD data (Fig. 4.9a) and EBSD phase maps (Fig. 4.9b) show a change in the fraction of martensite and austenite phases after each pulsing. For example, the phase fraction of martensite is 53.2% and 51.5% before the 2nd and 8th pulsing, respectively. However, after pulsing, the phase fraction of martensite approaches 0% (Fig. 4.9b), which is also confirmed by the disappearance of the

martensite peaks in Fig. 4.9a. Thus, we identify that the mechanically induced martensite phase completely transforms into austenite phase through the reverse transformation by applying electric pulsing for 0.55 s.

In general, when the heating rate is higher than 100 °C/s, shear-type of martensitic reverse transformation occurs [26]. The shear-type reversed austenite normally exhibits lath-type and banded grains with high dislocation density which are inherited from the martensite phase [26]. However, the grains of the austenite phase observed in this study have equiaxed shape and do not have an orientation gradient in each grain from the IPF maps (Fig. 4.8b). Therefore, we identify that both the reverse transformation of the martensite phase and the recrystallization of the deformed austenite phase occur under the given conditions due to the attained temperature (1000 °C). It can be said that the microstructure resetting assisted infinite deformation in the SUS301L is successfully realized through the two resetting cores: the martensitic reverse transformation of mechanically induced martensite and the recrystallization of deformed austenite.

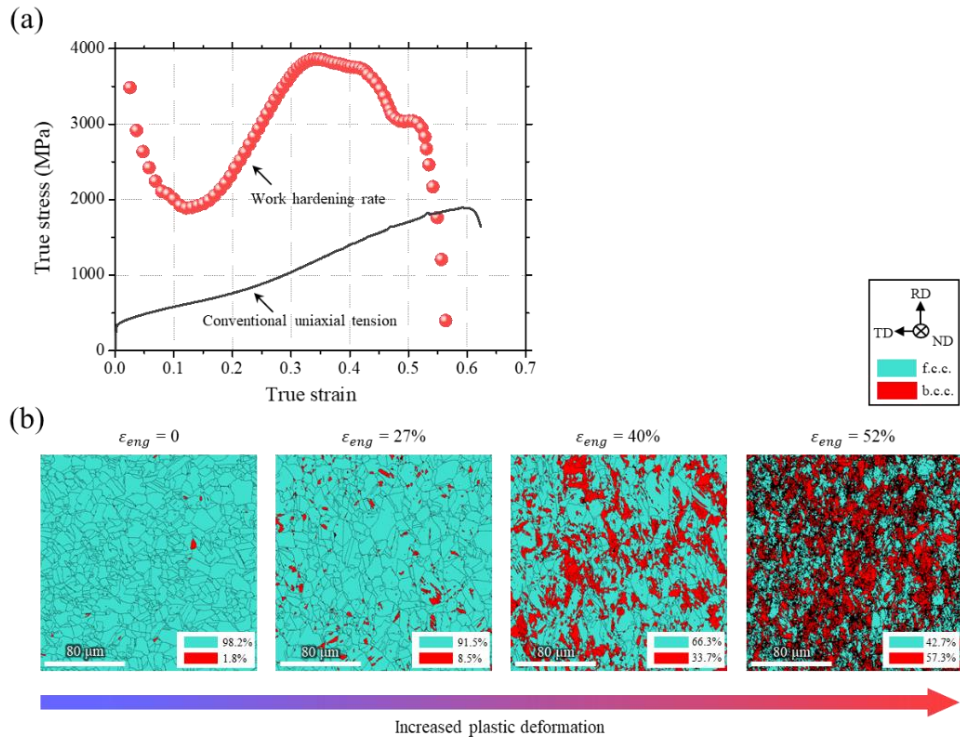


Figure 4.4 (a) Tensile curve (line) and work-hardening rate (symbol). The work hardening rate of SUS301L is obtained from the slope of the true stress–strain curve, which is related to the volume fraction of the mechanically induced martensite phase. (b) EBSD phase maps showing the MIMT as the plastic deformation increases.

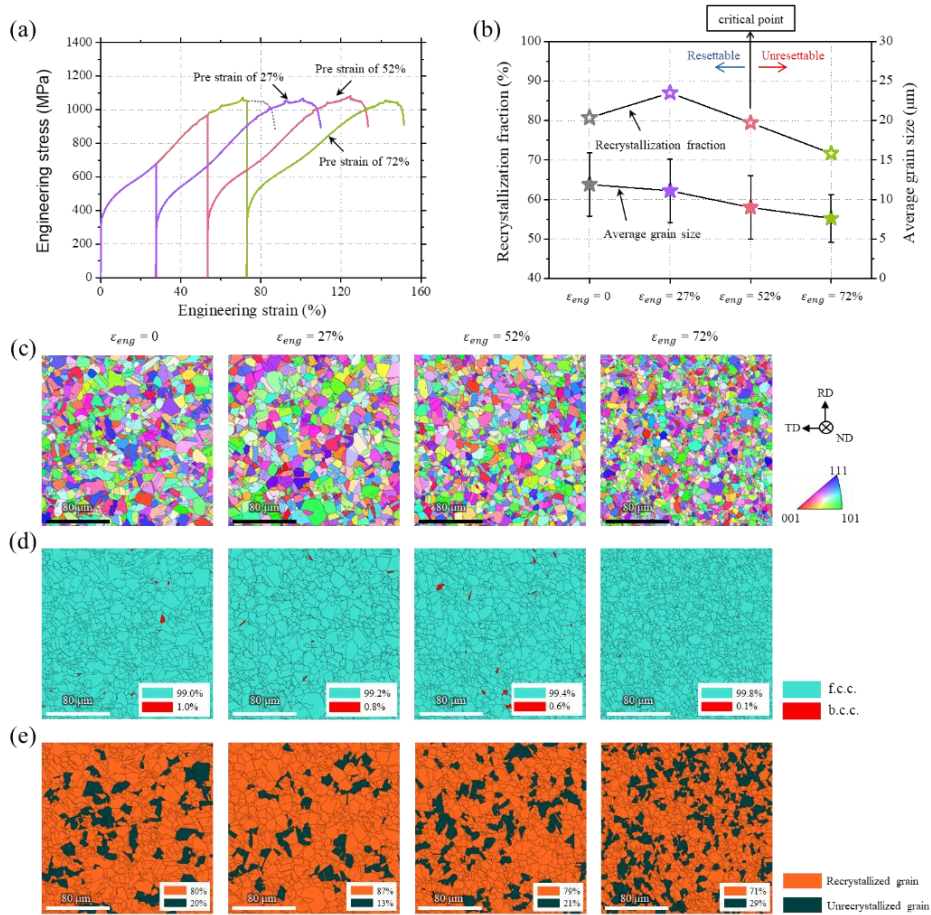


Figure 4.5 (a) Tensile curve data during reloading after single pulsing treatment at the pre-strain of 27%, 52% and 72%. (b) Recrystallization fraction (left axis) and average grain size (right axis) after each pulsing. (c), (d), and (e) EBSD inverse pole figure (IPF), phase, and grain orientation spread (GOS) maps for specimen after single pulsing treatment at the pre-strain of 27%, 52%, and 72% with initial specimen. The orange and dark green areas in the GOS map indicate the recrystallized and unrecrystallized grain, respectively.

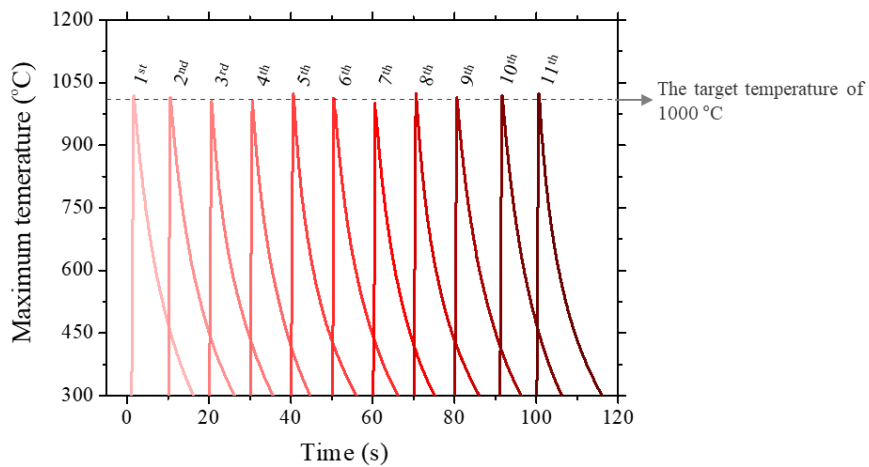


Figure 4.6 Maximum temperatures of specimen measured during pulsing treatment for SUS301L. The time between the previous pulsing and the next pulsing is independent of the actual time of the experiment. To aid in understanding, the temperature histories of each pulsing are arranged in order at a certain interval.

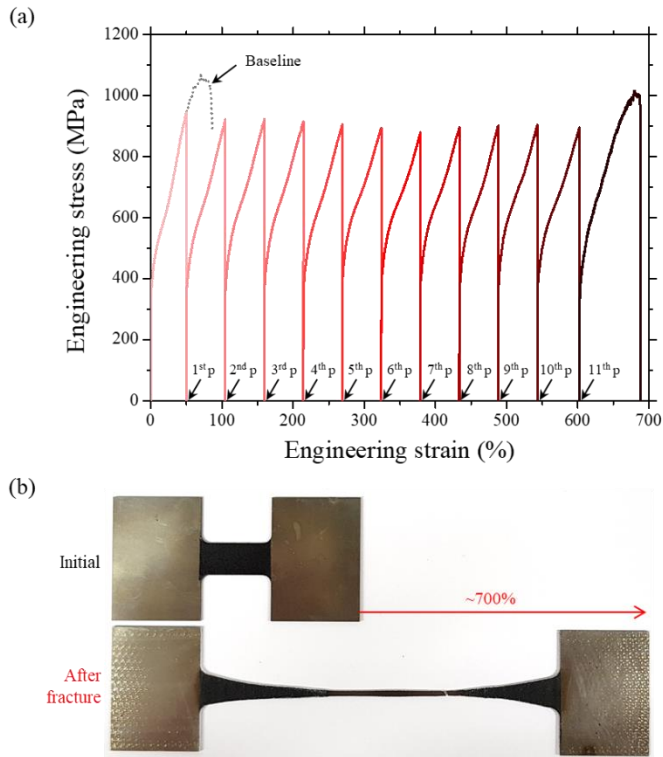


Figure 4.7 (a) Tensile behavior after each pulsing treatment based on the critical point (engineering strain of 52%) is described in red line. The order of pulsing is indicated with arrows. (b) Photograph of specimen after fracture through the microstructure resetting process. To compare the ductility, photograph of initial specimen is also shown.

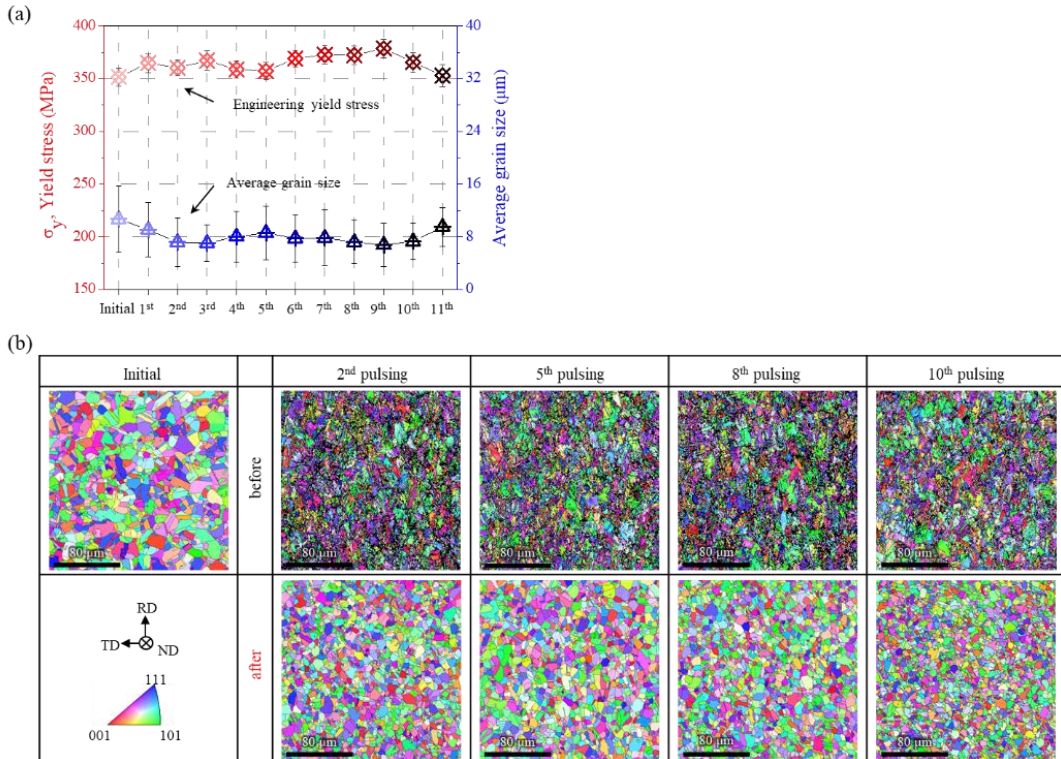


Figure 4.8 (a) Engineering yield strength and average grain size after each pulsing treatment. Error bars represent standard deviation from the average value. (b) EBSD inverse pole figure (IPF) maps for normal direction (ND) before and after 2nd, 5th, 8th, and 10th pulsing compared to the initial specimen. The different colors in the IPF map indicate the orientation of each grain with respect to ND.

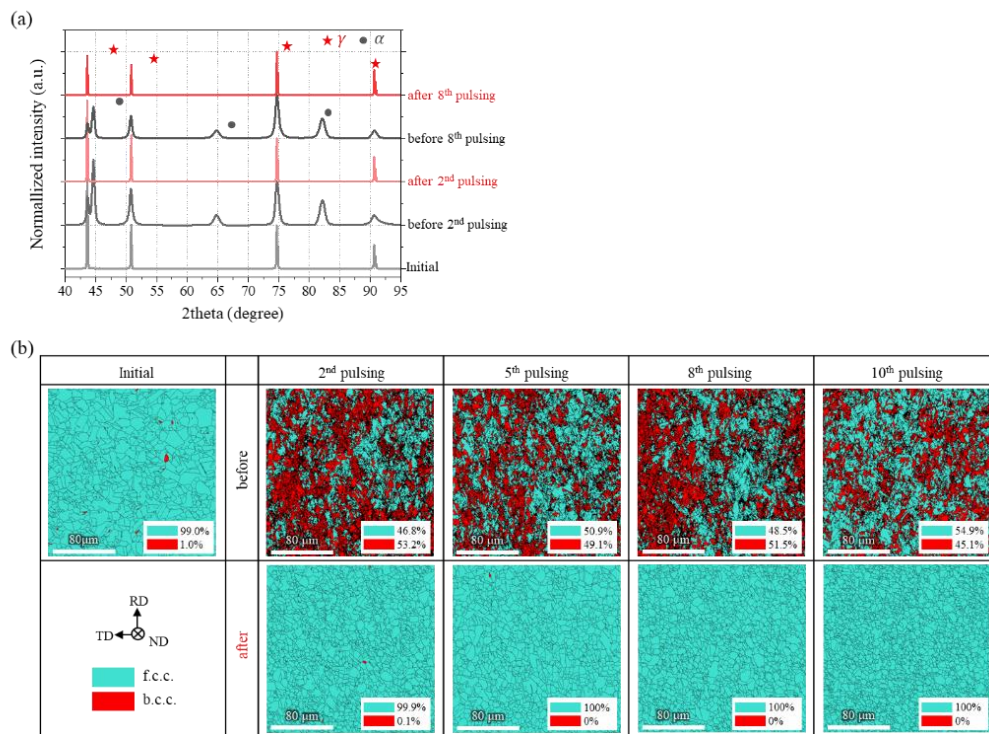


Figure 4.9 (a) X-ray diffraction (XRD) patterns before and after 2nd and 8th pulsing. For the comparison, the XRD pattern for the initial specimen is shown. Theta is the Bragg angle. The symbols of face-centered cubic (f.c.c.) and body-centered cubic (b.c.c.) are presented as star and circle, respectively. (b) EBSD phase maps before and after 2nd, 5th, 8th, and 10th pulsing compared to the initial specimen. The blue and red area in phase map indicate the f.c.c. and b.c.c. phase, respectively. The fraction of f.c.c. and b.c.c. phase is shown within the phase map.

4.4 Case 2: 316L Stainless steel (SUS316L)

SUS316L is well known to have higher stability of the austenite phase than the SUS301L, resulting in plastic deformation via dislocation evolution or twinning [29]. In normal uniaxial tension, the yield strength is ~330 MPa and the true strain at fracture is 0.55 (Fig. 4.10a). As the plastic deformation progresses, the martensite phase was not formed, which implies that the deformation mechanism is not the MIMT (Fig. 4.10b). Thus, the recrystallization was applied as the resetting core of SUS316L.

The critical point of SUS316L was the engineering strain of 40% (true strain of 0.34) which is obtained in the same way with the SUS301L. Although we can perform much more repetitive process, here only 3 tensile deformations and pulsing treatments based on the critical point were applied. The measured temperature during pulsing treatment was represented in Fig. 4.11. As a result, it exhibits the elongation improvement of ~200% after only 3 repetitions (Fig. 4.12). There is no significant difference in microstructure such as the average grain size and fraction of recrystallized area after each pulsing (Figs. 4.13a and b). Also, no change in texture was observed after recrystallization from the IPF maps for normal direction (ND), rolling direction (RD), and transverse direction (TD) (Fig. 4.14).

We focus on the dislocation annihilation after each pulsing. The change in the full width at half maximum (FWHM) values of austenite phase peaks obtained from the XRD data was compared before and after each pulsing (Fig. 4.15). This is a well-established technique for determining the dislocation density in crystalline materials

for which the specimens contain the same phase fraction and grain size [30, 31]. Before each pulsing, the FWHM values are much higher than those in the initial specimen due to the dislocation evolution by plastic deformation. However, after each pulsing, the FWHM values decreased to those in the initial specimen (Fig. 4.15b). This result is well matched with the kernel average misorientation (KAM) results obtained from the EBSD data, which shows that higher degree of misorientation is proportional to the amount of dislocation or the accumulated strain energy in the specimen (Fig. 4.16). This result clearly indicates that the dislocation formed by deformation is annihilated by applying electric pulsing for 0.65 s. Thus, we confirm that the damaged microstructure of SUS316L can be successfully reset through the resetting core of recrystallization.

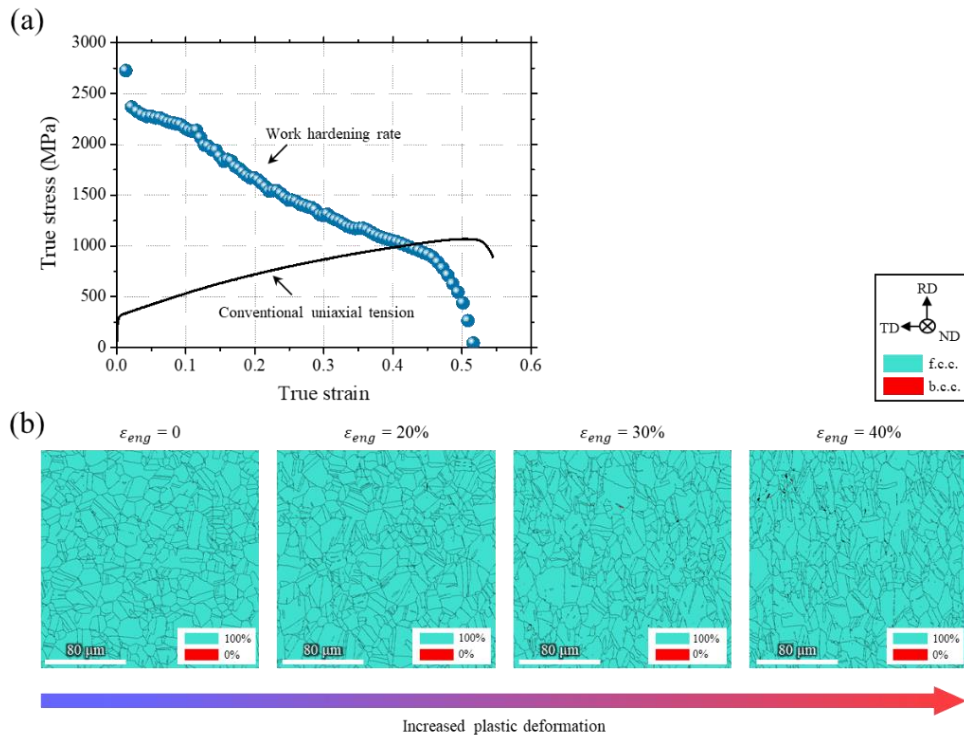


Figure 4.10 (a) Tensile curve (line) and work-hardening rate (symbol). The work hardening rate of SUS316L decreases continuously as the true strain increases. (b) EBSD phase maps showing no change in the phase fraction as the plastic deformation increases.

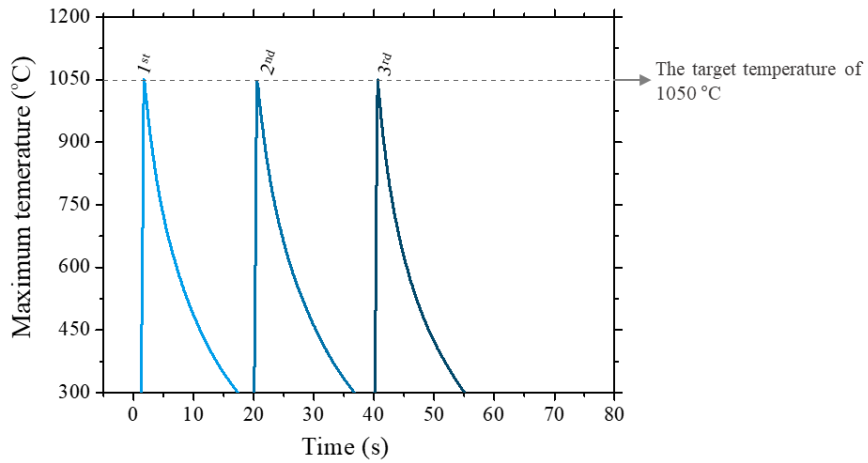


Figure 4.11 Maximum temperatures of specimen measured during pulsing treatment for SUS316L. The time between the previous pulsing and the next pulsing is independent of the actual time of the experiment. To aid in understanding, the temperature histories of each pulsing are arranged in order at a certain interval.

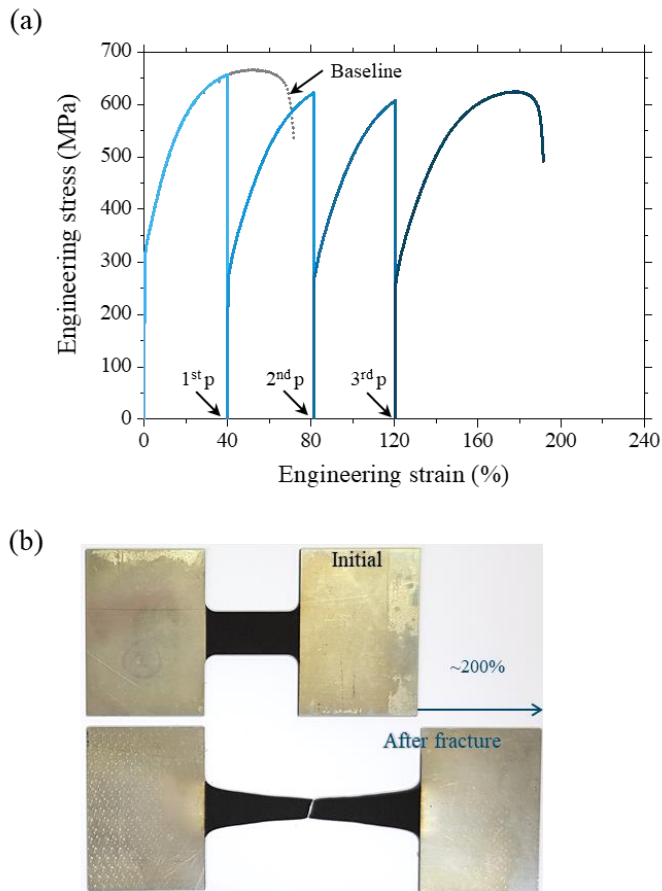


Figure 4.12 (a) Tensile behavior after each pulsing treatment based on the critical point (engineering strain of 40%). The order of pulsing is indicated with arrows. (b) Photograph of specimen after fracture compared to the initial specimen.

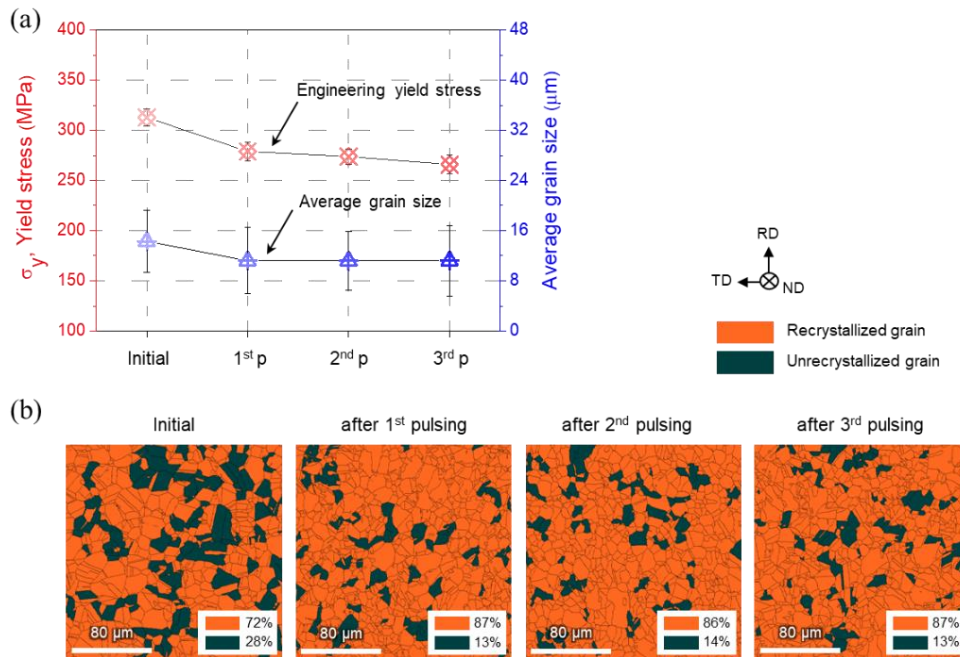


Figure 4.13 (a) Engineering yield strength and average grain size after each pulsing treatment. Error bars represent standard deviation from the average value (b) EBSD grain orientation spread (GOS) maps after 1st, 2nd, and 3rd pulsing with initial specimen. The orange and dark green area in the GOS map indicate the recrystallized and unrecrystallized grain, respectively.

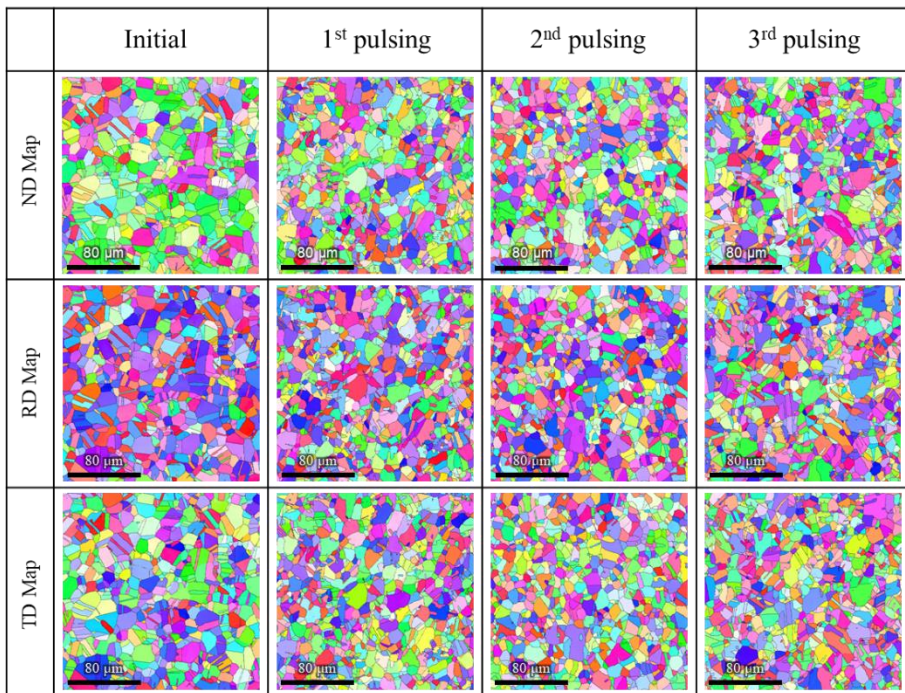


Figure 4.14 EBSD IPF maps for ND, RD and TD after 1st, 2nd, and 3rd pulsing with initial specimen for the SUS316L. The different colors in the IPF ND, RD, and TD maps indicate the orientation of each grain with respect to ND, RD, and TD, respectively.

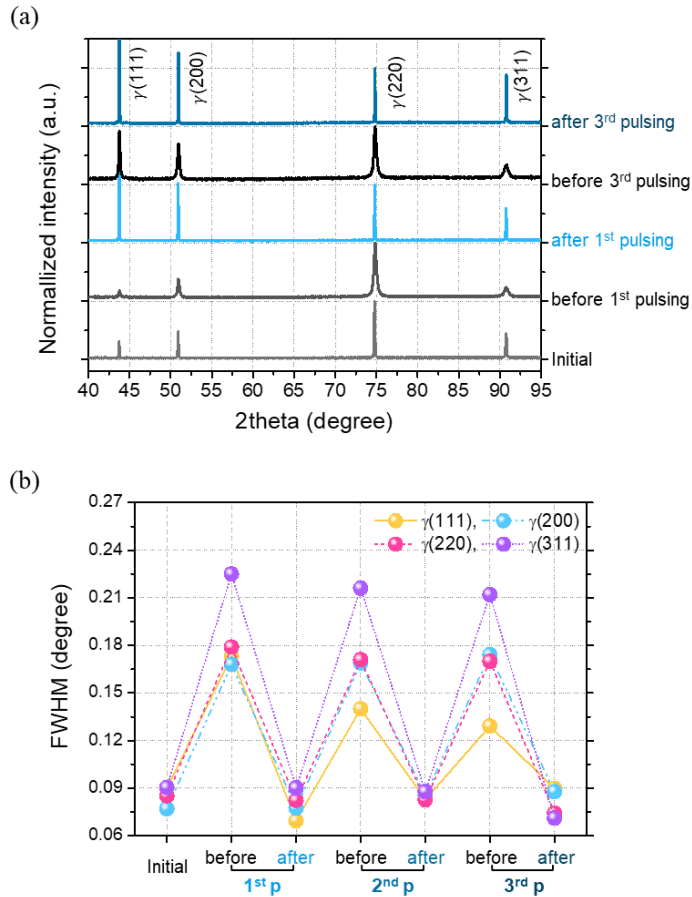


Figure 4.15 (a) X-ray diffraction (XRD) patterns before and after 1st and 3rd pulsing. For the comparison, the XRD pattern for the initial specimen is shown. (b) Full width at half maximum (FWHM) profiles of austenite phase peaks before and after each pulsing in addition to the initial specimen. The (111), (200), (220), and (311) peaks of austenite phase are used to obtain the FWHM values based on the XRD pattern.

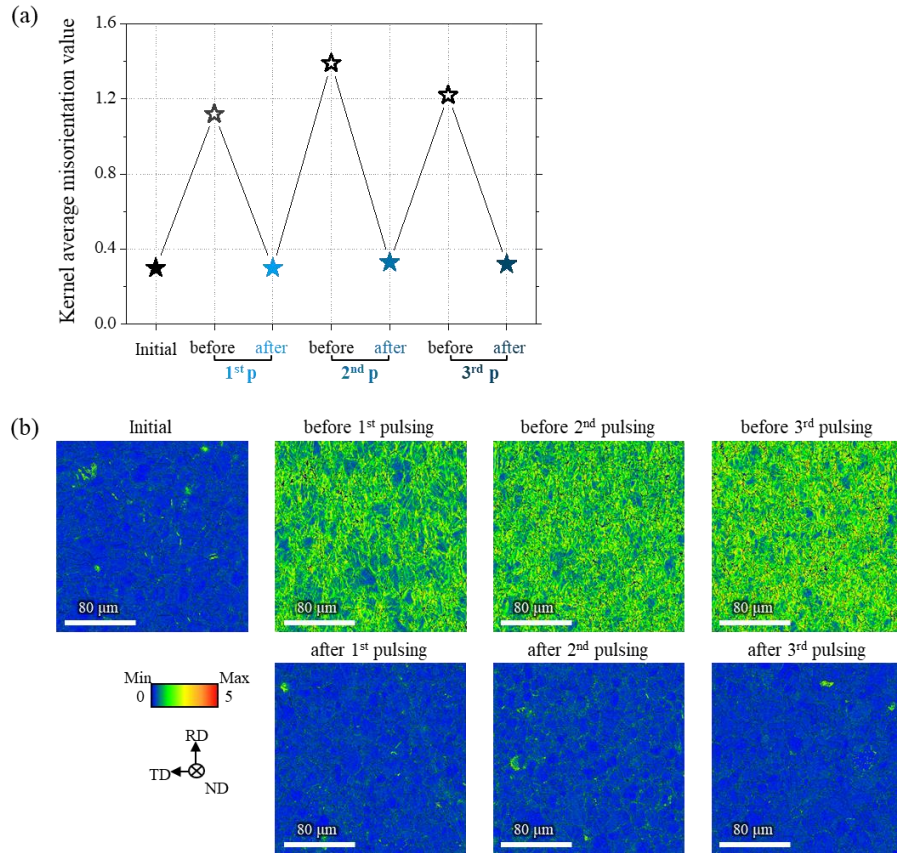


Figure 4.16 (a) The average kernel average misorientation (KAM) values before (unfilled symbol) and after (filled symbol) each pulsing in addition to the initial specimen (black filled symbol). (b) EBSD KAM maps at each condition. The range of degree of misorientation is 0 to 5, and is indicated in red to blue. Note that the brighter the colored areas, the more deformed the part with a higher dislocation density.

4.5 Case 3: super-elastic NiTi alloy

NiTi alloy (Nitinol) has the unique property of super-elasticity (SE) due to the diffusionless and reversible stress-assisted martensitic transformation of a metastable austenite phase. Under an external stress, the metastable austenite phase (B2 phase, b.c.c. structure) transforms to the martensite phase (B19' phase, monoclinic structure) [32, 33]. Once the stress is removed, it returns to its original shape as the martensite phase fully transforms back to the austenite phase. This is called the SE effect. Thus, this unique property and high biocompatibility make the super-elastic NiTi alloy a top choice material for biomedical applications or next-generation refrigeration systems. However, there is still problem in application of the NiTi alloy due to structural and functional stability upon cyclic deformation which is essentially required for biomedical application. It is well known that the structural and functional fatigue effect in the NiTi alloy occurs during cyclic deformation, resulting in the degradation of the SE characteristics and mechanical failure. For this reason, many researchers claimed to be the permanent strain accumulated during the cyclic deformation due to the formation of dislocation and other lattice defects generated at high stress levels in the preceding tension cycle [34, 35].

In addition, it was reported that the amount of stabilized martensite phase which did not return to the austenite phase increased as the number of cycles increased due to the internal stress formed by dislocation [36]. To overcome these problems, various efforts to suppress dislocation slip during stress-assisted martensitic

transformation by raising the critical stress for dislocation slip have been conducted [37, 38]. However, the fatigue due to the cyclic deformation cannot be fundamentally removed by this method only. Thus, we apply the concept of microstructure resetting for infinite reuse to the super-elastic NiTi alloy. The reverse transformation of the stabilized martensite and the dislocation recovery are utilized as the resetting cores of the super-elastic NiTi alloy.

For making the damaged microstructure in the super-elastic NiTi alloy, a cyclic deformation, including loading and unloading, is performed. Here, we decide to fix 100 cycles to which we apply electric pulsing. Although we could repeat this process many more times, here only 3 times of cyclic deformation (total 300 cycles) and pulsing treatments are applied. The measured temperature during pulsing treatment was represented in Fig. 4.17b. Fig. 4.18 exhibits the stress-strain curves obtained during repeated deformation of 100 cycles for the specimens before and after each pulsing treatment. Comparing with the 100th cycle of initial specimen and 1st cycle after 1st pulsing treatment, it is observed that the stress-strain curve changed by the cyclic deformation is returned to the initial state by applying electric pulsing.

To quantitatively evaluate SE characteristics, the residual and recovered strain values are plotted as a function of number of cycles (Fig. 4.19). These values are obtained from each stress-strain curve based on the method in Fig. 4.17a. ϵ_{rec} is the recovered strain during unloading, and ϵ_{res} is the residual strain after unloading which means a permanent strain accumulated in the specimen. As the number of cycles proceeds, the residual and recovered strain increase and decrease, respectively,

while the hysteresis curve becomes smaller. However, all these values become insensitive to cycling with increasing number of cycles, i.e., there is a steady state of the SE characteristics corresponding to cyclic stress level. This implies that the SE characteristics are stabilized against the cyclic deformation, which can be explained by the formation of dislocation during cyclic deformation [36]. However, here the residual and recovered strain stabilized after 100 cycles can successfully be returned to the initial state by applying electric pulsing.

From the XRD analysis, it is observed that new peaks of martensite phase are identified and the intensity of martensite phase peaks existed in the initial specimen increases by the cyclic deformation (Fig. 4.20a). This means that the stabilized martensite phase is gradually generated by the cyclic deformation, which is also observed from the EBSD image quality (IQ) map for the specimen before 1st pulsing treatment (Fig. 4.20b). Line traces within the grain in IQ map indicates that the stabilized martensite phase has a thin-plate shape, as marked by arrows, which is also observed in a previous study [36]. Thus, the stabilized martensite phase is considered to be the cause for the residual strain formed by the cyclic deformation. However, after the 1st pulsing treatment, the stabilized martensite phase disappears and returns back to the austenite phase, which is confirmed from both EBSD and XRD data (Fig. 4.20). Thus, we confirm that the stabilized martensite phase, which is formed by stress-assisted martensitic transformation, completely transforms into the austenite phase through reverse transformation by applying electric pulsing for 0.30 s.

We also focus on dislocation recovery after each pulsing. The change in the FWHM values of austenite phase peaks obtained from the XRD data is compared before and after each pulsing (Fig. 4.21a). Before each pulsing, FWHM values are much higher than those in the initial specimen due to the dislocation evolution by cyclic deformation. However, after each pulsing, FWHM values decrease to those in the initial specimen. This result is well matched with the KAM results obtained from the EBSD data (Figs. 4.21b and c). This result clearly indicates that the dislocation formed by cyclic deformation is annihilated by applying electric pulsing. In addition, there is no significant difference in microstructure, such as the average grain size and texture, after each pulsing from the IPF maps for ND (Fig. 4.22). Thus, we confirm that the damaged microstructure formed by the cyclic deformation of the super-elastic NiTi alloy can be successfully reset to its initial state through the resetting cores of martensitic reverse transformation and dislocation recovery by applying sub-second electric pulsing.

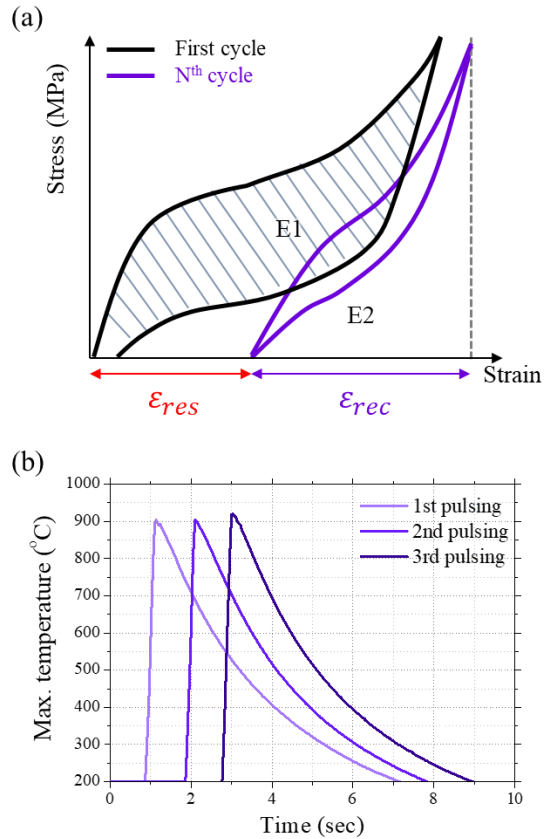


Figure 4.17 (a) Schematic stress-strain curves representing the super-elasticity (SE) characteristics for 1st and Nth cycle during the mechanical training. (b) Maximum temperatures of specimen measured during pulsing treatment for the super-elastic NiTi alloy. The time between the previous pulsing and the next pulsing is independent of the actual time of the experiment. To aid in understanding, the temperature histories of each pulsing are arranged in order at a certain interval.

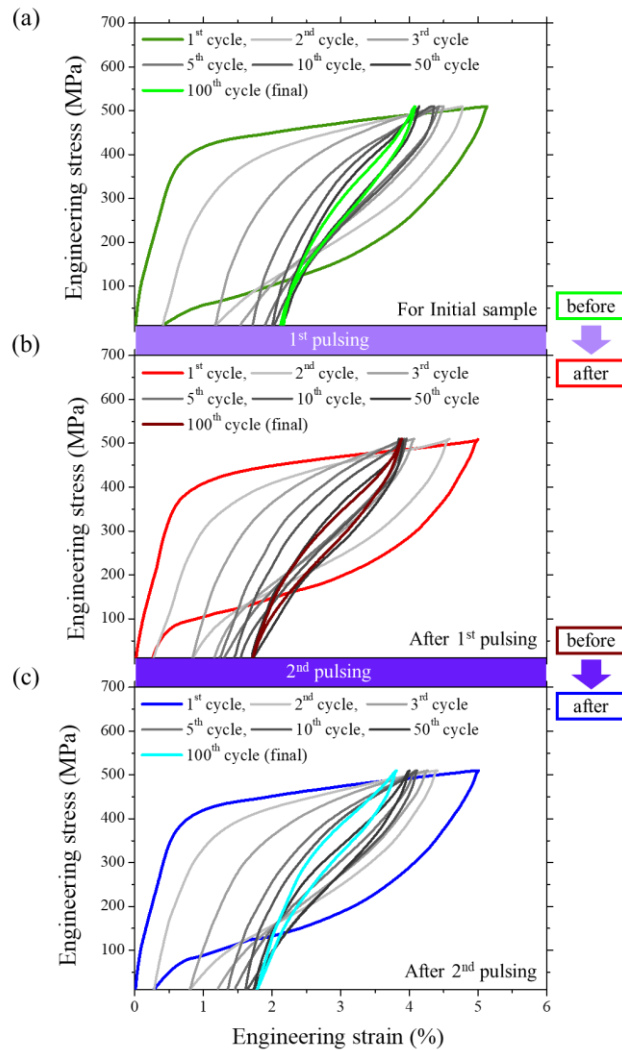


Figure 4.18 Stress-strain curves for 1st, 2nd, 3rd, 5th, 10th, 50th, and 100th cycle during the mechanical training of 100 cycles at RT for the (a) initial specimen, (b) specimen after 1st pulsing treatment, and (c) specimen after 2nd pulsing treatment, respectively. The stress-strain curve of first and final cycle is represented in colored solid line.

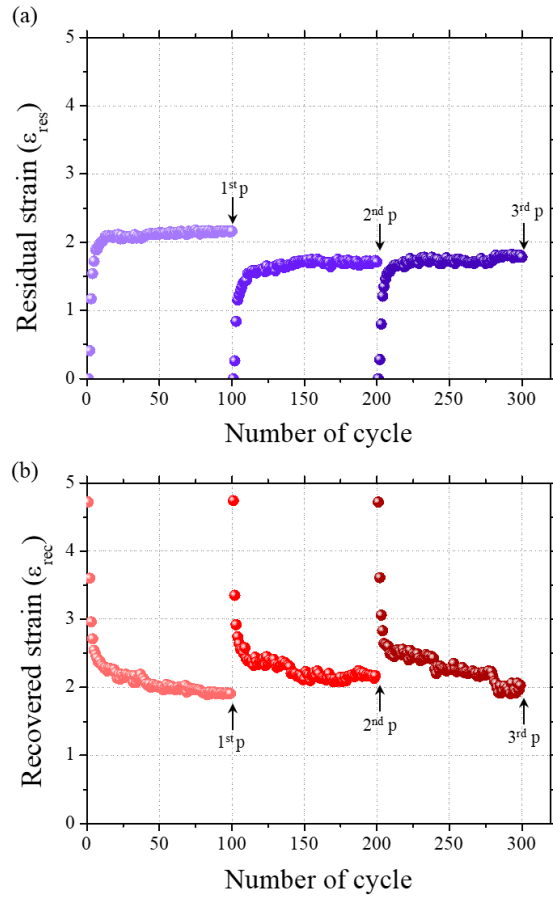


Figure 4.19 Effect of the mechanical training of 100 cycles on (a) residual strain and (b) recovered strain after each pulsing treatment. These data were obtained from the Fig. 4.18.

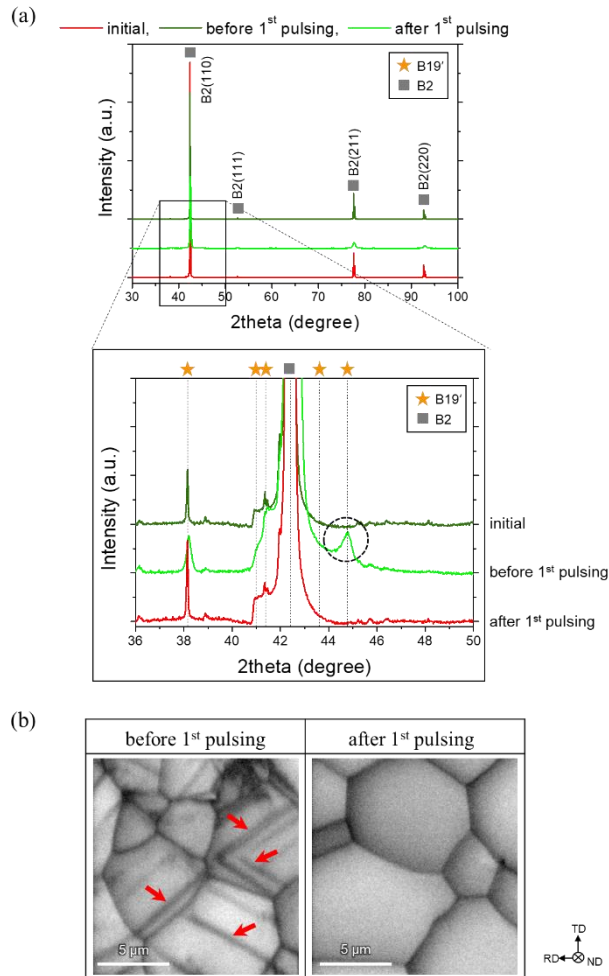


Figure 4.20 (a) XRD patterns for the specimens before and after 1st pulsing. For the comparison, the XRD pattern for the initial specimen is also shown. To clearly show the formation of stabilized martensite phase (B19'), the part where the peaks of the martensite phase appears is enlarged. (b) EBSD image quality (IQ) maps for the specimens before and after 1st pulsing. The stabilized martensite phase is marked by red arrows.

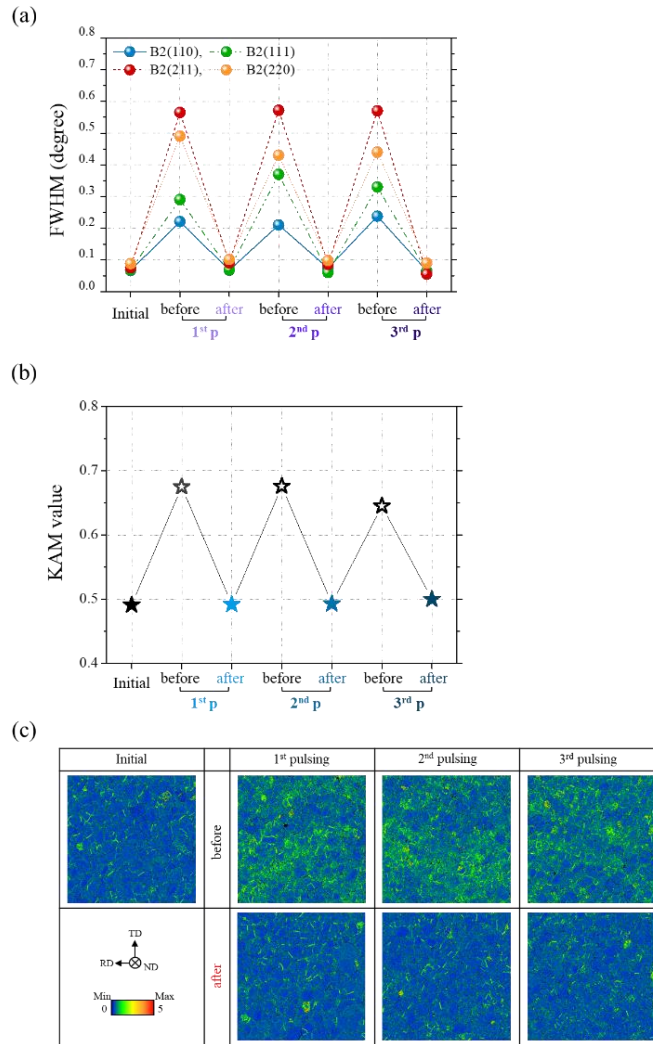


Figure 4.21 (a) FWHM profiles of B2 austenite phase peaks before and after each pulsing in addition to the initial specimen. The (110), (111), (211), and (220) peaks of B2 austenite phase are used to obtain the FWHM values based on the XRD pattern. (b) The KAM values before (unfilled symbol) and after (filled symbol) each pulsing. (c) EBSD KAM maps at each condition.

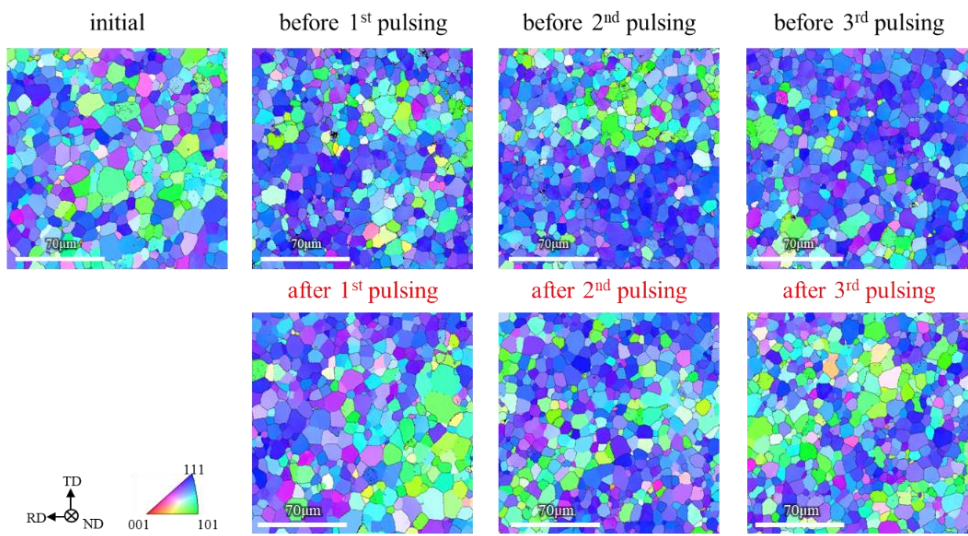


Figure 4.22 EBSD inverse pole figure (IPF) maps for normal direction (ND) before and after 1st, 2nd, and 3rd pulsing treatment with initial specimen. The different colors in the IPF map indicate the orientation of each grain with respect to ND.

4.6 Conclusion

In this chapter, a novel concept to reset a damaged microstructure by applying a repeated sub-second electric pulsing was proposed. This concept can sufficiently be alternative technique for healing the damaged materials and make the infinite reuse of bulk metallic materials possible, which is successfully realized using SUS301L, SUS316L, and super-elastic NiTi alloy. For the SUS301L, two resetting cores of reverse transformation of mechanically induced martensite phase and recrystallization of the deformed austenite phase are key roles in the microstructure resetting (Fig. 4.23a). For the SUS316L, the resetting core of recrystallization of deformed austenite phase is operated as the mechanism of the microstructure resetting. Also, the grain size after each pulsing treatment is identical with the initial state through the additional grain growth during pulsing treatment (Fig. 4.23b). For the super-elastic NiTi alloy, the damaged microstructure by cyclic deformation is successfully reset through the two resetting cores of reverse transformation of stabilized martensite phase and dislocation recovery (Fig. 4.23c).

In particular, for the SUS301L, comparing the actual cross-sectional area of the fractured specimen with initial specimen, we confirm that the specimen was deformed by a true strain of $\sim 3100\%$ after 11 pulsing treatments. This result is as if superplastic-like deformation occurs at RT. Furthermore, the complete martensitic reverse transformation, dislocation recovery, and recrystallization require normally a much longer duration (from 30 min to 2 h). However, the martensitic reverse transformation, dislocation recovery, and recrystallization are fully completed in

only 0.30–0.65 s in this study. This means that it can remarkably save time and costs in the materials process.

Thus, it can be said that the microstructure resetting method proposed in this study is combined with the extreme simplicity, rapidness, and infinite repetition which cannot be achieved by the conventional methods such as heat treatment. Also, this can open new avenues for non-autonomous self-healing of damaged microstructure of metallic materials and will guide in designing for the infinite reuse of commercial metallic materials.

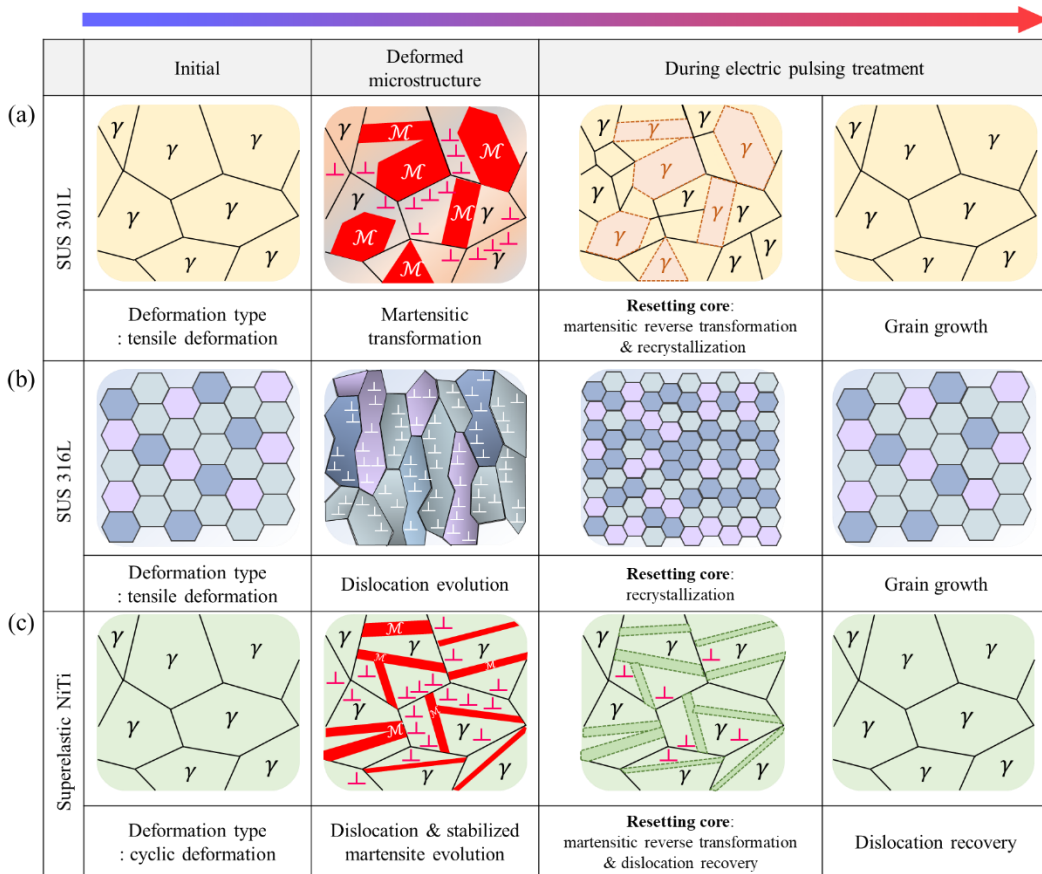


Figure 4.23 Summary for the principle of microstructure resetting in the selected three materials based on the resetting core classified into three categories (phase transformation, dislocation recovery, and recrystallization) for the (a) SUS301L, (b) SUS316L, and (c) super-elastic NiTi alloy.

4.7 References

- [1] B. Ghosh, M. W. Urban, *Science*, 323 (2009) 1458.
- [2] M. Burnworth, L. Tang, J. R. Kumpfer, A. J. Duncan, F. L. Beyer, G. L. Fiore, S. J. Rowan, C. Weder, *Nature*, 472 (2011) 334.
- [3] B. Grabowski, C. C. Tasan, *Self-Healing Metals*, Springer, Cham, Switzerland (2016) 387.
- [4] Y. Yanagisawa, Y. Nan, K. Okuro, T. Aida, *Science*, 359 (2018) 72.
- [5] H. Song, Z.-J. Wang, X.-D. He, J. Duan, *Sci. Rep.*, 7 (2017) 1.
- [6] J. Kim, H. J. Kim, S. H. Hong, H. J. Park, Y. S. Kim, Y. J. Hwang, Y. B. Jeong, J.-Y. Park, J. M. Park, B. Sarac, W.-M. Wang, J. Eckert, K. B. Kim, *Sci. Rep.*, 8 (2018) 1.
- [7] J. B. Ferguson, B. F. Schultz, P. K. Rohatgi, *JOM*, 66 (2014) 866.
- [8] K. S. Toohy, N. R. Sottos, J. A. Lewis, J. S. Moore, S. R. White, *Nat. mater.*, 6 (2007) 581.
- [9] M. Li, K. G. Pradeep, Y. Deng, D. Raabe, C. C. Tasan, *Nature*, 534 (2016) 227.
- [10] M. Koyoma, Z. Zhang, M. Wang, D. Ponge, D. Raabe, K. Tsuzaki, H. Noguchi, C. C. Tasan, *Science*, 355 (2017) 1055.
- [11] M.-J. Kim, K. Lee, K. H. Oh, I.-S. Choi, H.-H. Yu, S.-T. Hong, H. N. Han, *Scr. Mater.*, 75 (2014) 58.
- [12] C. D. Ross, D. B. Irvin, J. T. Roth, *J. Eng. Mater. Tech.*, 129 (2007) 342.
- [13] J. Magargee, F. Morestin, J. Cao, *J. Eng. Mater. Tech.*, 135 (2013) 041003–1.
- [14] M.-J. Kim, M.-G. Lee, K. Hariharan, S.-T. Hong, I.-S. Choi, D. Kim, K. H.

- Oh, H. N. Han, *Int. J. Plast.*, 94 (2017) 148.
- [15] A. Rahnama, R. Qin, *Sci. Rep.*, 7 (2017) 42732.
- [16] H.-J. Jeong, M.-J. Kim, J.-W. Park, C. D. Yim, J. J. Kim, O. D. Kwon, P. P. Madakashira, H. N. Han, *Mater. Sci. Eng. A*, 684 (2017) 668.
- [17] J.-W. Park, H.-J. Jeong, S.-W. Jin, M.-J. Kim, K. Lee, J. J. Kim, S.-T. Hong, H. N. Han, *Mater. Charact.*, 133 (2017) 70.
- [18] W. A. Salandro, J. J. Jones, C. Bunget, L. Mears, J. T. Roth, *Introduction to Electrically Assisted Forming*, in *Electrically Assisted Forming*, Springer, Cham, Switzerland (2015) 23.
- [19] K. Bhattacharya, S. Conti, G. Zanzotto, J. Zimmer, *Nature*, 428 (2004) 55.
- [20] X. G. Zheng, Y.-N. Shi, K. Lu, *Mater. Sci. Eng. A*, 561 (2013) 52.
- [21] A. Martinez-de-Guerenu, F. Arizti, M. Diaz-Fuentes, I. Gutierrez, *Acta Mater.*, 52 (2004) 3657.
- [22] G. B. Olson, M. Cohen, *Metall. Trans. A*, 13 (1982) 1907.
- [23] H. N. Han, C. G. Lee, C.-S. Oh, T.-H. Lee, S.-J. Kim, *Acta Mater.*, 52 (2004) 5203.
- [24] H. N. Han, D.-W. Suh, *Acta Mater.*, 51 (2003) 4907.
- [25] S.-J. Lee, Y.-M. Park, Y.-K. Lee, *Mater. Sci. Eng. A*, 515 (2009) 32.
- [26] G.-S. Sun, J. Hu, B. Zhang, L.-X. Du, *Mater. Sci. Eng. A*, 732 (2018) 350.
- [27] A. F. Padilha, R. L. Plaut, P. R. Rios, *ISIJ Int.*, 43 (2003) 135.
- [28] C. Herrera, R. L. Plaut, A. F. Padilha, *Mater. Sci. Forum*, 550 (2007) 423.
- [29] T. Masumura, N. Nakada, T. Tsuchiyama, S. Takaki, T. Koyano, K. Adachi,

- Acta Mater., 84 (2015) 330.
- [30] G. K. Williamson, W. H. Hall, *Acta Metall.*, 1 (1953) 22.
- [31] T. Ungar, A. Borbely, *Appl. Phys. Letts.*, 69 (1996) 3173.
- [32] Y. Kudoh, M. Tokonami, S. Miyazaki, K. Otsuka, *Acta Metall.*, 33 (1985) 2049.
- [33] K. Otsuka, X. Ren, *Prog. Mater. Sci.*, 50 (2005) 511.
- [34] G. Eggeler, E. Hornbogen, A. Yawny, A. Heckmann, M. Wagner, *Mater. Sci. Eng. A*, 378 (2004) 24.
- [35] M. J. Mahtabi, N. Shamesaei, M. R. Mitchell, *J. Mech. Behav. Biomed. Mater.*, 50 (2015) 228.
- [36] S. Miyazaki, T. Imai, Y. Igo, K. Otsuka, *Metall. Trans. A*, 17 (1986) 115.
- [37] F. Sun, S. Nowak, T. Gloriant, P. Laheurte, A. Eberhardt, F. Prima, *Scr. Mater.*, 63 (2010) 1053.
- [38] Z. Zhang, R. D. James, S. Muller, *Acta Mater.*, 57 (2009) 4332.
- [39] S. X. McFadden, R. S. Mishra, R. Z. Valiev, A. P. Zhilyaev, A. K. Mukherjee, *Nature*, 398 (1999) 684.
- [40] B.-N. Kim, K. Hiraga, K. Morita, Y. Sakka, *Nature*, 413 (2001) 288.

Chapter 5

Total conclusion

In this study, the effect of electric current on dissolution of $Mg_{17}Al_{12}$ phase, mechanically induced martensitic transformation (MIMT), and dislocation recovery using AZ91 magnesium alloy and TRIP-aided steel were investigated based on microstructural analysis. In addition, the microstructure reset-based self-healing method using sub-second electric pulsing was proposed and demonstrated for infinite reuse when the microstructure of metallic materials is damaged by deformation.

First, AZ91 magnesium alloys normally contain significant amounts of brittle $Mg_{17}Al_{12}$ phase which induces poor ductility. Thus, an electric pulsing was introduced during deformation in order to improve the ductility while omitting additional dissolution heat treatment in Chapter 2. The effect of electric current on dissolution of $Mg_{17}Al_{12}$ phase in as-extruded AZ91 magnesium alloy was investigated by uniaxial tensile testing and microstructural analysis. When a periodic electric pulsing was applied to the specimen during plastic deformation, the flow stress substantially decreased and the elongation at fracture increased 3.7 times compared to the non-pulsed tensile test at RT. From EBSD and EDS phase mapping analysis, it was observed that the average fraction of $Mg_{17}Al_{12}$ phase dissolved during pulsed tensile test was much larger than that during IHT. These results

sufficiently support that dissolution of the $Mg_{17}Al_{12}$ phase occurs by both thermal effect due to Joule heating and athermal effect of electric current during pulsed tensile test. In addition, the athermal effect of electric current on dissolution of the $Mg_{17}Al_{12}$ phase was demonstrated by comparing $Mg_{17}Al_{12}$ phase fractions after EPT and CHT. Thus, it could be understood that electric current can accelerate the dissolution of the $Mg_{17}Al_{12}$ phase, resulting in significant improvement of ductility.

In Chapter 3, the effect of electric current on the MIMT for TRIP-aided steel was investigated based on microstructural analysis and calculation of the MIMT kinetics. When a periodic electric pulsing was applied to the specimen until fracture (multi-pulsed tension), the elongation at fracture decreased compared to the non-pulsed tension at RT, although the flow stress was reduced significantly. From the XRD analysis, it was identified that the MIMT effect could not work properly in the multi-pulsed tension because the stability of the retained austenite phase increased due to a temperature rise by applying electric current. Thus, a pattern of electric pulsing was newly designed to improve the formability of TRIP-aided steel. 3 pulses of electric current were applied in the early stage of deformation before the phase transformation of retained austenite phase begins to take place. As a result, a significant increase in elongation was observed compared to non-pulsed tension at RT. It was identified that the increase in elongation in the 3-pulsed tension was due to two effects. One is the delay effect of MIMT, which is caused by the increased in stability of retained austenite phase during electric current application. Thus, the MIMT effect was exhibited in earnest in the latter stage of deformation. The other is

the dislocation recovery effect caused by applying electric current, which is identified by comparing the FWHM values obtained from the XRD measurement. Also, it was confirmed that dislocation recovery was accelerated by applying electric current.

In Chapter 4, the microstructure resetting method was proposed based on the electroplasticity and concept of non-autonomous self-healing. The damaged microstructure of metallic materials was instantly reset into the initial state by applying a sub-second electric pulsing. Key points in this microstructure resetting method are finding the critical point where the electric pulsing is applied to the specimen and choosing the materials to which the resetting core reflecting a reversible damage characteristics is applicable. Herein, the resetting core was classified into three categories: phase transformation, dislocation recovery, and recrystallization. Microstructure resetting-assist infinite reuse was successfully realized using SUS301L, SUS316L, and super-elastic NiTi alloy. For the SUS301L, two resetting cores of reverse transformation of mechanically induced martensite phase and recrystallization of the deformed austenite phase are key roles in the microstructure resetting. For the SUS316L, the resetting core of recrystallization of deformed austenite phase is operated as the mechanism of the microstructure resetting. Also, the grain size after each pulsing treatment is identical with the initial state through the additional grain growth during pulsing treatment. For the super-elastic NiTi alloy, the damaged microstructure by cyclic deformation is successfully reset through the two resetting cores of reverse transformation of stabilized

martensite phase and dislocation recovery.

From this study, it was confirmed that the deformation capacity of AZ91 magnesium alloy was enlarged due to the electric current-induced dissolution of the brittle $Mg_{17}Al_{12}$ phase during deformation. Also, electric current-induced delay of MIMT and annealing also occurred during plastic deformation for the TRIP-aided steel so that the ductility was improved. Thus, if EAM is carefully applied to the material considering the microstructural features, it was proved that the formability can be sufficiently improved without degradation of mechanical property. Furthermore, by proposing the microstructure resetting method in this study, it was clearly identified that the damaged materials can be infinitely reused. This novel method has an unlimited potential as it can be applied to various industrial applications.

국문 초록

금속 재료의 변형 중에 고밀도 전류가 인가되면, 유동 응력이 감속함과 동시에 연성이 현저히 증가하게 되는데, 이러한 현상을 통전 소성 (Electroplasticity) 이라고 하며, 최근 학계와 제조 분야에서 통전 소성에 대한 연구가 많은 주목을 받고 있다. 1969년 Troistkii에 의해 처음으로 통전 소성이 보고됨에 따라, Conrad, Ross, Roth, Cao, 등의 연구자들을 중심으로 다양한 금속 재료에 대한 통전 소성 현상들이 집중적으로 관찰되었다. 그 후, 많은 연구자들이 통전 소성에 대한 메커니즘을 규명하고자 시도하였으며, 대표적으로 저항 발열에 의한 Joule heating에 의한 것으로 보는 관점과 고전류 밀도의 전류 인가에 의한 electron wind force가 원자의 이동을 촉진시킨다는 관점으로 보는 것이 제안되었다. 아직까지 정확한 메커니즘은 규명되지 않은 상황이지만, 그들은 전류가 Joule heating에 의한 열적 효과(thermal effect)와는 별개로 비열적 효과(athermal effect)에 의해 어닐링, 노화, 용체화 및 재결정과 같은 미세조직 변화를 가속화시킨다는 것을 공통적으로 주장하였다. 최근에는, 통전 소성 효과의 장점들을 활용하여, 실공정에 적용하기 위한 다양한 노력들이 활발하게 진행되고 있으며, 이러한 통전 소성을 활용하는 제조 기술을 통전 성형법(Electrically

assisted manufacturing, EAM)이라고 일컫는다. 더불어, 이는 성형 공정 외에 굽힘, 압출, 압연 등의 공정에 광범위하게 활용이 가능하다는 점에서 가능성이 무궁무진한 기술이라 할 수 있다.

따라서, 본 연구에서는 AZ91 마그네슘 합금과 TRIP 강에서의 통전 소성 거동을 미세조직 분석과 함께 평가하고, 다양한 실험적 방법으로 전류의 효과를 확인하였다. 또한, 통전 소성 거동의 이해를 기반으로, 금속 재료의 무한 재사용을 위해 1초 미만의 전기적 펄싱을 활용하여 손상된 미세조직을 리셋할 수 있는 방법을 제안하고 검증하였다.

먼저, 압출된 AZ91 마그네슘 합금에 대해 통전 인장을 진행하면서 기계적 거동과 미세조직 변화를 분석함으로써, $Mg_{17}Al_{12}$ 상의 용체화에 미치는 전류의 영향이 평가되었다. 통전 인장 시 유동 응력은 감소하고, 상온에서 일반 인장 시 측정된 파단 연신율에 비해 약 3.7배 증가하였다. 전류의 비열적 효과를 구분하기 위해, 통전 인장 시 측정된 온도 이력과 동일한 이력으로 딜라토미터를 활용하여 유도 열처리를 수행하였다. 각 조건에서의 EBSD 및 EDS 분석으로부터, 통전 인장 시 $Mg_{17}Al_{12}$ 상의 용체화가 가속화되어 일어나는 것이 관찰되었고, 추가적으로 동일 온도와 시간에 대해 통전 처리와 노 열처리 후 시편에서의 $Mg_{17}Al_{12}$ 상의 분율을 비교해본 결과, 통전 처리 후 시편에서 더 많은 $Mg_{17}Al_{12}$ 상의 용체화가 일어나는 것을 확인하였다. 이를 통해, 변형 시 전류가

인가되면 전류 자체의 비열적 효과로 인해 $Mg_{17}Al_{12}$ 상의 용체화 (Electric current-induced dissolution) 현상이 가속화되어 최종적으로 연성이 크게 개선될 수 있음이 증명되었다.

다음으로, TRIP 강에 대해 통전에 의한 기계적 거동과 미세조직 변화를 분석함으로써 변형유기 마르텐사이트 상변태 (Mechanically induced martensite transformation, MIMT) 및 전위 회복에 미치는 전류의 영향이 평가되었다. 인장 변형 시 파단 할 때까지 주기적으로 펄스 전류를 인가한 결과, 유동 응력은 감소함에도 불구하고, 상온에서의 일반 인장과 비교하여 파단 연신율이 현저히 감소하였다. XRD 분석 및 MIMT kinetics의 계산 결과로부터, 통전 인장 시 온도 상승으로 인한 오스테나이트 상의 안정성 증가로 MIMT가 제대로 발휘되지 않아 파단연신율이 감소하는 것이 관찰되었다. 따라서, 이를 극복하기 위해, 전류 인가 패턴을 새롭게 설계하였으며, MIMT가 발생하는 변형 초기 단계에 3번의 펄스 전류를 인가하였다. 그 결과, 일반 인장 대비 파단 연신율이 증가하는 것이 관찰되었으며, 이는 2가지 영향에 기인하는 것을 확인하였다. 하나는 전류를 인가하는 동안 오스테나이트 상의 안정성이 증가함에 따라 MIMT의 발생이 지연되는 효과 (Electric current-induced delay of MIMT)이다. 다른 하나는 전류가 인가되는 동안 시편 내부에 발생하는 전위 회복 효과(Electric

current-induced dislocation recovery)로, 이는 XRD 분석으로부터 얻어진 피크의 반가폭 값을 비교함으로써 입증되었다.

마지막으로, 앞서 규명된 통전 소성 효과를 바탕으로 금속 재료의 미세조직 리셋팅 방법이 제안되었다. 일반적으로, 금속 재료의 미세 스케일 결함은 초기 미세조직을 손상시켜 기계적 특성 및 기대 수명을 저하시킨다. 따라서, 재료의 손상을 치유 또는 복구하기 위해 자가 치유(Self-healing) 개념에 기초하여 다양한 방법들이 제안되었다. 본 연구에서는 1초 미만의 전기적 펄싱을 비자율적(Non-autonomous) 자가 치유 방법 중 하나로, 금속 재료의 손상된 미세조직을 리셋하는 데에 활용하였다. 이 방법의 핵심은 전기적 펄싱을 시편에 인가하기 위한 지점을 찾는 것과, 리셋팅 코어(resetting core)를 적용하기에 적합한 재료를 선택하는 것이다. 여기서 리셋팅 코어는 가역적인 손상 특성을 반영하여 정의하였으며, 본 연구에서는 상 변태, 전위 회복 및 재결정의 세 가지 범주로 분류하여 제안하였다. 따라서, SUS301L(마르텐사이트 역변태 및 재결정을 통한 리셋팅), SUS316L(재결정을 통한 리셋팅) 및 초탄성 NiTi 합금(마르텐사이트 역변태 및 전위 회복을 통한 리셋팅)을 활용하여 미세조직 리셋 기반 재료의 무한 재사용이 가능함을 명확하게 보여주었다.

따라서, 본 연구를 통해 전류가 용체화, 마르텐사이트 상변태 및 전위

회복, 등에 미치는 영향이 명확하게 조사되었으며, 각 재료의 미세조직적 특성을 고려하여 적절하게 통전을 적용함으로써 재료의 물성과 공정 효율을 동시에 향상시킬 수 있는 최적의 조건들을 확보할 수 있었다. 더 나아가, 통전 소성 거동 이해를 기반으로 미세조직 리셋 기반 자가치유 방법을 제안하였으며, 1초 미만의 전기적 펄싱을 인가하는 것 만으로 손상된 미세조직을 초기 상태로 리셋할 수 있음을 입증하였다. 이는 열처리와 같은 기존의 방법으로는 달성할 수 없는 극도의 용이함, 신속성 및 무한 반복성, 등이 결합된 새로운 방법이며, 더욱이 본 연구를 통해 다양한 산업 및 학계에서 통전 소성을 활용함에 있어 충분한 통찰력을 제공할 것으로 기대하는 바이다.

핵심어: 구조재료, 마그네슘 합금, TRIP 강, 초탄성 NiTi 합금, 통전 소성, 통전 성형법, SEM, EBSD, XRD, 용체화, 마르텐사이트 상변태, 전위 회복, 재결정, 성형성, 손상, 미세구조 리셋팅, 비자율적 자가 치유

Student number: 2014-22532